Vol.16, No.4(51), Summer 2023

Progress in Color, Colorants and Coatings

Ministry of Science, Research and Technology
Institute for Color
Science &Technology

Vol. 16, No. 4(51), Autumn 2023

Print ISSN: 2008-2134
Online ISSN: 2283-1790

P
C
C
C

Progress in Color, Colorants and Coatings

Available online at
www.pccc.icrc.ac.ir

Ministry of Science, Research and Technology

Iran Color Society

Ministry of Science, Research and Technology
Institute for Color
Science & Technology

CECST
Center of Excellence for
Color Science and Technology

Progress in Color, Colorants and Coatings

The Progress in Color, Colorants and Coatings Journal is an international research peer reviewed Journal covers a wide range of the highly interdisciplinary field of color science and technogy, including (i) Color Imaging and Image Processing, (ii) Color Physics (Color Control and Measurement, Color Imaging and Color Image Processing), (iii) Environmental Aspect on Color and Coating Science and Technology, (iv) Ink and Printing Science and Technology, (v) Inorganic Pigments and Glazes including their applications, (vi) Novel Technologies in Color and Coating Science and Technology (Nano Technology, Bio Technology), (vii) Organic Colorants and Their applications, (viii) Resin and Additives, (ix) Surface Coatings & Corrosion (Materials / Applications), (x) Inorganic Coatings their applications, (xi) Outlook, Market and Technology Trend, (xii) Standardization.

Publisher: Institute for Color Science and Technology

Printing Office: Iran Kohan Print

Manager-in-Chief : Zahra Ranjbar
Professor, Insititute for Color Science and Technology, Tehran, Iran.
ranjbar@icrc.ac.ir

Editor-in-Chief: Zahra Ranjbar
Professor, Institue for Color Science and Technology,
Tehran, Iran. ranjbar@icrc.ac.ir

Assistant Editor: Mozhgan Hosseinnezhad
Assistant Professor, Institue for Color Science and Technology,
Tehran, Iran. hosseinnezhad-mo@icrc.ac.ir

Editorial Board

Faramarz Afshar Taromi
Professor, Amirkabir University of Technology, Tehran, Iran
afshar@aut.ac.ir
Hosein Amirshahi
Professor, Amirkabir University of Technology, Tehran, Iran
hamirshah@aut.ac.ir
Hosein Sarpoolaky
Associate Professor, Iran University of Science andTechnology,
Tehran, Iran. hsarpoolaky@iust.ac.ir
Issa Yavari
Professor, Tarbiat Modares University, Tehran, Iran
yavarisa@modares.ac.ir
Kamaladin Gharanjig
Professor, Institute for Color Science and Technology, Tehran, Iran
gharanjig@icrc.ac.ir
Mohsen Mohseni
Professor, Amirkabir University of Technology, Tehran, Iran
mmohseni@aut.ac.ir
Niyaz Mohammad Mahmoodi
Professor, Institute for Color Science and Technology,
Tehran, Iran. mahmoodi@icrc.ac.ir
Ramazan Solmaz
Associate Professor, Bingol University, Turkey
rsolmaz@bingol.edu.tr
Siamak Moradian
Professor, Amirkabir University of Technology, Tehran, Iran
moradian@aut.ac.ir
Stephen Westland
Professor, Univrsity of Leeds, UK
s.westland@leeds.ac.uk
Wan Saime Wan Ngah
Professor, University Sains Malaysia, Malaysia
wsaime@usm.my
Zahra Ranjbar
Professor, Institute for Color Science and Technology, Tehran, Iran,
ranjbar@icrc.ac.ir

Adminstration Office:

Mehrnoosh Ghasemi
Institute for Color Science and Tecnology

Publishing Office:
No.55, Vafamanesh St. Lavizan Exit, Sayad Shirazi North HWY, P. O. Box:16765-654, Tehran-Iran; Tel/Fax:+98 21 22947358

Notice:
No responsibility is assumed by the publisher for any injury and/or damage to persons or property as a matter of products liability, negligence or from any use or opreration of any methode and products in the material herein.

Please follow the Instructure for Authors at www.pccc.icrc.ac.ir

2023

Progress in Color, Colorants and Coatings

Vol. 16, No. 4, 2023

Editor in Chief:

Prof. ZAHRA RANJBAR

Assistant Editor:

Dr. MOZHGAN HOSSEINNEZHAD

In the Name of God

Progress in Color, Colorants and Coatings

Vol. 16, No. 4, 2023

CONTENTS

PROGRESS IN COLOR, COLORANTS AND COATINGS

available online @ www.pccc.icrc.ac.ir

Progress in Color Colorants Coating 16 (2023), 319-329

Ministry of Science, Research and Technology
Institute for Color Science & Technology

Schiff's Base Performance in Preventing Corrosion on Mild Steel in Acidic Conditions

A. Naseef Jasim[1], B. A. Abdulhussein[2], S. Mohammed Noori Ahmed[3], W. K. Al-Azzawi[4], M. M. Hanoon[3], M. K. Abbass[3], A. A. Al-Amiery[5, 6*]

[1.] Materials Engineering Department, Diyala University, P.O. Box: 32001, Diyala-Iraq
[2.] Chemical Engineering Department, University of Technology, P.O. Box: 10001, Baghdad-Iraq
[3.] Production and Metallurgy Engineering Department, University of Technology, P.O. Box: 10001, Baghdad, Iraq
[4.] Al-Farahidi University, Baghdad, P. O. Box: 10001, Baghdad, Iraq.
[5.] Department of Chemical and Process Engineering, Faculty of Engineering and Built Environment, Univerversiti Kebangsaan Malaysia, P.O. Box: 43600 UKM Bangi, Selangor, Malaysia
[6.] Energy and Renewable Energies Technology Center, University of Technology, P.O. Box: 10001, Baghdad, Iraq

ARTICLE INFO

Article history:
Received: 04 Jan 2023
Final Revised: 24 Mar 2023
Accepted: 27 Mar 2023
Available online: 19 Aug 2023

Keywords:
Corrosion inhibitor
Schiff base
MMPC
Pyrazole
DFT

ABSTRACT

Many industries, particularly the oil and gas industry, extensively use metallic materials. However, steel is negatively impacted by corrosion, which decreases the functioning of its surfaces. Therefore, finding a solution to the corrosion challenge is imperative. To prevent mild steel from corroding in a 1 M hydrochloric acid medium, a Schiff base named methyl 5-(((((2-hydroxynaphthalen-1-yl)methylene)amino))-1-methyl-1H-pyrazole-4-carboxylate (MMPC) was utilized. Weight loss measurements and theoretical calculations were conducted to explore the effectiveness and mechanism of corrosion protection. MMPC adsorbs onto mild steel, blocking active sites, and the adsorption follows the Langmuir adsorption isotherm model. Based on a free energy (ΔG^{o}_{ads}) value of -37.25 KJmol^{-1}, physical adsorption and chemical adsorption are two separate adsorption modes. At a concentration of 0.5 mM and 303 K, the findings demonstrate that MMPC showed an excellent inhibitor effectiveness of 97.13 %. The acid reaction site is blocked by the inhibitor adsorbed onto the mild steel surface. Density Functional Theory (DFT) at the B3LYP/6-311 G^{++} basis set was also used to determine the effectiveness of the inhibitor, and the results demonstrated that MMPC is an effective inhibitor. Prog. Color Colorants Coat. 16 (2023), 319-329© Institute for Color Science and Technology.

1. Introduction

Due to its superior mechanical and thermal properties, mild steel is one of the most significant steel alloys used in various sectors to build factories, appliances, storage facilities, and more [1]. However, because of how quickly mild steel corrodes when exposed to acids, corrosion prevention is of great industrial and scientific interest [2]. Corrosive environments are utilized in various manufacturing processes, such as scaling, cleaning (oil well cleaning), and pickling [3]. Anticorrosion technology is a realistic, reliable, and economical corrosion reduction technology [4]. Effective corrosion inhibitors should greatly reduce the rate of metal corrosion during acidifying treatments. Corrosion inhibitors are adsorbed onto the metallic substrate to inhibit corrosion through their active

---

*Corresponding author: * dr.ahmed1975@ukm.edu.my
dr.ahmed1975@gmail.com

Doi: 10.30509/pccc.2023.167081.1197

functions. Several natural substances are used as corrosion inhibitors due to the well-documented risks associated with most synthetic corrosion inhibitors [5]. Corrosion inhibitor engineering is developing from the perspective of environmental sustainability. Green inhibitors, which are more ecologically responsible, are currently the subject of recent rules everywhere [6].

Hazardous compounds used as corrosion inhibitors, such as triazoles, heterocyclic rings, chromate ions, and molybdate ions, are believed to significantly slow corrosion rates. However, they contain carcinogenic compounds that kill plants and animals, heavy metals that wash into streams and ruin ecosystems, and are often very expensive to dispose of after being used in metal pipes. As a result, the usage of novel inhibitors with fewer side effects has increased due to concerns about toxicity, degradability, bioaccumulation, and affordability [7]. The much more significant and effective strategy for preventing iron corrosion is the application of organic inhibitors [8]. Widely utilized organic inhibitors include aromatic rings, double and triple bonds, nitrogen, sulfur, and oxygen as heteroatoms [9]. The effectiveness of such chemical compounds in preventing corrosion depends on their ability to remove adsorbed water molecules at the interface and create a tight protective film that shields the metal surface from the corrosive fluid [10]. The amount of adsorption is influenced by these organic molecules' molecular weight, projected surface area, and heteroatom content [11, 12].

Most of these substances have a poisonous character and stick poorly to metal surfaces. Therefore, in this study, a Schiff base (Figure 1) was assessed as a mild steel corrosion inhibitor in a 1 M HCl solution. The effects of concentration (0.1, 0.2, 0.3, 0.4, 0.5, and 1 mM), immersion duration (1, 5, 10, 24, and 48 h), and temperature (303, 313, 323, and 333 K) on the corrosion inhibition ability of the Schiff base were investigated using weight loss techniques. The evaluated Schiff base was subjected to computational investigations using density functional theory (DFT) to validate and support the experimental findings. The article presents a study on the use of a Schiff base named MMPC as a corrosion inhibitor for mild steel in a 1 M hydrochloric acid medium. The study combines experimental techniques such as weight loss measurements with theoretical calculations using Density Functional Theory (DFT) to explore the effectiveness and mechanism of corrosion protection. The objective of the article is to present the findings of the study on the effectiveness of MMPC as a mild steel corrosion inhibitor in a 1 M HCl solution. The investigation includes analyzing the effects of concentration, immersion duration, and temperature on the corrosion inhibition ability of the Schiff base, using weight loss techniques. The study also validates and supports the experimental findings with computational investigations using DFT.

2. Experimental

2.1. Materials and methods

The sample company provided the mild steel used in this research, and Table 1 specifies the element content by composition (by wt. %). The steel was cut into measurements of 35×20×4 mm and cleaned with silicon carbide paper. After treatment with acetone as a cleaning agent, the steel was rinsed with double distilled water and oven-dried before being weighed.

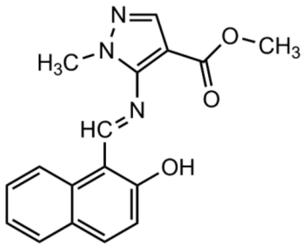

Figure 1: The structure of MMPC.

Table 1: Shows the weight percentage chemical composition of the metallic substrate.

Iron	Phosphorous	Sulphur	Aluminium	Silicon	Manganese	Carbon
Balance	0.09 %	0.05 %	0.01 %	0.38 %	0.05 %	0.21 %

2.2. Weight loss techniques

The metallic substrate was subjected to untreated and treated solutions of 1 M HCl. The treated solution had the tested inhibitor with concentrations of 0.1, 0.2, 0.3, 0.4, 0.5, and 1.0 mM. Exposure durations were 1, 5, 10, 24, and 48 hours at 303 K. To study the effect of temperature, the inhibited and uninhibited solutions were investigated for 5 hours at solution temperatures of 313, 323, or 333 K in accordance with NACE TM0169/G31 [13]. The tested coupons were then removed and treated in line with ASTM standard G1-03. Continuing the computations, the mean mass loss was used to calculate the rate of corrosion [14]. The rate of corrosion (C_R), the inhibitory performance (IE %), and the surface coverage (θ) were determined using Equations 1-3 [13,14]:

$$C_R\ (\mathrm{mg.cm^{-2}.h^{-1}})=\frac{W}{a} \tag{1}$$

$$\mathrm{IE}\ \%=[1-\frac{C_{R(i)}}{C_{R_o}}]\times 100 \tag{2}$$

$$\theta=1-\frac{C_{R(i)}}{C_{R_o}} \tag{3}$$

where W is the mass loss of metallic substrate (mg), a is the area of investigated coupon (cm^2), t is the immersion durations (h) [13, 14].

2.3. Theoretical calculations

The molecular modeling computations were carried out using Gaussian 09 [15]. The inhibitor structure in the gas phase was optimized using the B3LYP method and the principle group "6-31G^{++} (d,p)". According to Koopman's hypothesis [16], the ionization potential (I) and electron affinity (A) correspond to E_{HOMO} and E_{LOMO}, respectively. The ionization potential and electron affinity were calculated using equations 4 and 5, respectively:

$$I=-E_{HOMO} \tag{4}$$

$$A=-E_{LOMO} \tag{5}$$

To determine the hardness (η), softness (σ), and electronegativity (χ), utilize equations 6-8:

$$\chi=\frac{I+A}{2} \tag{6}$$

$$\eta=\frac{I-A}{2} \tag{7}$$

$$\sigma=\eta^{-1} \tag{8}$$

To calculate the proportional number of transported electrons (ΔN), [16] can utilize equation 9:

$$\Delta N=\frac{\chi_{Fe}-\chi_{inh}}{2(\eta_{Fe}+\eta_{inh})} \tag{9}$$

Thus, χ_{Fe} and χ_{inh} referred to iron and inhibitor electronegativities, whereas η_{Fe} and η_{inh} signify to iron and inhibitor hardness respectively.

For the metallic substrate the value of ΔN was determined based Equation 10, and the χ_{Fe} = 7 eV, η_{Fe} = 0 eV [16]:

$$\Delta N=\frac{7-\chi_{inh}}{2(\eta_{inh})} \tag{10}$$

3. Result and Discussion

3.1. Weight loss investigations

Figure 2 presents an overview of the weight loss assay results for metallic samples in HCl without and with the addition of MMPC. The findings show that MMPC protects the coupon surface from corrosion, and its ability to do so increases with its concentration. For a 5-hour exposure, the corrosion rate was slowed down by increasing the MMPC concentration. The maximum inhibitory potency concentration (97.13 %) was observed at 0.5 mM MMPC. It is believed that the large molecular structure of MMPC and the abundance of heteroatoms (three nitrogen atoms plus three oxygen atoms) contribute to the strong inhibitory ability of the material [15].

The corrosion inhibition performance of MMPC was enhanced by increasing its dosage up to 0.5 mM as the MMPC molecules were adsorbed onto the metal sample surface to form a protective barrier. However, when inhibitor concentrations climbed above 0.5 mM and approached 1.0 mM, the inhibitor molecules were attracted to the surface of the steel substrate, virtually retaining the inhibitory efficiency constant.

3.2. The effect of exposure time

The metal substrate was exposed to an HCl solution with inhibitory concentrations ranging from 0.1 to 1.0 mM for 1 to 48 hours at 303 K to examine the effect of exposure duration on the corrosion inhibition efficacy of MMPC (Figure 3). Up to 10 hours of immersion time, rapidly increasing damping efficiency was observed. After that, it decreased steadily to 24 hours, and then more rapidly to 48 hours. By increasing the amount of MMPC adsorbed on the mild steel surface as a result of increasing the concentration and exposure time, the inhibitory efficiency was increased. Additionally, as even more inhibitor molecules were adsorbed on the metallic substrate, the inhibitor's adsorption density notably rose, enabling both Van Der Waals forces (physisorption) and the formation of coordination complexes (chemisorption). If some inhibitor molecules leave the surface, the effective area that the inhibitor covers and the inhibitory activity may both be lowered. Evidence that the inhibitor layer adsorbed in the inhibited media comes from the comparatively high inhibitive efficacy observed over the prolonged immersion period.

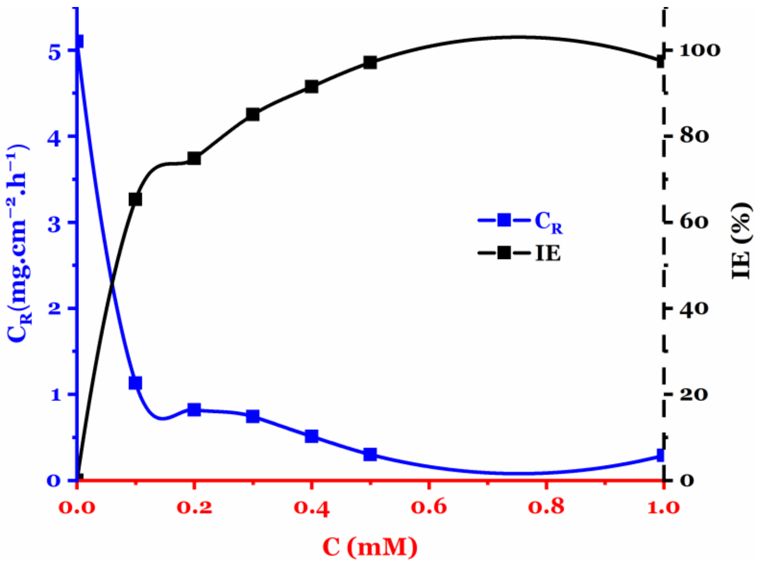

Figure 2: C_R vs IE % for various MMPC concentrations of metallic substrate subjected to corrosive media for 5 hours at 303 K.

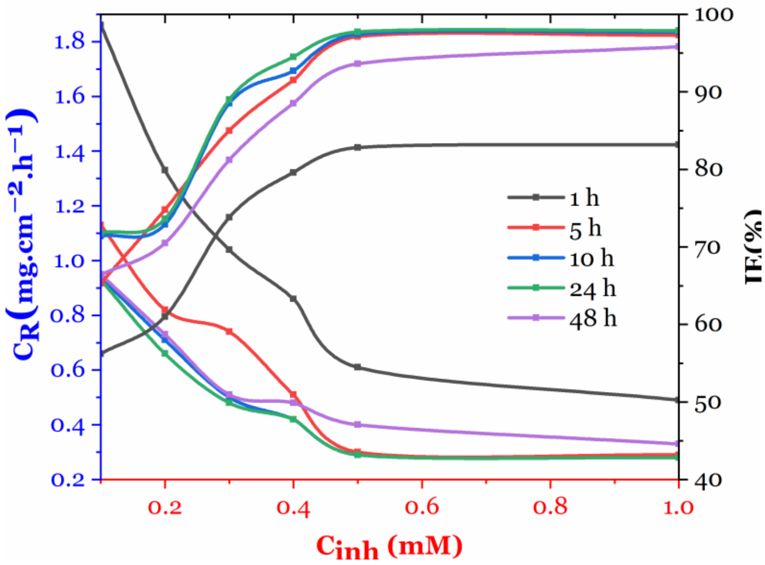

Figure 3: Various dosages effect of MMPC on the C_R and IE % of metallic substrate immersed in 1 M HCl solution for 1 to 48 h at 303 K.

3.3. The effect of temperature

The weight loss method was utilized to investigate the corrosion inhibitory effectiveness of MMPC on mild steel under acidic conditions with various concentrations (0.1-1.0 mM) at different temperatures (303-333 K) after 5 hours of exposure. As shown in Figure 4, at a constant inhibitor concentration, the corrosion rate increased with increasing temperature, while the effectiveness of corrosion protection decreased as the temperature rose from 303 to 333 K. At normal temperatures, MMPC performed optimally. Physisorption was observed, with a decrease in inhibitory activity as the temperature increased at all concentrations. Additionally, at high temperatures, desorption occurs, resulting in the loss of MMPC molecules from the surface of the sample.

3.4. Adsorption isotherm

The comprehension of the interaction between the inhibitor molecules and the metallic substrate is made easier by the adsorption temperature. The surface coverage (θ) value, obtained by graphemetrical measurments, was used to decide which isotherm best fits the data. To ascertain if MMPC molecules attested inhibitor to the surface of the metallic substrate physically or chemically, a number of adsorption isotherms, including the Temkin, Freundlich, and Langmuir isotherms, were utilized to analyze the adsorption mechanism. The regression coefficient (R^2) for the MMPC of 0.9989 and the computed slope and intercept values for the Langmuir isotherms of 9.591E-4 ± 2.21372E-5 and 0.05926 ± 0.01125, respectively at 303 K, show that the Langmuir absorption isotherms appear to suit the data well. Equation 12 and the isothermal plot of Langmuir absorption between C/θ and C are shown in Figure 5

$$\frac{C}{\theta}=\frac{1}{K_{ads}}+C \tag{12}$$

where C is the concentration of MMPCs and K_{ads}, which stands for surface area, is the equilibrium constant.

To use the K_{ads} value and a linear straight fitted plot between C/θ and C, the free energy of adsorption, ΔG^{o}_{ads}, was computed. K_{ads} and ΔG^{o}_{ads} are connected by equation 13 in this way.

$$\Delta G^{o}_{ads} = -RT\ ln(55.5K_{ads}) \tag{13}$$

where T is the temperature, R is the gas constant, and 55.5 is the water content measurement. The "K_{ads}" constant was added to the calculation above to produce the "ΔG^{o}_{ads}" value.

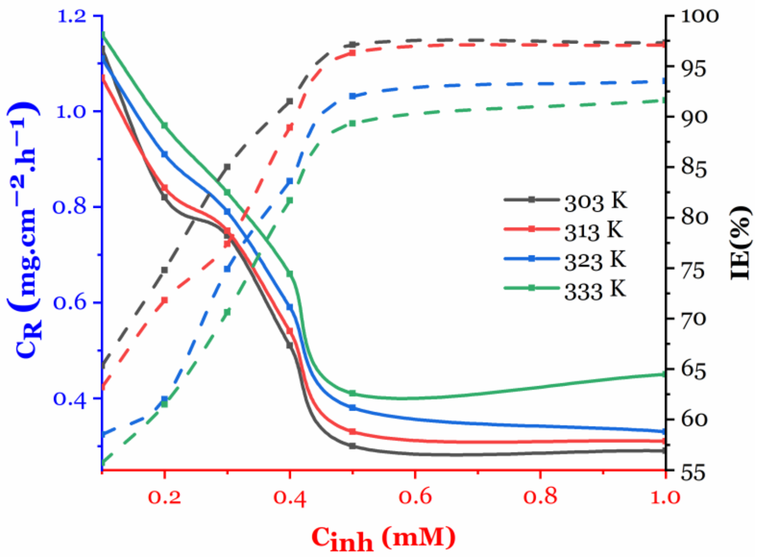

Figure 4: Various dosages effect of MMPC on the C_R and IE % of metallic substrate immersed in 1 M HCl solution for 5 h at 303-333 K.

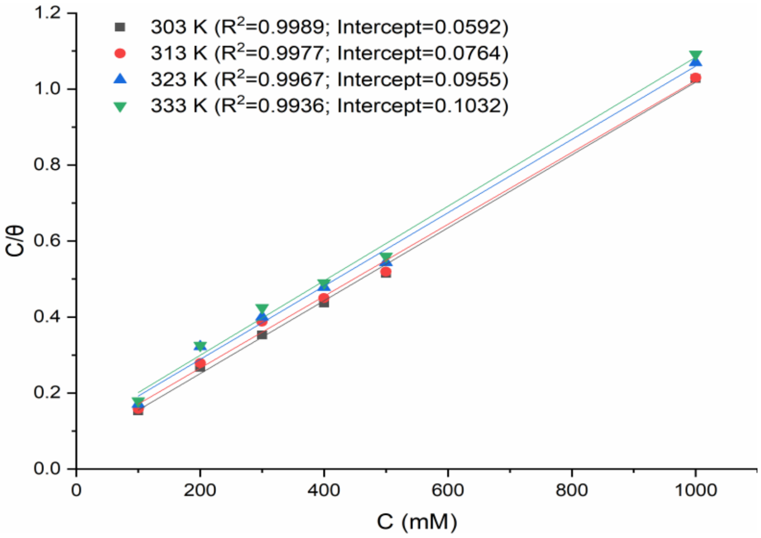

Figure 5: Langmuir adsorption isotherm for metallic substrate in acidic solution at different temperatures.

A value of ΔG^{o}_{ads} approximately or even less negative than -20 kJmol^{-1} suggests physisorption, but a value of ΔG^{o}_{ads} ranging from -40 kJmol^{-1} and larger negative value suggests chemisorption [22, 23]. Physical adsorption and chemical adsorption are two separate adsorption modes, according to the MMPC ΔG^{o}_{ads} value of -37.25 kJmol^{-1}.

3.5. DFT calculations

Numerous applications use density functional theory (DFT) to assess the effectiveness of inhibitors and the behavior of the coupon surface. In this study, geometrical optimization of the tested inhibitor molecule was performed using the DFT/B3LYP approach with the basis set 6-311G^{++}(d,p) and Gaussian 09. Quantum chemical descriptors were calculated using the optimized geometry to determine the ionization potential (IP) and electron affinity (EA). Figure 6 displays the structure of the optimized tested inhibitor molecule. Quantum chemical calculations are frequently employed to explore the reaction mechanism process, which has been verified as an effective way to prevent corrosion activities of chemicals in connection to their electronic structure [17-19]. As a result, the effectiveness of the tested inhibitor to resist corrosion has been studied. Table 2 shows the values of the quantum chemical characteristics, which include E_{HOMO}, E_{LUMO}, ΔE, χ (Electronegativity), Softness (σ), and Hardness (η). The frontier orbitals play an important role in understanding the reactivity of chemical compounds when determining the corrosion behavior of any organic substance [20]. The values for E_{HOMO}, E_{LUMO}, and ΔE are -9.067, -4.203, and 4.864 eV, respectively. A lower E_{LUMO} is accountable for mild steel's ability to receive electrons into the vacant d-orbital of the inhibitor, and a lower E boosts corrosion efficiency. E_{HOMO} is responsible for the compound's ability to donate electrons; the higher the E_{LUMO}, the better the compound's donating potential. This determines the covalent bond's polarity and the distribution of charges that enable molecules to adsorb on metallic surfaces, making the tested inhibitor an effective corrosion inhibitor. The electronegativity (χ) value of 6.635 eV, which explains how the molecule attracts electrons toward itself, and a higher electronegativity leads to better inhibition efficiency, are other quantum chemical property values that help to explain the potential of the tested inhibitor as a corrosion inhibitor. The computed values for the ionization energy (I), hardness (η), softness (σ), and electron affinity energy are shown in Table 2 as 9.067, 2.432, 0.41118, and 4.203 eV, respectively. A greater E_{HOMO} offers low ionization energy and electron affinity, which leads to improved inhibition efficiency. As a result, the tested inhibitor is a better inhibitor to corrosion on mild steel. Ionization and electron affinity describe the properties of compounds based on electron density. Additionally, the hardness and softness listed in Table 2 were verified. This information illustrates the compound's molecular stability and reactivity and is favorable for preventing corrosion on mild steel.

Table 2: Quantum chemical parameters of tested inhibitor molecule.

Inhibitor	E_{HOMO}	E_{LUMO}	ΔE	χ	σ	η	I	A	ΔN
MMPC	-9.067 eV	-4.203 eV	4.864 eV	6.635	0.41118	2.432	9.067 eV	4.203 eV	0.075

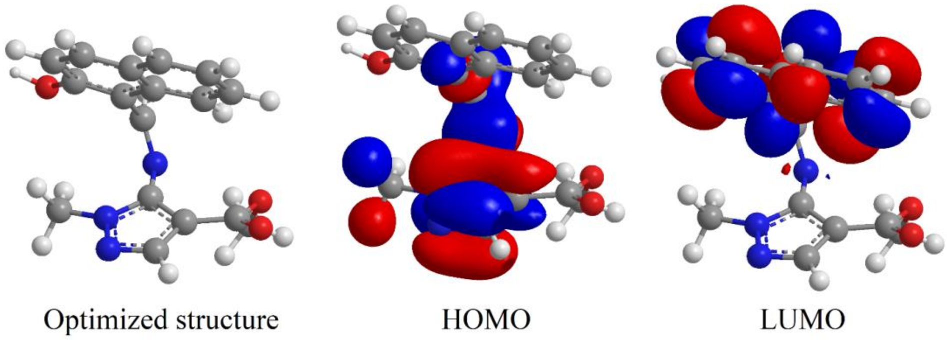

Figure 6: Optimized structure, HOMO, and LUMO for the AAQQQ4 tested inhibitor molecule.

3.6. Mechanism of inhibition

Corrosion is the process by which materials deteriorate due to chemical reactions with their environment, typically involving oxidation or reduction reactions. Corrosion inhibitors are substances that can be added to a system to prevent or slow down the corrosion process [21-23].

Organic synthesized inhibitors are a common type of corrosion inhibitor that work by forming a protective film on the metal surface, which helps to prevent or slow down the corrosion process. The mechanism of corrosion inhibition by organic synthesized inhibitors can be explained in the following steps:

1. Adsorption: The inhibitor molecules adsorb onto the metal surface by weak chemical forces, such as Van der Waals forces, electrostatic forces, and hydrogen bonding. The adsorption process is influenced by factors such as the chemical structure and size of the inhibitor molecules, the nature of the metal surface, and the pH and temperature of the solution.
2. Formation of a protective film: The adsorbed inhibitor molecules react with the metal ions and other species in the corrosive environment to form a protective film on the metal surface. This film acts as a barrier between the metal and the corrosive environment, preventing or slowing down the corrosion process.
3. Inhibition of cathodic and anodic reactions: The inhibitor molecules can also inhibit the cathodic and anodic reactions that occur during the corrosion process. For example, the inhibitor can block the reaction sites on the metal surface where oxygen reduction occurs during the cathodic reaction. This inhibition reduces the rate of the corrosion process.

The effectiveness of an organic synthesized inhibitor depends on a number of factors, including the chemical structure of the inhibitor, the concentration of the inhibitor in the solution, and the nature of the corrosive environment. These factors need to be optimized to achieve the best corrosion inhibition performance.

Using weight loss measurements, it was observed that the chemical azomethine forms protective films against mild steel corrosion in hydrochloric acid medium. The inhibition efficiency increases with higher inhibitor concentrations. When 0.5 mM of the inhibitor was present at 303 K for 5 hours of immersion, the material showed a protective capacity between 65 and 97 %. The investigated inhibitor utilizes the Langmuir model, which takes into account both decomposition and chemisorption adsorption at the metal interface. Figure 7 illustrates the adsorption of an imine molecule on the metal surface, showing the chemical attraction of the unshared electron pairs of the azomethine molecule to the unoccupied iron d-orbitals of the metallic substrate surface, as well as the electrostatic attractions of the negatively charged steel surface.

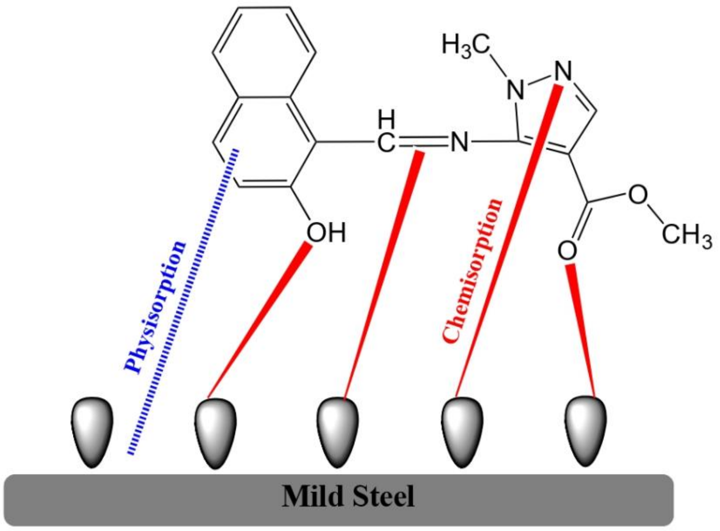

Figure 7: The suggested mechanism of tested inhibitor molecule on mild steel surface in in corrosive solution.

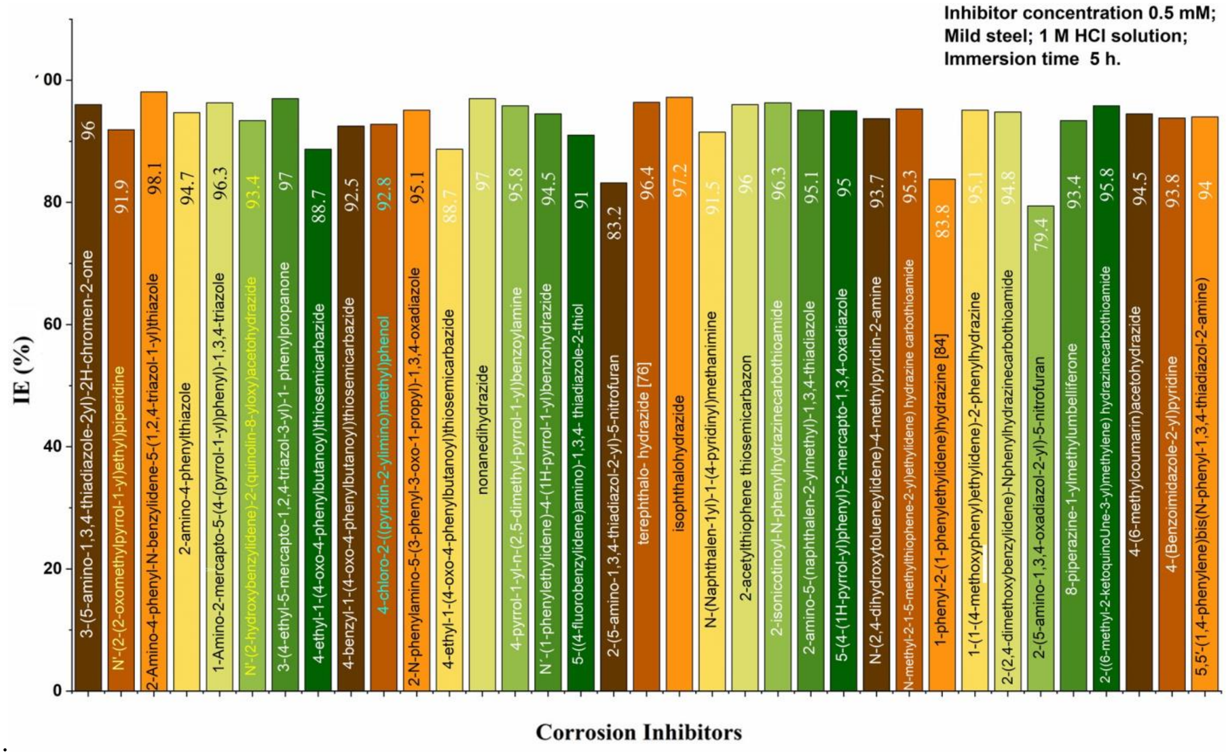

Figure 8: Comparison between several synthesized organic corrosion inhibitors.

3.7. Comparison studies

In this research, we conducted a comparative analysis of the inhibitory effectiveness of various organic corrosion inhibitors that have been previously synthesized and published [24, 56]. We evaluated the inhibitory efficiency of each inhibitor and presented our findings in Figure 8.

Figure 8 provides an overview of the inhibition efficiencies of several synthesized organic corrosion inhibitors. The chart displays the inhibitors' inhibition efficiency as a percentage, with a higher percentage indicating a more effective inhibition. The inhibitors are identified on the x-axis, and the y-axis represents the percentage of inhibition efficiency.

The comparison enables us to determine which synthesized organic corrosion inhibitor is the most effective at inhibiting corrosion. This information can help in selecting the most suitable inhibitor for specific applications, such as in the chemical, petroleum, or manufacturing sectors. Furthermore, the study's results may offer insights into the mechanisms of corrosion inhibition and guide future research and development of corrosion inhibitors.

4. Conclusions

In conclusion, the research findings show that MMPC is an effective inhibitor for preventing the corrosion of mild steel in a 1 M hydrochloric acid medium. The use of weight loss measurements and theoretical calculations, including the Langmuir adsorption isotherm model and Density Functional Theory, provided insight into the mechanism and effectiveness of the corrosion protection. The results indicate that MMPC adsorbs onto mild steel, blocking active sites and exhibiting excellent inhibitor effectiveness of 97.13 % at a concentration of 0.5 mM and 303 K. Overall, this study offers valuable insights into the development of effective inhibitors for protecting metallic materials, particularly in the oil and gas industry, where corrosion is a significant challenge.

5. References

1. G. E. Badr, The role of some thiosemicarbazide derivatives as corrosion inhibitors for C-steel in acidic media, *Corros, Sci*., 51(2009), b2529-2536.
2. M. Goyal, S. Kumar, I. Bahadur, C. Verma, E. Ebenso, Organic corrosion inhibitors for industrial cleaning of ferrous and non-ferrous metals in acidic solutions: A review, *J. Mol. Liq.*, 256(2018), 565-573.
3. S. Ghareba, S. Omanovic, Interaction of 12-aminododecanoic acid with a carbon steel surface: towards the development of ‘green’ corrosion inhibitors, *Corros. Sci.*, 52(2010), 2104-2113.
4. A. Yıldırım, M. Cetin, Synthesis and evaluation of new long alkyl side chain acetamide, isoxazolidine and isoxazoline derivatives as corrosion inhibitors, *Corros. Sci.*, 50(2008), 155-165.
5. S. K. Saha, A. Dutta, P. Ghosh, D. Sukul, P. Banerjee, P. Novel, Schiff-base molecules as efficient corrosion inhibitors for mild steel surface in 1 M HCl medium: experimental and theoretical approach, *Phys. Chem. Chem. Phys.*, 18(2016), 17898-17911.
6. X. Li, S. Deng, H. Fu, Three pyrazine derivatives as corrosion inhibitors for steel in 1.0 M H_2SO_4 solution, *Corros. Sci.*, 53(2011), 3241-3247.
7. M. Karelson, V. Lobanov, A. Katritzky Quantum-chemical descriptors in QSAR/QSPR studies, *Chem. Rev.*, 96(1996), 1027-1044.
8. J. Kumaran, S. Priya, J. Gowsika, N. Jayachandramani, S. Mahalakshmi, Synthesis, Spectroscopic Characterization, In silico DNA studies and antibacterial activites of copper(II) and zinc(II) complexes derived from thiazole based pyrazolone derivatives, *Res. J. Pharm. Biol. Chem. Sci*., 4(2013), 279-288.
9. M. M. El-Naggar, Bis-aminoazoles corrosion inhibitors for copper in 4 0 M HNO_3 solutions, *Corros. Sci.*, 42(2000), 773-789.
10. I. Lukovits, E. Kálmán, F. Zucchi, Corrosion inhibitors-correlation between electronic structure and efficiency, *Corrosion*, 57(2001), 3-14.
11. O. Kikuchi, Systematic QSAR procedures with quantum chemical descriptors, *Quant. Struct.-Act. Relat*., 6(1987), 179-188.
12. K. F. Khaled, K. F. Scientific fraud in corrosion science research: a review, *Res. Chem. Intermediates*, 40(2014), 1735-1752.
13. ASTM International, Standard Practice for Preparing, Cleaning, and Evaluating Corrosion Test., 2011, pp 1-9.
14. NACE International, Laboratory Corrosion Testing of Metals in Static Chemical Cleaning Solutions at Temperatures below 93 °C (200 F), TM0193-2016-SG, 2000.
15. Gaussian 09, Revision D.01, M. J. Frisch, G. W. Trucks, H. B. Schlegel, G. E. Scuseria, M. A. Robb, J. R. Cheeseman, G. Scalmani, V. Barone, B. Mennucci, G. A. Petersson, H. Nakatsuji, M. Caricato, X. Li, H. P. Hratchian, A. F. Izmaylov, J. Bloino, G. Zheng, J. L. Sonnenberg, M. Hada, M. Ehara, K. Toyota, R. Fukuda, J. Hasegawa, M. Ishida, T. Nakajima, Y. Honda, O. Kitao, H. Nakai, T. Vreven, J. A. Montgomery, Jr., J. E. Peralta, F. Ogliaro, M. Bearpark, J. J. Heyd, E. Brothers, K. N. Kudin, V. N. Staroverov, R. Kobayashi, J. Normand, K. Raghavachari, A. Rendell, J. C. Burant, S. S. Iyengar, J. Tomasi, M. Cossi, N. Rega, J. M. Millam, M. Klene, J. E. Knox, J. B. Cross, V. Bakken, C. Adamo, J. Jaramillo, R. Gomperts, R. E. Stratmann, O. Yazyev, A. J. Austin, R. Cammi, C. Pomelli, J. W. Ochterski, R. L. Martin, K. Morokuma, V. G. Zakrzewski, G. A. Voth, P. Salvador, J. J. Dannenberg, S. Dapprich, A. D. Daniels, Ö. Farkas, J. B. Foresman, J. V. Ortiz, J. Cioslowski, and D. J. Fox, Gaussian, Inc., Wallingford CT, (2009).
16. T. Koopmans, Ordering of wave functions and eigenenergies to the individual electrons of an atom, *Physic*a, 1(1933), 104-113.
17. L. Larabi, Y. Harek, O. Benali, S. Ghalem, Hydrazide derivatives as corrosion inhibitors for mild steel in 1 M HCl, *Prog. Org. Coat.*, 54(2005), 256-262.
18. I. Lukovits, E. Kálmán, F. Zucchi, Corrosion

inhibitors-correlation between electronic structure and efficiency, *Corrosion*, 57(2001), 3-14.

19. A. Zarrouk, A. Dafali, B. Hammouti, H. Zarrok, S. Boukhris, M. Zertoubi, Synthesis, characterization and comparative study of functionalized quinoxaline derivatives towards corrosion of copper in nitric acid medium, *Int. J. Electrochem. Sci.*, 5(2010), 46-53.
20. A. Fiala, A. Chibani, A. Darchen, A. Boulkamh, K. Djebbar, Investigations of the inhibition of copper corrosion in nitric acid solutions by ketene dithioacetal derivatives, *Appl. Surf. Sci.*, 253(2007), 9347.
21. Q. Jawad, D. Zinad, R. Salim, A. Al-Amiery, T. Gaaz, M. Takriff, A. Kadhum, Synthesis, characterization, and corrosion inhibition potential of novel thiosemicarbazone on mild steel in sulfuric acid environment, *Coatings*, 9(2019), 729-736.
22. I. Aziz, M. Abdulkareem, I. Annon, M. Hanoon, M. Al-Kaabi, L. Shaker, A. Alamiery, W. Wan Isahak, M. Takriff, Weight Loss, Thermodynamics, SEM, and electrochemical studies on N-2-methylbenzylidene-4-antipyrineamine as an inhibitor for mild steel corrosion in hydrochloric acid, *Lubricants*, 10(2022), 23-36.
23. A. Al-Amiery, A. Kadhum, A. Kadihum, A. Mohamad, C. How, S. Junaedi, Inhibition of mild steel corrosion in sulfuric acid solution by new schiff base, *Materials*, 7(2014), 787-804.
24. I. Alkadir Aziz, I.A. Annon, M. Abdulkareem, M. Hanoon, M. Alkaabi, L. Shaker, A. Alamiery, W. Wan Isahak, M. Takriff, Insights into corrosion inhibition behavior of a 5-mercapto-1,2,4-triazole derivative for mild steel in hydrochloric acid solution: experimental and DFT studies, *Lubricants*, 9(2021), 122-132
25. K. Al-Azawi, S. Al-Baghdadi, A. Mohamed, A. Al-Amiery, T. Abed, S. Mohammed, A. Kadhum, A. Mohamad, Synthesis, inhibition effects and quantum chemical studies of a novel coumarin derivative on the corrosion of mild steel in a hydrochloric acid solution, *Chem. Central J.*, 10(2016), 1-9
26. A. Alamiery, Study of corrosion behavior of N'-(2-(2-oxomethylpyrrol-1-yl) ethyl) piperidine for mild steel in the acid environment, *Biointerface Res. Appl. Chem.*, 12(2022), 3638-3646
27. A. Al-Amiery, A. Mohamad, A. Kadhum, l. Shaker, W. Isahak, M. Takriff, Experimental and theoretical study on the corrosion inhibition of mild steel by nonanedioic acid derivative in hydrochloric acid solution, *Sci. Rep*., 12(2022), 1-21.
28. A. Alamiery, A. Mohamad, A. Kadhum, S. Takriff, Comparative data on corrosion protection of mild steel in HCl using two new thiazoles, *Data* Brief, 40(2022), 107838
29. A.M. Mustafa, F.F. Sayyid, N. Betti, L.M. shaker, M.M. Hanoon, A.A. Alamiery, A.A.H. Kadhum, M.S. Takriff, Inhibition of mild steel corrosion in hydrochloric acid environment by 1-amino-2-mercapto-5-(4-(pyrrol-1-yl)phenyl)-1,3,4-triazole, *South African J. Chem. Eng.*, 39(2022), 42-51.
30. A. Alamiery, Investigations on corrosion inhibitory effect of newly quinoline derivative on mild steel in HCl solution complemented with antibacterial studies, *Biointerface Res. Appl. Chem*., 12(2022), 1561-1568
31. A. Aziz, I.A. Annon, M. Abdulkareem, M. Hanoon, M. Alkaabi, L. Shaker, A. Alamiery, W. Wan Isahak, M. Takriff, Insights into corrosion inhibition behavior of a 5-mercapto-1,2,4-triazole derivative for mild steel in hydrochloric acid solution: experimental and DFT etudies, *Lubricants*, 9(2021), 122-134.
32. A. Alamiery, W. Isahak, M. Takriff, Inhibition of mild steel corrosion by 4-benzyl-1-(4-oxo-4-phenylbutanoyl)thiosemicarbazide: Gravimetrical, adsorption and theoretical studies, *Lubricants*, 9(2021), 93-109.
33. M.A. Dawood, Z.M.K. Alasady, M.S. Abdulazeez, D.S. Ahmed, G.M. Sulaiman, A.A.H. Kadhum, L.M. Shaker and A.A. Alamiery, The corrosion inhibition effect of a pyridine derivative for low carbon steel in 1 M HCl medium: Complemented with antibacterial studies, *Int. J. Corros. Scale Inhib.*, 10(2021), 1766-1782.
34. A. Alamiery, Corrosion inhibition effect of 2-N-phenylamino-5-(3-phenyl-3-oxo-1-propyl)-1,3,4-oxadiazole on mild steel in 1 M hydrochloric acid medium: Insight from gravimetric and DFT investigations, *Mater. Sci. Energy Technol.*, 4(2021), 398-406.
35. A. Alamiery, Short report of mild steel corrosion in 0.5 m H_2SO_4 by 4-ethyl-1-(4-oxo-4-phenylbutanoyl) thiosemicarbazide, *J. Tribol*, 30(2021), 90-99.
36. A. Alamiery, Anticorrosion effect of thiosemicarbazide derivative on mild steel in 1 M hydrochloric acid and 0.5 M sulfuric acid: gravimetrical and theoretical studies, *Mater. Sci. Energy Technol.*, 4(2021), 263-273.
37. A. Alamiery, W. Isahak, H. Aljibori, H. Al-Asadi, A. Kadhum, Effect of the structure, immersion time and temperature on the corrosion inhibition of 4-pyrrol-1-yl-n-(2,5-dimethyl-pyrrol-1-yl)benzoylamine in 1.0 m HCl solution, *Int. J. Corros. Scale Inhib.*, 10(2021), 700-713.
38. A. Alamiery, E. Mahmoudi and T. Allami, Corrosion inhibition of low-carbon steel in hydrochloric acid environment using a Schiff base derived from pyrrole: gravimetric and computational studies, *Int. J. Corros. Scale Inhib.*, 10(2021), 749-765.
39. A.J.M. Eltmimi, A. Alamiery, A.J. Allami, R.M. Yusop, A.H. Kadhum, T. Allami, Inhibitive effects of a novel efficient Schiff base on mild steel in hydrochloric acid environment, *Int. J. Corros. Scale Inhib.*, 10(2021), 634-648.
40. A. Alamiery, L. Shaker, A. Allami, A. Kadhum, M. Takriff, A study of acidic corrosion behavior of Furan-Derived schiff base for mild steel in hydrochloric acid environment: Experimental, and surface investigation, *Mater. Today: Proc.*, 44(2021), 2337-2341.
41. S. Al-Baghdadi, A. Al-Amiery, T. Gaaz, A. Kadhum, Terephthalohydrazide and isophthalo-hydrazide as new corrosion inhibitors for mild steel in hydrochloric acid: Experimental and theoretical approaches, *Koroze*

Ochrana Materialu, 65(2021), 12-22.

42. M. Hanoon, A. Resen, L. Shaker, A. Kadhum, A. Al-Amiery, Corrosion investigation of mild steel in aqueous hydrochloric acid environment using n-(Naphthalen-1yl)-1-(4-pyridinyl)methanimine complemented with antibacterial studies, *Biointerface Res. Appl. Chem.*, 11(2021), 9735-9743.
43. S. Al-Baghdadi, T. Gaaz, A. Al-Adili, A. Al-Amiery, M. Takriff, Experimental studies on corrosion inhibition performance of acetylthiophene thiosemicarbazone for mild steel in HCl complemented with DFT investigation, *Inter. J. Low-Carbon Technol.*, 16(2021), 181-188.
44. A. Al-Amiery, Anti-corrosion performance of 2-isonicotinoyl-n-phenylhydrazinecarbothioamide for mild steel hydrochloric acid solution: Insights from experimental measurements and quantum chemical calculations, *Surf. Rev. Lett.*, 28(2021), 2050058.
45. M. S. Abdulazeez, Z. S. Abdullahe, M. A. Dawood, Z.K. Handel, R.I. Mahmood, S. Osamah, A.H. Kadhum, L. M. Shaker, A. A. Al-Amiery, Corrosion inhibition of low carbon steel in HCl medium using a thiadiazole derivative: weight loss, DFT studies and antibacterial studies, *Int. J. Corros. Scale Inhib.*, 10(2021), 1812-1828.
46. A. Mustafa, F. Sayyid, N. Betti, M. Hanoon, A. Al-Amiery, A. Kadhum, M. Takriff, Inhibition Evaluation of 5-(4-(1H-pyrrol-1-yl)phenyl)-2-mercapto-1,3,4-oxadiazole for the corrosion of mild steel in an acidic environment: thermodynamic and DFT aspects, *Tribologia-Finnish J. Tribol.*, 38(2021), 39-47.
47. Y. M. Abdulsahib, A. J. M. Eltmimi, S.A. Alhabeeb, M.M. Hanoon, A. A. Al-Amiery, T. Allami, A. A. H. Kadhum, Experimental and theoretical investigations on the inhibition efficiency of N-(2,4-dihydroxytolueneylidene)-4-methylpyridin-2-amine for the corrosion of mild steel in hydrochloric acid, *Int. J. Corros. Scale Inhib.*, 10(2021), 885-899.
48. A. Khudhair, A. Mustafa, M. Hanoon, A. Al-Amiery, L. Shaker, T. Gazz, A. Mohamad, A. Kadhum, M. Takriff, Experimental and theoretical investigation on the corrosion inhibitor potential of N-MEH for mild steel in HCl, *Prog. Color Colorant Coat.*, 15(2021), 111-122.
49. D. Zinad, R. Salim, N. Betti, L. Shaker, A. AL-Amiery, Comparative investigations of the corrosion inhibition efficiency of a 1-phenyl-2-(1-phenylethylidene)hydrazine and its analog against mild steel corrosion in hydrochloric acid solution, *Prog. Color Colorants Coat.*, 15(2021), 53-63
50. R. Salim, N. Betti, M. Hanoon, A., Al-Amiery, 2-(2,4-Dimethoxybenzylidene)-N-Phenylhydrazinecarbothioamide as an Efficient Corrosion Inhibitor for Mild Steel in Acidic Environment, *Prog. Color Colorants Coat.*, 15(2021), 45-52
51. A. Al-Amiery, L. Shaker, A. M. Takriff, Exploration of furan derivative for application as corrosion inhibitor for mild steel in hydrochloric acid solution: Effect of immersion time and temperature on efficiency, *Mater. Today: Proc.*, 42(2021), 2968-2973
52. A. M. Resen, M. M. Hanoon, W. K. Alani, A. Kadhim, A. A. Mohammed, T. S. Gaaz4, A. A. H. Kadhum, A. A. Al-Amiery, M. S. Takriff, Exploration of 8-piperazine-1-ylmethylumbelliferone for application as a corrosion inhibitor for mild steel in hydrochloric acid solution, *Int. J. Corros. Scale Inhib.*, 10(2021), 368-387.
53. M. Hanoon, A. Resen, A. Al-Amiery, A. Kadhum, T. Takriff, Theoretical and experimental studies on the corrosion inhibition potentials of 2-((6-Methyl-2-ketoquinolin-3-yl)methylene) hydrazinecarbothio-amide for mild steel in 1 M HCl, *Prog. Color Colorants Coat.*, 15(2021), 21-33.
54. F. Hashim, T. Salman, S. Al-Baghdadi, T. Gaaz, A. Al-Amiery, Inhibition effect of hydrazine-derived coumarin on a mild steel surface in hydrochloric acid, *Tribologia*, 37(2020), 45-53.
55. A. M. Resen, M. Hanoon, R. D. Salim, A. A. Al-Amiery, L. M. Shaker, A. A. H. Kadhum, Gravimetrical, theoretical, and surface morphological investigations of corrosion inhibition effect of 4-(benzoimidazole-2-yl) pyridine on mild steel in hydrochloric acid, *Koroze Ochrana Materialu*, 64(2020), 122-130.
56. A. Salman, Q. Jawad, K. Ridah, L. Shaker, A. Al-Amiery, Selected BIS-thiadiazole: synthesis and corrosion inhibition studies on mild steel in HCl environment, *Sur. Rev. Lett.*, 27(2020), 2050014.

How to cite this article:
A. Naseef Jasim, B. A. Abdulhussein, S. Mohammed Noori Ahmed, W. K. Al-Azzawi, M. M. Hanoon, M. K. Abbass, A. A. Al-Amiery, Schiff's Base Performance in Preventing Corrosion on Mild Steel in Acidic Conditions. Prog. Color Colorants Coat., 16 (2023), 319-329.

PROGRESS
IN COLOR, COLORANTS AND COATINGS

available online @ www.pccc.icrc.ac.ir
Progress in Color Colorants Coating 16 (2023), 331-345

Ministry of Science, Research and Technology
Institute for Color Science & Technology

Optical and Physical Properties for the Nanocomposite Poly(vinyl chloride) with Affected of Carbon Nanotube and Nano Carbon

A. M. Abdullah[1], L. H. Alwan[1], A. A. Ahmed[2], R. N. Abed[3*]
[1] Department of Chemistry, College of Education, University of Samarra, P.O. Box: 64546, Salah Al Din, Iraq
[2] Polymer Research Unit, College of Science, Al-Mustansiriyah University, P.O. Box: 10052, Baghdad, Iraq
[3] Department of Mechanical Engineering, College of Engineering, Al-Nahrain University, P.O. Box: 64040, Jadria, Baghdad, Iraq

ARTICLE INFO

Article history:
Received: 6 Jan 2023
Final Revised: 25 Mar 2023
Accepted: 27 Mar 2023
Available online: 22 Aug 2023

Keywords:
PVC
PVC-CNT
Optical conductivity
Topography roughness
Synthesis

ABSTRACT

In this paper, the new nanocomposite thin films of carbon nanotube (CNT) and nano carbon (CN) implanted in PVC matrix were produced by casting technique. The influence of nanomaterials (CNT+CN) was studied on the optical properties and structure of PVC nanocomposite thin films (PVC-CNT, PVC-CN, and PVC-CNT-CN) by utilizing a microscope, AFM device, and computerized diffused reflectance of UV-Visible. The energy gap, absorption coefficient, reflectance, extinction factor, refractive index, and urbach energy have been studied. The reflectance and transmittance of the nanocomposite thin films (PVC-CNT, PVC-CN, and PVC-CNT-CN) were decreased compared with blank PVC after being dispersed (CNT+CN) in the PVC matrix. The dielectric constant and conductivity of nanocomposite thin films also increased after adding nanomaterials (CNT+CN). The direct energy gap and indirect energy gap were decreased for the nanocomposite thin films (PVC-CNT, PVC-CN, and PVC-CNT-CN) compared with the energy gap of blank PVC, where, urbach energy of nanocomposite thin films (PVC-CNT, PVC-CN, and PVC-CNT-CN) increased after addition the nanomaterials (CNT+CN) to the PVC matrix. The SEM images were used to show the shape of carbon nanotube (CNT) and nano carbon (CN). The surface topography was tested by the AFM device and it found the roughness of the nanocomposite thin films (PVC-CNT, PVC-CN, and PVC-CNT-CN) were increased compared with the blank PVC. The application of nanocomposite thin films (PVC-CNT, PVC-CN, and PVC-CNT-CN) was used in many applications like optical clarity, high mechanical strength, and thermal gas barrier. Prog. Color Colorants Coat. 16 (2023), 331-345© Institute for Color Science and Technology.

1. Introduction

The production of plastic is vastly utilized in communication cable packaging, medical fields, food packing, and in many fields due to outstanding their mechanical and chemical resistance with lightweight and lower cost [1]. Poly(vinyl chloride) is the one type of plastic that is used as a polymer in many research applications, it has a simple modification, cheap thermo-plastic, economic formation, and flame retardancy, thereby used in thin films [2]. Therefore, PVC at high temperatures is unsteady out of the application in molding, consequently, the addition of reinforcement

---

*Corresponding author: * rasheed.n.abed@nahrainuniv.edu.iq
rasheednema@yahoo.com

Doi: 10.30509/pccc.2023.167082.1198

material to be stabilized and through the processing [3]. The reinforcement materials such NPs as titanium oxide (TiO_2), chromium oxide (Cr_2O_3), cobalt oxide (Co_3O_4), nickel oxide (NiO), copper oxide (CuO), graphene (Gr), multi-walled nanotube (MWNT), carbon nanotube (CNT), and carbon nano (CN) are added to polymer structure enhanced its properties via preparing new nanocomposite of polymer PVC, that it is used in optical clarity, high mechanical strength, thermal gas barrier [4-7].

In the present work, the nanocomposite thin films of PVC are reinforced by carbon nanotube (CNT) and carbon nano (CN), which is regarded as a nanofiller material inside the PVC matrix. So, the single-walled carbon nanotube (CNT) has extraordinary properties that are utilized in many applications as a nanofiller in the nanocomposite, when adds to the PVC structure and gives it electrical transport properties and high thermal stabilization [8, 9]. MWCNT was used in PVC matric that dissolved in THF to study the effect of thermal, electrical, and dispersion within the PVC structure [10]. The nanocomposite-MWCNTs were synthesizes and dissolved in THF and cast as a film, where the addition of MWCNTs increased the electrical conductivity for these nanocomposite thin films due to the change in PVC structure and penetrate MWCNTs within PVC lattice [11]. Likewise, PVC-nanocomposite thin films have been prepared with various contents of MWCNTs, these thin films are hit by plasma irradiation to give a fine dispersion of MWCNTs within the PVC matrix. the resulting thin films gained good AC electrical conductivity, thermal stability, and a good dielectric constant layer [12, 13]. But regarding of carbon nano (CN) is used in the present work with carbon nanotube (CNT) to improve the structure of PVC. The thin films which were fabricated give nanocomposite good electrical conductivity with high absorption.

The present work aims to fabricate thin films consisting of PVC-CNT, PVC-CN, and PVC-CNT-CN and study the effect of CNT and CN on the PVC structure to show the optical properties of these films, compared with blank PVC. These thin films with nanomaterials improved the absorbance, refractive index, energy gap, dielectric constant, and urbach energy. To our knowledge, there is no one using carbon nano (CN) with PVC. the SEM device was used to show the shape of carbon nanotube (CNT) and nano carbon (CN). The nanocomposite thin films (PVC-CNT, PVC-CN, and PVC-CNT-CN) are used in many applications like optical clarity, high mechanical strength, and thermal gas barrier.

2. Experimental

2.1. Materials

The material of pure PVC bought from Turkey, Istanbul (PetKim Petrokimya), carbon nanotube, and carbon nano have been synthesized in the lab.

2.2. Synthesis carbon nanotube and nano carbon

The carbon nanotube (CNT) and carbon nano (CN) were synthesized in the lab. Primely, preparation of carbon nanotube (CNT) by taking 1 g of reeds with 3 g from NaOH (1:3 wt. %), they were mixed and put in the furnace at 550 ^{o}C for 1 h, every 1 min raise the temperature 10 ^{o}C, at this degree the calcination has happened. The output was cooled at room temperature and washed with hot water many times using Hcl to normalize the pH degree (pH=7) and get rid of NaOH, then the wetted mass was left to dry at 80 ^{o}C for 12 h. Secondly, the same method above was used to produce nano carbon (CN), but the difference was in burning the reeds with NaOH at 700 ^{o}C for 3 h in the furnace. A scheme (1) shows the synthesis of carbon nanotube (CNT) and carbon nano (CN) in different temperatures of calcination.

2.3. Preparation thin film

The PVC nanocomposite thin films were prepared in these steps. In step one, the blank PVC thin film was produced with 1 g of PVC in 100 mL of THF to be 1 % wt. of the mixture. The mixture is blended with a stirrer and raised the temperature to 75 ^{o}C, then the solution is poured into the glass template. In step two, the nanocomposite thin film of (PVC+CNT) was prepared by taking 0.05 g from carbon nanotube (CNT) added to the PVC mixture and blended by a stirrer and then in a sonication device to dissolve the CNT with the mixture. Finally, in step three, the nanocomposite thin film of (PVC+CN) was prepared at the same method by taking 0.05 g from the carbon nano (CN) to the PVC mixture. The nanocomposite thin film (PVC+CNT+CN) was prepared by taking (0.025CNT+0.025CN) with a PVC mixture. All these nanocomposite films were poured into a glass template 40 μm thick and were left under vacuum circular glass, to protect these thin films from any environmental effect. Scheme 2 shows the preparation of synthesis the nanocomposite thin films of PVC with CNT and CN.

2.4. Characterization techniques devices

The samples were inspected by the reflectance device Avantes (DH-S-BAL-2048, UV-Visible Spectro-2048) in the wavelength range (250-1300 nm) for 0.5 step wavelength. The microscope image MK 1000 and MEIJI equipped is inspected with central processor controller with INSTEC hot stage, that was connected to Lumenera color, that have 20x magnifying powers. It used for signify the morphology of the surface. The AA2000 AFM device is employed to assign the particles size of roughness for the blank PVC and PVC-CNT, PVC-CN, PVC-CNT-CN nanocomposite thin films.

The scanning electron microscopy (SEM) S50 with a low vacuum (3 nm at 30 kV SE) was used to show the shape after burned, where the carbon nanotube after calcination at 550 ^{o}C shown in Figure 1a and nano carbon after calcination at 700 ^{o}C shown in Figure 1b.

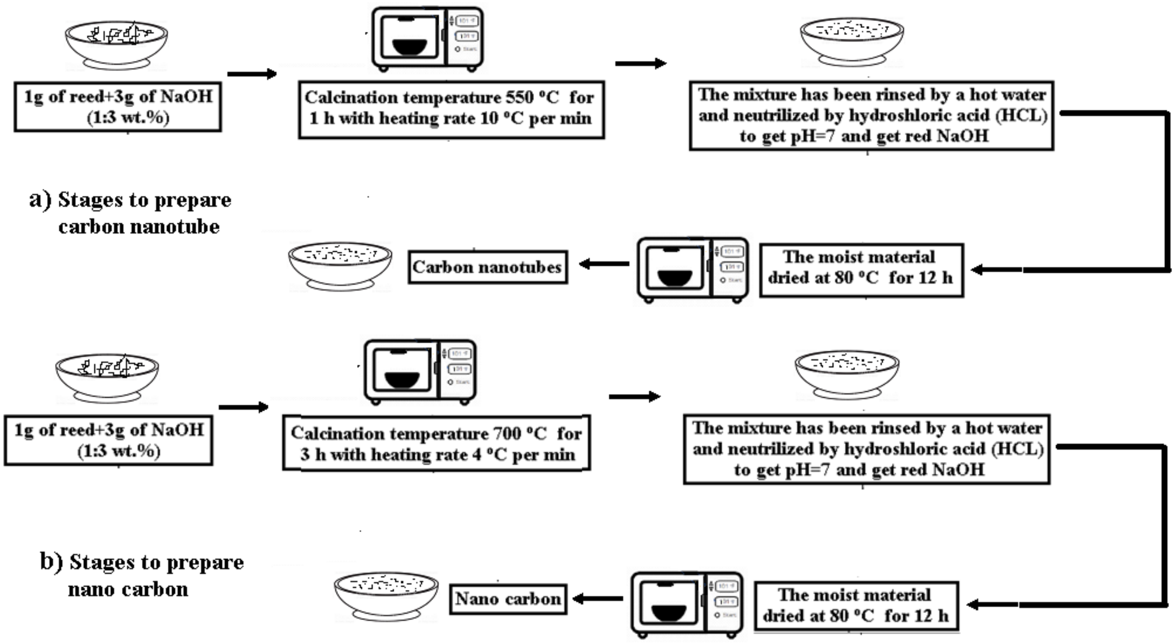

Scheme 1: Described the stages to synthesis: a) carbon nanotubes (CNT) and b) nanocarbon (CN).

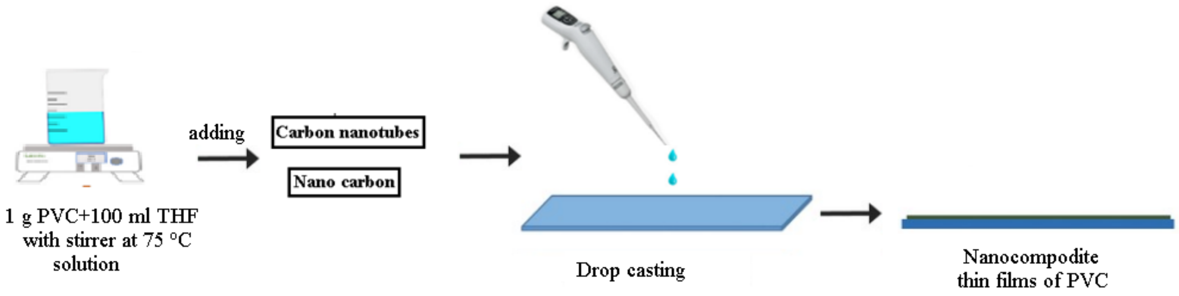

Scheme 2: Synthesis the nanocomposite thin films of PVC with carbon nanotube (CNT) and carbon nano (CN).

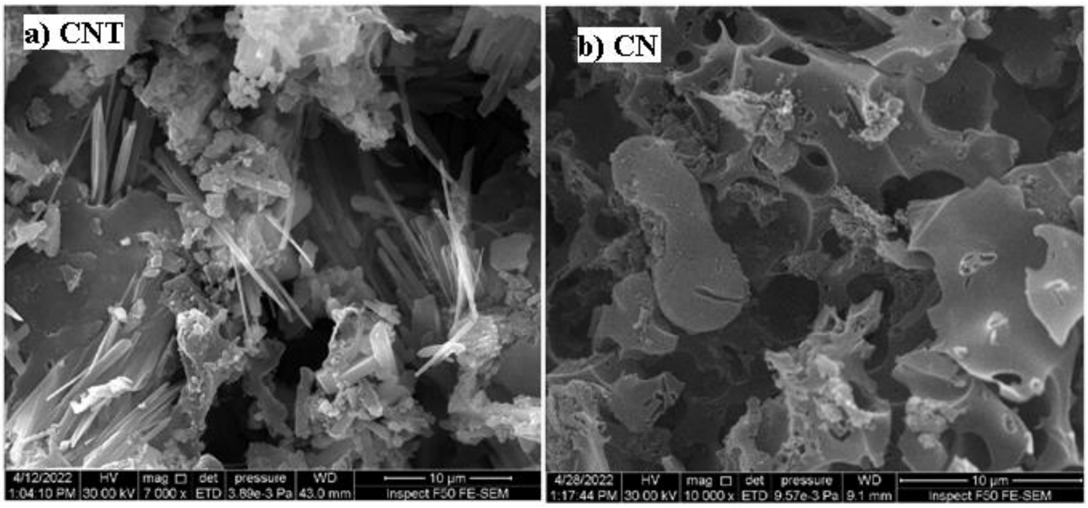

Figure 1: The images of a) carbon nanotube (CNT) and b) nano carbon (CN).

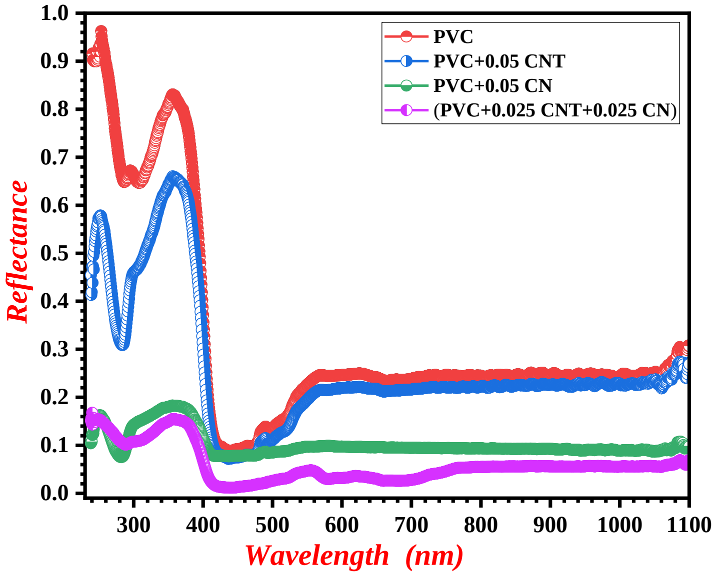

Figure 2: Reflectance variation with wavelength for the nanocomposite thin films **(**blank PVC, PVC-CNT, PVC-CN, and PVC-CNT-CN).

3. Results and Discussion

3.1. Reflectance of the nanocomposite thin films (blank PVC, PVC-CNT, PVC-CN, and PVC-CNT-CN)

The reflectance of the nanocomposite thin films (blank PVC, PVC-CNT, PVC-CN, and PVC-CNT-CN) can be shown in Figure 2. Figure 2 shows the variation of reflectance with wavelength for the nanocomposite thin films (blank PVC, PVC-CNT, PVC-CN, and PVC-CNT-CN), it can see the curves of reflectance initiated from a high value in the UV region and declines to a lower value in the visible region. Therefore, after the visible region ($400\geq\lambda\geq600$), all curves of reflectance are continued invariant when shifted to a higher wavelength. The best nanocomposite thin film is PVC-CNT-CN has a lower value of reflectance compared with other curves and blank PVC [14, 15].

3.2. Absorption coefficient of the nanocomposite thin films (blank PVC, PVC-CNT, PVC-CN, and PVC-CNT-CN)

The absorption coefficient (α) of nanocomposite thin films was studied between 250-1300 nm of the incident wavelength. The variation of absorption coefficient (α) with the wavelength of the nanocomposite thin films (blank PVC, PVC-CNT, PVC-CN, and PVC-CNT-CN) can be shown in Figure 3.

The absorbance coefficient (α) of the nanocomposite thin films (blank PVC, PVC-CNT, PVC-CN, and PVC-CNT-CN) is calculated from equation 1 [15-17]:

$$\alpha = 2.303 * \frac{A}{t} \ldots \qquad (1)$$

Where (α) absorbance coefficient (cm^{-1}), (A) absorbance value, (t) coating thickness (cm).

It is obvious from Figure 3 that the absorption coefficient (α) increases as a content of nanoparticles (CNT+CN) is founded in the PVC matrix, because these nanoparticles improves the matrix of PVC and drives to increase in the absorption after the absorption edge between the wavelength range ($500 \geq \lambda \geq 600$) of the thin films. Thereby, all the absorption coefficient curves have high absorption after doping PVC with (CNT+CN) [18].

3.3. Transmittance of the nanocomposite thin films (blank PVC, PVC-CNT, PVC-CN, and PVC-CNT-CN)

The transmittance of the nanocomposite thin films (blank PVC, PVC-CNT, PVC-CN, and PVC-CNT-CN) are demonstrated in Figure 4.

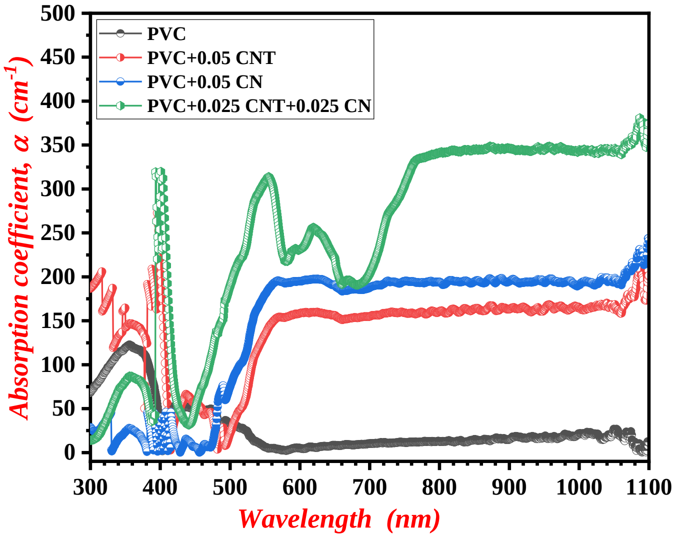

Figure 3: Absorbance coefficient variation with wavelength for the nanocomposite thin films **(**blank PVC, PVC-CNT, PVC-CN, and PVC-CNT-CN).

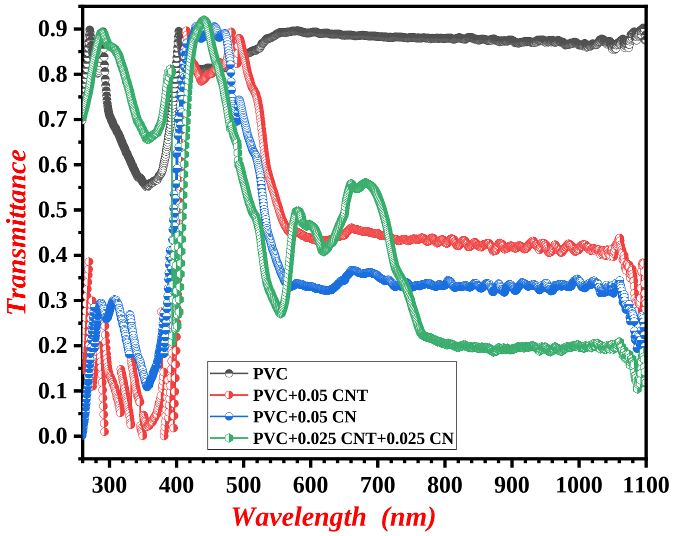

Figure 4: Transmittance variation with wavelength for the nanocomposite thin films **(**blank PVC, PVC-CNT, PVC-CN, and PVC-CNT-CN).

It can be seen from Figure 4 that the transmittance of the blank PVC is 90 %, but the other curves that doped with nanoparticles (CNT+CN) decreased to be lower value when is shifted to a higher wavelength. This due to existence of nanoparticles (CNT+CN) in the PVC matrix. Also, can see from Figure 4 the interference of nanoparticles inside the PVC decreased the transmittance and be about 20 % for the nanocomposite thin film PVC-CNT-CN, which is be the best thin film compared with other curves [19].

3.4. Refractive index of the nanocomposite thin films (blank PVC, PVC-CNT, PVC-CN, and PVC-CNT-CN)

The propagation of the wavelength inside the thin films is displayed by the refractive index, therefore, the refractive index depends on the reflectance. Then, it is computed from equation 2 [20]:

$$n = \left[\frac{1+R}{1-R}\right] + \sqrt{\frac{4R}{(1-R)^2} - k^2} \ldots \qquad (2)$$

Where (n) refractive index, (R) reflectance, and (k) extinction factor. The refractive index (n) is displayed in Figure 5 of the nanocomposite thin films (blank PVC, PVC-CNT, PVC-CN, and PVC-CNT-CN).

Figure 5 shows the refractive index of nanocomposite thin films (blank PVC, PVC-CNT, PVC-CN, and PVC-CNT-CN), it is obvious that the refractive index (n) increases to be maximum value in the UV region. Then decreases in the visible region and be continuous invariant along the wavelength shifted to higher values. The refractive index increases from value 1.5 to 2.5 at (λ=600 nm), the increasing in refractive index (n) for all the curves have nanoparticles of (CNT+CN) compared with blank PVC, this due to the density of (CNT+CN) nanoparticles packed in PVC structure [21].

3.5. Extinction factor of the nanocomposite thin films (blank PVC, PVC-CNT, PVC-CN, and PVC-CNT-CN)

The important factor that demonstrates the light loss during the absorption and scattering inside the thin films called by extinction coefficient (k). it is computed from equation 3 [22]:

$$k = \frac{\alpha\lambda}{4\pi} \ldots \qquad (3)$$

Where, (λ) wavelength (cm), (α) absorption coefficient (cm^{-1}).

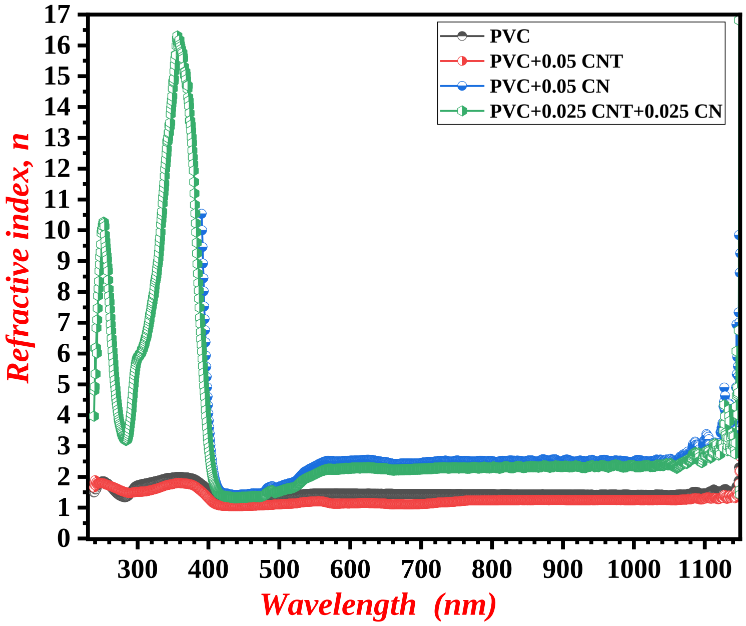

Figure 5: Refractive index variation with wavelength for the nanocomposite thin films (blank PVC, PVC-CNT, PVC-CN, and PVC-CNT-CN).

Therefore, it can be seen from Figure 6 the extinction factor (k) for the nanocomposite thin films (blank PVC, PVC-CNT, PVC-CN, and PVC-CNT-CN), inside these thin films, the CNT and CN were implanted within the PVC matrix to dope PVC and minimize losses of absorption and scattering inside nanocomposite thin films.

Also, from Figure 6 the extinction factor (k) for all curves of the nanocomposite thin films (PVC-CNT, PVC-CN, and PVC-CNT-CN) have low values of extinction factor (k), this is attributed to finding the nanoparticles inside the PVC matrix which is lead minimizing the loss in absorption and scattering [23, 24].

3.6. Dielectric constant (real and imaginary) of the nanocomposite thin films (blank PVC, PVC-CNT, PVC-CN, and PVC-CNT-CN)

The dielectric constant (ε) is correlated to the electronic framework of the nanocomposite thin films and denotes to the density of localized states in the gap, the dielectric constant for the real ε' and imaginary ε can be computed directly from the equation 4 [25]:

$$\left[(\varepsilon) = \varepsilon'(\boldsymbol{\omega}) + \boldsymbol{i}\varepsilon''(\boldsymbol{\omega})\right] \qquad (4)$$

The dielectric constant (ε) dependent on (n) and (k) parameters and can be computed equation 5 [25]:

$$\begin{bmatrix} \varepsilon' = n^2 - k^2 \\ \varepsilon'' = 2nk \end{bmatrix}\ldots \qquad (5)$$

Furthermore, both the real ε and imaginary ε are shown in Figures 7 and 8 of the nanocomposite thin films (PVC-CNT, PVC-CN, and PVC-CNT-CN). Figure 7 shows the real dielectric constant ε for the nanocomposite thin films (PVC-CNT, PVC-CN, and PVC-CNT-CN) to exhibit its values various with the wavelength.

Figure 7 shows the variation of real dielectric constant (ε) with the wavelength for the nanocomposite thin films (PVC-CNT, PVC-CN, and PVC-CNT-CN), where the real dielectric constant for these thin films increases when added the (CNT+CN) to the PVC matrix, this increase lead to form many local states in the gap. Therefore, the doping changes the electronic structure of PVC [26]. Similarly, Figure 8 shows the variation of imaginary dielectric constant with the wavelength for the nanocomposite thin films (PVC-CNT, PVC-CN, and PVC-CNT-CN).

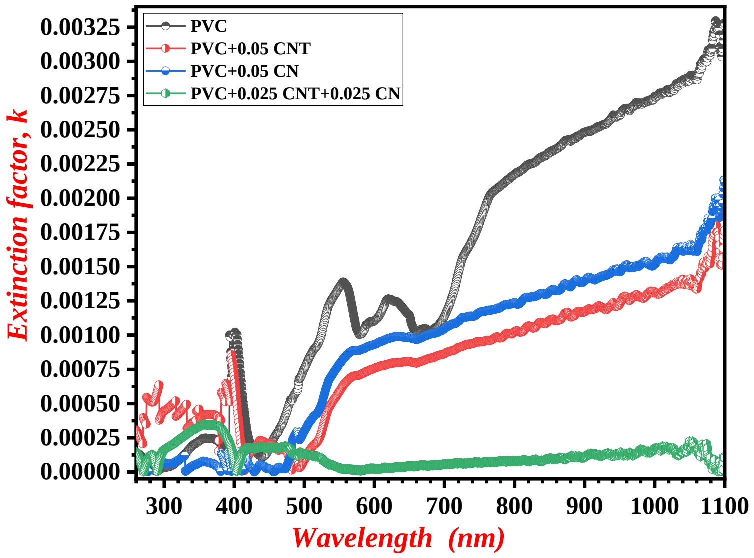

Figure 6: Extinction factor variation with wavelength for the nanocomposite thin films **(**blank PVC, PVC-CNT, PVC-CN, and PVC-CNT-CN).

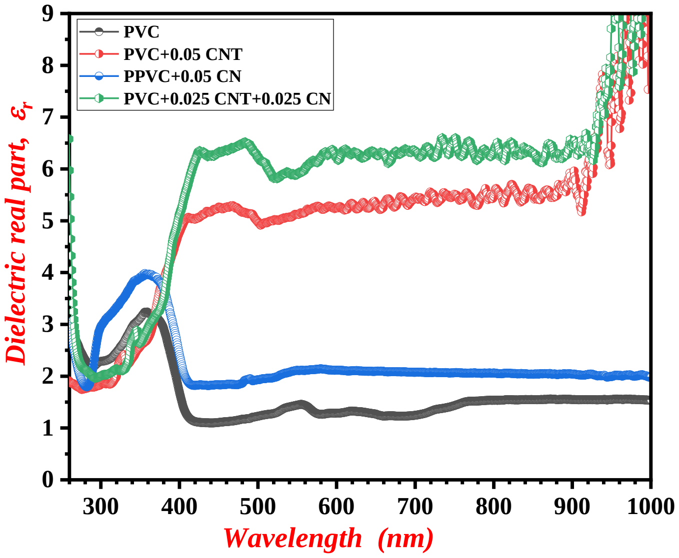

Figure 7: Real dielectric constant variation with wavelength for the nanocomposite thin films **(**blank PVC, PVC-CNT, PVC-CN, and PVC-CNT-CN).

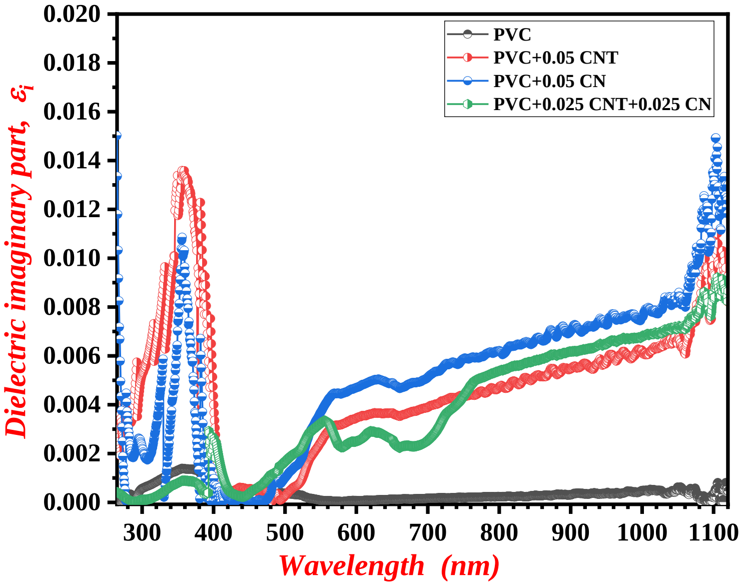

Figure 8: Imaginary dielectric constant variation with wavelength for the nanocomposite thin films **(**blank PVC, PVC-CNT, PVC-CN, and PVC-CNT-CN).

It can be seen from Figure 8 the imaginary dielectric constant for the nanocomposite thin films (PVC-CNT, PVC-CN, and PVC-CNT-CN), whereas, its high values in the UV region is attributed to the effect of polarization that decrease when the wavelength shifted to higher values. Thereby, the addition of (CNT+CN) lead to increase the imaginary dielectric constant due to change in the electronic structure in PVC matrix [26].

3.7. Optical conductivity of the nanocomposite thin films (blank PVC, PVC-CNT, PVC-CN, and PVC-CNT-CN)

The photon energy when incident on the surface of the thin films will excited the charge carriers and diffused between the structure. This diffusion will caused transfer these charge carriers from valence band to the conduction band. Then, the optical conductivity is computed by the equation 6 [27]:

$$\sigma = \frac{\alpha n c}{4\pi} \ldots \qquad (6)$$

Where (σ) optical conductivity (S^{-1}), (*n*) refractive index, (c) light speed ($3x10^{10}$ cm/s), and (*α*) absorbance coefficient (cm^{-1}).

Figure 9 shows the optical conductivity various with the wavelength for the nanocomposite thin films (PVC-CNT, PVC-CN, and PVC-CNT-CN). In overall, it is shown that the optical conductivity increasing when the wavelength increases. the influence of the wavelength is clear to excite the electrons and lead to increase the optical conductivity as shown in Figure 9. Therefore, the addition of (CNT+CN) to the PVC matrix increase optical conductivity, which lead to increase charge carriers and make easy transition of electrons through the bands [28].

3.8. Optical energy gap of the nanocomposite thin films (blank PVC, PVC-CNT, PVC-CN, and PVC-CNT-CN)

The gap between the valence band and conduction band is called the energy gap and it has been studied via Tauc's relation, equation 7 [29]:

$$\alpha h\nu = B\ (h\nu - E_g)^n \ldots \qquad (7)$$

Where (*B*) constant, (*Eg*) energy gap, and (n) power to the transition type (n=2 for direct transition and n=0.5 for indirect transition, respectively) [30, 31].

Thereby, to get the values of energy gap by taking the square of ($\alpha h\upsilon$) with ($h\upsilon$) as shown in Figures 10 and 11 for the nanocomposite thin films (PVC-CNT, PVC-CN, and PVC-CNT-CN). Figure 10 shows the direct energy gap for the nanocomposite thin films (PVC-CNT, PVC-CN, and PVC-CNT-CN), it can be obtained by intercept the linear line of extrapolating to x-axis when the value of ($\alpha h\upsilon$) zero (y=0).

It can be shown from Figure 10 that the direct energy gap of blank PVC thin film is 4.6 eV, and for the nanocomposite thin film (PVC-CNT) is become 3.0 eV, where decreased after added carbon nanotube (CNT). The direct energy gap of nanocomposite thin film (PVC-CN) is become 3.4 eV, after addition carbon nano (CN). And then, for the nanocomposite thin film (PVC-CNT-CN) is become 2.9 eV, where after addition the hybrid nanomaterials (CNT+CN) to the PVC matrix, there is a decreasing in the energy gap to a lower value. Therefore, when added the nanomaterials to the PVC matrix are changed the structure and grant it the conductivity. All values of energy gap for the nanocomposite thin films (PVC-CNT, PVC-CN, and PVC-CNT-CN) are listed in table 1 [32]. Likewise, Figure 11) shows the indirect energy gap for the nanocomposite thin films (PVC-CNT, PVC-CN, and PVC-CNT-CN) to obtain these values.

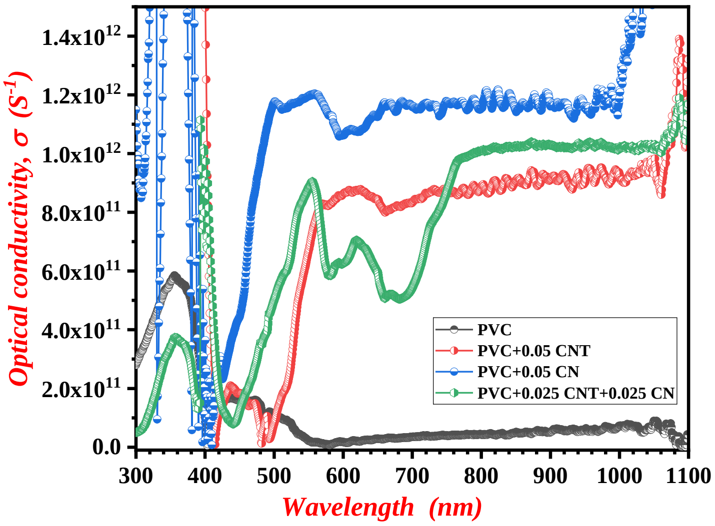

Figure 9: Optical conductivity variation with wavelength for the nanocomposite thin films **(**blank PVC, PVC-CNT, PVC-CN, and PVC-CNT-CN).

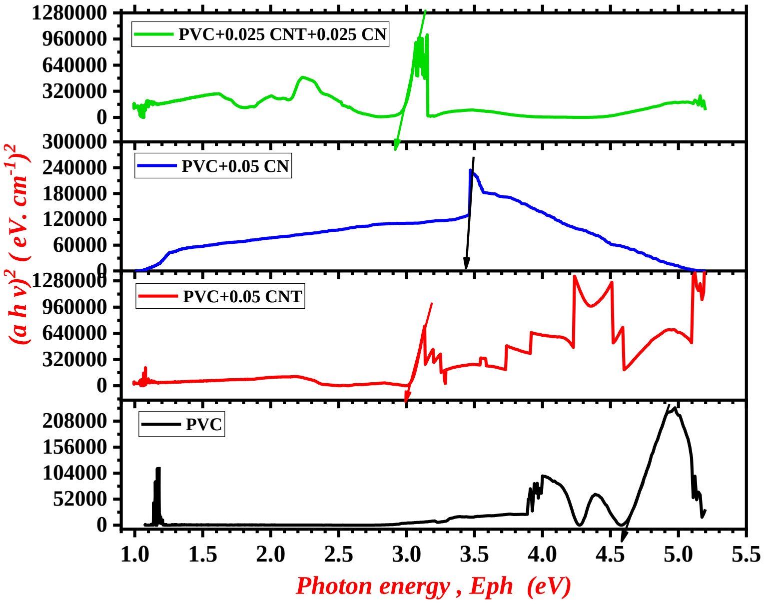

Figure 10: Energy gap variation with wavelength for the nanocomposite thin films (blank PVC, PVC-CNT, PVC-CN, and PVC-CNT-CN).

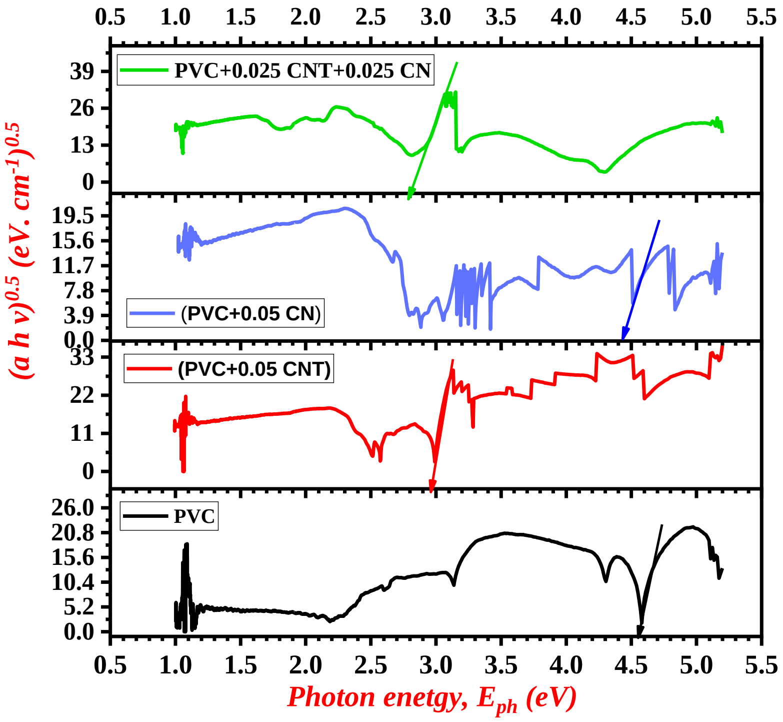

Figure 11: Energy gap variation with wavelength for the nanocomposite thin films (blank PVC, PVC-CNT, PVC-CN, and PVC-CNT-CN).

It can show from Figure 11 that the indirect energy gap of blank PVC thin film is 4.55 eV, and for the nanocomposite thin film (PVC-CNT) is become 2.95 eV, where decreased after added carbon nanotube (CNT). The indirect energy gap of nanocomposite thin film (PVC-CN) is become 4.4 eV, after addition carbon nano (CN), this value is become higher from direct band gap value due to irregular mixing in this region. And then, for the nanocomposite thin film (PVC-CNT-CN) is become 2.8 eV, where after addition the hybrid nanomaterials (CNT+CN) to the PVC matrix, there is a decreasing in the energy gap to a lower value. Therefore, when added the nanomaterials to the PVC matrix are changed the structure and grant it the conductivity. All values of energy gap for the nanocomposite thin films (PVC-CNT, PVC-CN, and PVC-CNT-CN) are listed in Table 1 [32].

3.9. Urbach energy of the nanocomposite thin films (blank PVC, PVC-CNT, PVC-CN, and PVC-CNT-CN)

The urbach energy (ε_u) is happened due to absorb the photon energy, this absorption caused a formation of localized states in the gap due to the electrons movement which lead increase the degree of disorder in the gap of the nanocomposite. Then, equations 8 is used to compute urbach energy [30, 32]:

$$\alpha = \alpha_o exp\frac{hv}{E_u}\ldots \qquad (8)$$

By modified equation 8, the get (Eq. 9):

$$ln\alpha = ln\alpha_o + \frac{hv}{E_u} \qquad (9)$$

Where, (α_o) constant.

Figure 12 shows the urbach energy variation with photon energy for the nanocomposite thin films (PVC-CNT, PVC-CN, and PVC-CNT-CN). From Figure 12 shows the urbach energy is plotted against photon energy, and gets the reciprocal of the slope for the curves that formed in Figure 11 to give the value of urbach energy. It can see from Figure 12 that urbach energy is increased from 2.240-8.190 eV for the nanocomposite thin films (PVC-CNT, PVC-CN, and PVC-CNT-CN), this obvious that urbach energy increased when added the nanomaterials (CNT+CN) to the PVC matrix. Also, the degree of disorder is increased when the value of urbach energy increases [33, 34]. The values of urbach energy are listed in Table 1.

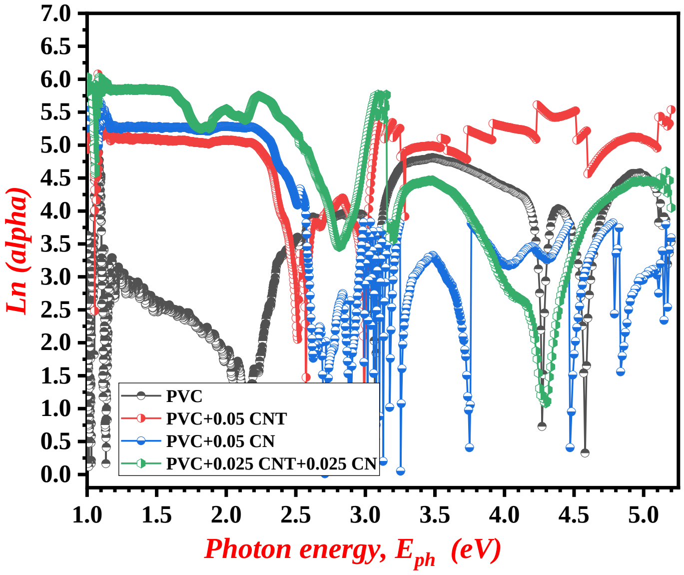

Figure 12: Urbach energy variation with wavelength for the nanocomposite thin films **(**blank PVC, PVC-CNT, PVC-CN, and PVC-CNT-CN).

Table 1: shows the values of direct energy gap, indirect energy gap, and urbach energy.

No.	Parameters	Blank PVC (eV)	PVC+0.05CNT (eV)	PVC+0.05CNT (eV)	PVC+0.025CNT +0.025CN (eV)
1	Direct transition of (Eg) (eV)	4.6	3.0	3.4	2.9
2	Indirect transition of (Eg) (eV)	4.55	2.95	4.4	2.8
3	Urbach energy (Eu) (eV)	2.240	8.190	1.126	1.386
4	(α_o) constant (cm^{-1})	7.925	177.151	634.603	853.035

4. Microscope images of the nanocomposite thin films (blank PVC, PVC-CNT, PVC-CN, and PVC-CNT-CN)

The microscope images analysis was utilized to assign the form of thin film morphology and distribution of nanomaterials (CNT+CN) in the PVC matrix. Figure 13 exhibits the microscope images for the blank PVC and the nanocomposite thin films (PVC-CNT, PVC-CN, and PVC-CNT-CN). It was noticed that the (CNT+CN) nanomaterials have collected as a spherical shape. Where, Figure 13a shows the blank PVC image is clear. Figure 13b shows the nanocomposite thin film of PVC+CNT and the carbon nanotube (CNT) takes a form agglomerates of spherical shape in the thin film. Figure 13c shows the nanocomposite thin film of PVC+CN and the nano carbon takes a form agglomerates as a spherical shape also, but is smaller than the spherical shape in PVC+CN thin film. Figure 13d shows a homogeneous mixing of carbon nanotube with nano carbon distributed in PVC matrix [35].

5. AFM test of the nanocomposite thin films (blank PVC, PVC-CNT, PVC-CN, and PVC-CNT-CN)

Figure 14 a, b, c, and d shows the topography of the surface in 3D and 2D for the blank PVC and the nanocomposite thin films (PVC-CNT, PVC-CN, and PVC-CNT-CN) by the AFM device.

The blank PVC thin film surface shows in Figure 14a is fine and has small roughness 1.07 nm. Figure 14b shows the nanocomposite thin film of PVC+CNT has a high roughness; its value 3.09 nm is greater than the blank PVC thin film. Figure 14c shows the nanocomposite thin film of PVC+CN has a higher roughness; its value 3.30 nm is greater than from the blank PVC thin film and the nanocomposite thin film of PVC+CNT. While, Figure 14d shows the nanocomposite thin film of PVC+CNT+CN has a lower value of roughness is 1.22 and greater than the blank PVC thin film [36].

Table 2: AFM test for blank PVC, PVC+CNT, PVC+CN, and PVC+CNT+CN nanocomposites thin films.

No.	Composite	Number of figures	Roughness average (nm)	Root mean square of roughness (nm)
1	Blank PVC	14a	1.07	1.49
2	PVC+CNT	14b	3.09	4.08
3	PVC+CN	14c	3.30	4.57
4	PVC+CNT+CN	14d	1.22	1.79

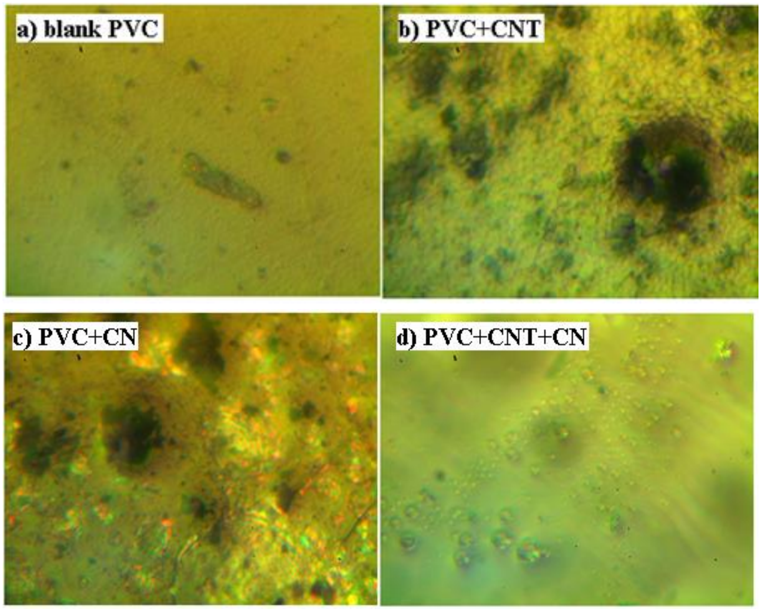

Figure 13: Images for the nanocomposite thin films a) blank PVC, b) PVC-CNT, c) PVC-CN, and d) PVC-CNT-CN).

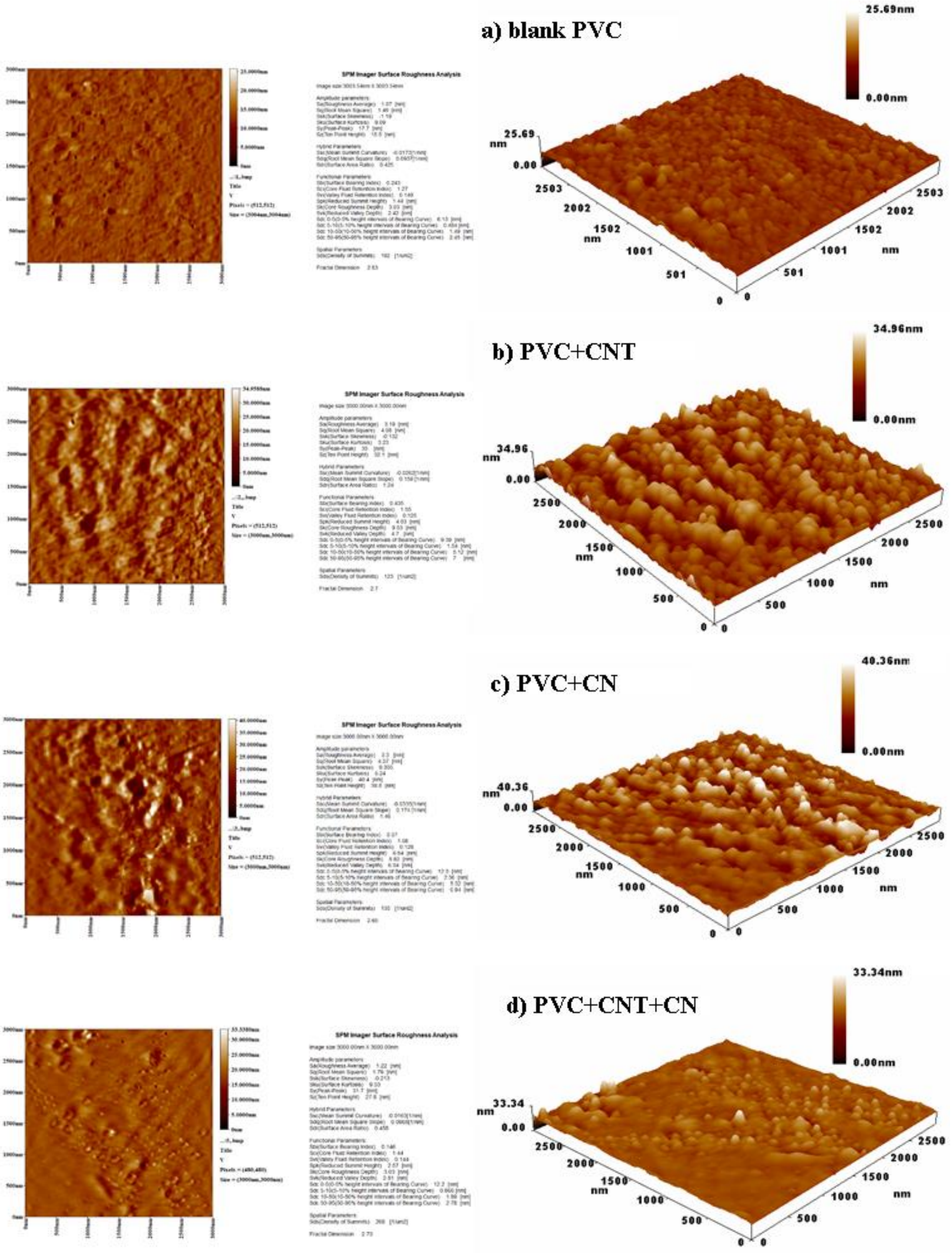

Figure 14: 3D and 2D pictures display the average roughness and root mean square for: a) blank PVC, b) PVC-CNT, and c) PVC-CN, and d) PVC+CNT+CN.

4. Conclusion

The PVC nanocomposite thin films have been made by casting technology, they containing carbon nanotube (CNT) and nano carbon (CN) in PVC matrix to change their structure. The impact was done in the structure of PVC nanocomposite thin films (PVC-CNT, PVC-CN, and PVC-CNT-CN) by adding nanomaterials (CNT+CN). The optical properties were studied for the blank PVC and nanocomposite thin films by using computerized diffused reflectance of UV-Visible. The absorption coefficient, reflectance, extinction factor, optical density, and refractive index of optical properties have decreased, and the reflectance with transmittance were decreased of the nanocomposite thin films (PVC-CNT, PVC-CN, and PVC-CNT-CN) compared with blank after dispersion of (CNT+CN) in

PVC matrix. The conductivity and dielectric constant were increased of nanocomposite thin films after adding nanomaterials. The diminish direct energy gap from 4.6 eV for the blank PVC to 2.9 eV of nanocomposite thin film, and there is a diminish in an indirect energy gap from 4.55-2.8 eV. The urbach energy was increased of nanocomposite thin films (PVC-CNT, PVC-CN, and PVC-CNT-CN) after adding the nanomaterials (CNT+CN) to the PVC matrix from 2.240 eV to 8.190. The configuration of the carbon nanotube (CNT) and nano carbon (CN) was appeared by SEM images, and the AFM images shows a fine surface of the of nanocomposite thin films (PVC-CNT, PVC-CN, and PVC-CNT-CN). The surface roughness has been increased from 1.07 nm for the blank PVC to 3.30 nm of nanocomposite thin films (PVC-CNT, PVC-CN, and PVC-CNT-CN) after adding the nanomaterials to the PVC matrix. The applications were used in many applications like optical clarity, high mechanical strength, thermal gas barrier of the nanocomposite thin films (PVC-CNT, PVC-CN, and PVC-CNT-CN).

Acknowledgment

This work was supported by Polymer Research Center/ College of Science of Al-Mustansiriyah University and university of Samarra.

5. References

1. S. N. Krivoshapko, The perspectives of application of thin-walled plastic and composite polymer shells in civil and industrial architecture, *J. Reinf. Plast. Comp*., 37(2018), 217-229.
2. F. Cogswell, The processing science of thermoplastic structural composites, *Int Polym Process.*, 1(1987), 157-165.
3. Y. Z. Bao, H. Zhi-Ming, L. Shen-Xing, W. Zhi-Xue, Thermal stability, smoke emission and mechanical properties of poly (vinyl chloride)/hydrotalcite nanocomposites, *Polym Degrad Stabil.*, 93 (2008), 448-455.
4. K. Kalaitzidou, H. Fukushima, L.T. Drzal, Mechanical properties and morphological characterization of exfoliated graphite–polypropylene nanocomposites, *Compos Part A: Appl Sci Manuf.*, 38(2007), 1675-1682.
5. J. Liang, Y. Huang, L. Zhang, Y. Wang, Y. Ma, T. Guo, Y. Chen, Molecular-level dispersion of graphene into poly (vinyl alcohol) and effective reinforcement of their nanocomposites, *Adv. Funct. Mater.*, 19(2009), 1-6.
6. T. Ramanathan, A. A. Abdala, S. Stankovich, D. A. Dikin, M. Herrera-Alonso, R. D. Piner, D. H. Adamson, H. C. Schniepp, X. Chen, R. S. Ruoff, S. T. Nguyen, I. A. Aksay, R.K. Prud’homme, L. C. Brinson, Functionalized graphene sheets for polymer nanocomposites, *Nature Nanotechnol*., 3(2008), 327-331.
7. X. Zhao, Q. Zhang, D. Chen, P. Lu, Enhanced mechanical properties of graphene-based poly (vinyl alcohol) composites, *Macromolecules.*, 43(2010), 2357-2363.
8. S. Kumar, M. Nehra, D. Kedia, N. Dilbaghi, K. Tankeshwar, K.H. Kim, Carbon nanotubes: a potential material for energy conversion and storage, *Prog. Energy Combust. Sci.*, 64(2018), 219-53.
9. L. Sun, X. Wang, Y. Wang, Q. Zhang, Roles of carbon nanotubes in novel energy storage devices Carbon, N. Y., *book*, 122 (2017), 462-74.
10. A. F. A. Naim, H. Alfannakh, S. Arafat, S. S. Ibrahim, Characterization of PVC/MWCNT snanocomposite: solvent blend, *Sci. Eng. Compos. Mater.*, 27(2020), 55-64.
11. G. Broza., K. Piszczek, K. Schulte, T. Sterzynski, Nanocomposites of poly(vinyl chloride) with carbon nanotubes (CNT), *Composites Sci. Technol.*, 67(2007), 890-894.
12. E. Abdel‑Fattah, A.I. Alharthi, T. Fahmy, Spectroscopic, optical and thermal characterization of polyvinyl chloride‑based plasma‑functionalized MWCNTs composite thin films, *Appl. Phys. A*, 475(2019), 1-8.
13. P. Molla-Abbasi, Effect of nano-size nodular structure induced by CNT promoted phase separation on the fabrication of superhydrophobic polyvinyl chloride films, *Polym. Adv. Technol.*, 32(2021), 391-401.
14. G. He, X. Chen, Z. Sun, Interface engineering and chemistry of Hf-based high-k dielectrics on III–V substrates, *Surf. Sci. Rep.*, 68(2013), 68-107.
15. R. N. Abed, A.R.N. Abed, F.A. Khamas, M. Abdallh, E. Yousif, High performance thermal coating comprising (CuO:NiO) nanocomposite/C spectrally selective to absorb solar energy, *Prog. Color Colorants Coat.*, 13 (2020), 275-284.
16. W. Al-Taa’y, M.A. Nabi, R. Yusop, M. E. Yousif, B. M. Abdullah, J. Salimon, N. Salih, S.I. Zubairi, Effect of nano ZnO on the optical properties of poly(vinyl chloride) films, *Int. J. Polym. Sci.*, 2014 (2014), 1-6.
17. W.A. Al-Taa'y, A.A. Ameer, W. H. Al-Dahhan, M. Abddallh, E. Yousif, Optical constants of poly(vinyl chloride) doped by nano ZnO, *J. Chem. Pharm. Res.*, 7(2015), 536-541.

18. A. Hassen, S. El-Sayed, M. Mm, A. El Sayed, Preparation, dielectric and optical properties of Cr_2O_3/ PVC nanocomposite films, *J. Adv. Phys.*, 4(2018), 571-584.
19. R. Khordad, Absorbance of iron nanoparticles dispersed in the ethylene glycol and n-propanol, *Armen. J. Phys.*, 9(2016), 211-219.
20. A.S.Hassanien, A.A.Akl, Optical characteristics of iron oxide thin films prepared by spray pyrolysis technique at different substrate temperatures, *Appl. Phys. A*, 752(2018), 1-16.
21. A. Yang, H. Fan, Y. Xuexi, J. Chen, Z. Li, Effects of depositing temperatures on structure and optical properties of TiO_2 film deposited by ion beam assisted electron beam evaporation, *Appl. Surf. Sci.*, 254(2008), 2685-2689.
22. Q. M. Al-Bataineh, A. M. Alsaad, A. A. Ahmad, A. Al-Sawalmih, Structural, electronic and optical characterization of ZnO thin film-seeded platforms for ZnO nanostructures: Sol–Gel method versus Ab initio calculations, *J. Electron. Mater.*, 48(2019), 5028-5038.
23. M. D. Stamate, Dielectric properties of TiO_2 thin films deposited by a DC magnetron sputtering system, *Thin Solid Films*, 372(2000), 246-249.
24. D. Souri, Z. E. Tahan, A new method for the determination of optical band gap and the nature of optical transitions in semiconductors, *Int. J. Appl. Phys. B*, 119(2015), 273-279.
25. R. N. Abed, M. Abdallh, A. A. Rashad, A. Hadawey, E. Yousif, New coating synthesis comprising CuO:NiO/C to obtain highly selective surface for enhancing solar energy absorption, *J. Polym. Bull.*, 78(2021), 433-455.
26. R. N. Abed, M. Kadhom, D. S. Ahmed, A. Hadawey, E. Yousif, Enhancing optical properties of modified PVC and Cr_2O_3 nanocomposite, *Trans. Electr. Electron. Mater.*, 22(2021), 317-327.
27. F. Urbach, The long wavelength edge of photographic sensitivity and of the electronic absorption of solids, *Phys. Rev.*, 92(1953), 1324.
28. R. N. Abed, E. Yousif, A. R. N. Abed, A. A. Rashad, Synthesis thin films of poly(vinyl chloride) doped by aromatic organosilicon to absorb the incident light, *Silicon*, 223(2022), 33-45.
29. O. G. Abdullah, D. R. Saber, Optical absorption of poly-vinyl alcohol films doped with nickel chloride, *Appl. Mech. Mater.*, 110-116(2012), 177-182.
30. R. N. Abed, A. R. N. Abed, E. Yousif, Carbon surfaces doped with (Co_3O_4-Cr_2O_3) nanocomposite for high-temperature photo thermal solar energy conversion via spectrally selective surfaces, *Prog. Color Colorants Coat.*, 14(2021), 301-315.
31. A. S.Hassanien, A. A. Akl, Effect of Se addition on optical and electrical properties of chalcogenide CdSSe thin films, *Superlattice Microst.*, 89(2016), 153-169.
32. Z. M. Al-Azzawi, M. Al-Baidhani, A. R. N. Abed, R. N. Abed, Influence of nano silicon carbide (SiC) embedded in poly(vinyl alcohol) (PVA) lattice on the optical properties, *Silicon*, 14(2021), 5719-5732.
33. A. M. Alsaad, A. A. Ahmad, I. A. Qattan, Q. M. Al-Bataineh, Z. Albataineh, Structural, optoelectrical, linear, and nonlinear optical characterizations of dip-synthesized undoped ZnO and group III elements (B, Al, Ga, and In)-doped ZnO thin films, *Crystals*, 252(2020), 1-17.
34. R. N. Abed, A. R. N. Abed, Characterization effect of copper oxide and cobalt oxide nanocomposite on poly(vinyl chloride) doping process for solar energy applications, *Prog. Color Colorants Coat.*, 15(2022), 235-241.
35. A. P. Safronov, A. Shankar, E. A. Mikhnevich, I. V. Beketov, Influence of the particle size on the properties of polyacrylamide ferrogels with embedded micron-sized and nano-sized metallic iron particles, *J. Magn. Magn. Mater.*, 459(2018), 125-130.
36. N. Algethami, A. Rajeh, H. M. Ragab, A. E. Tarabiah, F. Gami, Characterization, optical, and electrical properties of chitosan/polyacrylamide blend doped silver nanoparticles, *J. Mater. Sci.: Mater. Electron.*, 33(2022), 10645-10656.

How to cite this article:
A. M. Abdullah, L. H. Alwan, A. A. Ahmed, R. N. Abed, Optical and Physical Properties for The Nanocomposite Poly(vinyl chloride) with Affected of Carbon Nanotube and Nano Carbon. Prog. Color Colorants Coat., 16 (2023), 331-345.

PROGRESS IN COLOR, COLORANTS AND COATINGS

available online @ www.pccc.icrc.ac.ir

Progress in Color Colorants Coating 16 (2023), 347-359

Ministry of Science, Research and Technology
Institute for Color Science & Technology

Investigation of the Corrosion Inhibition Properties of 4-Cyclohexyl-3-Thiosemicarbazide on Mild Steel in 1 M HCl Solution

A. Mohammed[1], A. Y. I. Rubaye[2], W. K. Al-Azzawi[3], A. Alamiery[4]*

[1] Department of Electromechanical Engineering, University of Technology-Iraq, P.O. Box: 10001, Baghdad, Iraq

[2] Chemical and Petrochemical Techniques Engineering Department, Basra Engineering Technical College, Southren Technical University, P.O. Box: 102, Basra, Iraq

[3] Department of Medical Instruments Engineering Techniques, Al-Farahidi University, P.O. Box:10001, Baghdad, Iraq

[4] Department of Chemical and Process Engineering, Faculty of Engineering and Build Environment, Universiti Kebangsaan Malaysia, P.O. Box: 43600, Bangi, Selangor, Malaysia.

ARTICLE INFO

Article history:
Received: 08 Apr 2023
Final Revised: 10 May 2023
Accepted: 14 May 2023
Available online: 27 Aug 2023

Keywords:
4-Cyclohexyl-3-thiosemicarbazide
Corrosion inhibitor
DFT
LUMO.

ABSTRACT

The study investigated the effectiveness of 4-cyclohexyl-3-thiosemicarbazide (4C3T) as a corrosion inhibitor for mild steel in 1 M HCl solution using the weight loss method. Various concentrations of 4C3T, temperatures, and immersion times were used to determine the inhibitory efficiency. The results showed that increasing the concentration of 4C3T resulted in higher inhibition efficiency while increasing the temperature decreased it. The optimal conditions were found to be a concentration of 0.5 mM at 303 K, which resulted in a 95 % inhibition efficiency. The mechanism of inhibition involved the adsorption of 4C3T onto the mild steel surface, which prevented corrosion. The adsorption followed the Langmuir adsorption isotherm, where physical and chemical adsorption coexisted. Quantum chemical calculations were used to support the findings. Overall, the study highlights the potential of 4C3T as a corrosion inhibitor for mild steel in HCl solution and offers insights into the underlying inhibitory process. Prog. Color Colorants Coat. 16 (2023), 347-359© Institute for Color Science and Technology.

1. Introduction

Corrosion is a major problem in various industries and can result in significant economic costs due to damage and loss of productivity. The direct and indirect costs associated with corrosion can be substantial, and therefore, preventing corrosion is of utmost importance [1]. Corrosion protection of metallic structures is a crucial concern in many industries due to the significant financial and safety losses from corrosion [2, 3]. Mild steel is widely used in various applications due to its low cost and excellent physical and mechanical properties [4, 5]. However, mild steel is highly susceptible to corrosion, particularly in acidic environments [6]. Therefore, it is necessary to discover effective methods to protect mild steel from corrosion [7]. Several methods are used to prevent corrosion, including protective coatings, cathodic protection, and corrosion inhibitors. Corrosion inhibitors are chemicals that can be added to a corrosive environment to reduce or prevent a material's corrosion. Corrosion inhibitors work by adsorbing onto the metal surface, forming a protective barrier, and reducing the corrosion rate [8].

---

*Corresponding author: * dr.ahmed1975@ukm.edu.my
dr.ahmed1975@gmail.com

Doi: 10.30509/pccc.2023.167126.1212

Corrosion inhibitors are widely accepted for preventing corrosion in various industries, including oil and gas, chemical processing, and transportation [9]. Corrosion inhibitors offer several advantages over other methods, such as ease of application, cost-effectiveness, and compatibility with other corrosion prevention methods [10]. One approach to reducing corrosion in acidic solutions is using organic compounds as corrosion inhibitors. Heterocyclic compounds containing N, S, and O-atoms, π-bonds, and aromatic systems have been effective inhibitors by adsorbing onto the mild steel surface and reducing corrosion [11-14]. The corrosion inhibitor 4C3T has been chosen for this study due to its highly functionalized structure, which includes -NH, NH_2, and C=S functional groups and three N and one S atoms. These features allow easy attachment to the mild steel surface and effective corrosion reduction [15, 16].

Additionally, 4C3T can be synthesized using green chemistry principles through multicomponent one-pot reactions with good yields. The corrosion inhibition efficiency (IE) of 4C3T has been investigated using density functional theory (DFT). This cost-effective and time-saving method provides detailed information about the mechanism of corrosion inhibition. Molecular properties such as EHOMO, ELUMO, ΔE, GS, GH, χ, and ΔN have been estimated using DFT, which helps simulate the experimental results obtained. This study explores the use of thiosemicarbazide derivatives as corrosion inhibitors in acidic media, focusing on the inhibitive performance of 4-cyclohexyl-3-thiosemicarbazide (4C3T) on mild steel corrosion in 1 M HCl, using weight loss techniques. The impact of varying immersion times and acidic inhibitor solutions was examined, and various thermodynamic parameters were determined. The experimental results were compared to theoretical data obtained using density functional theory (DFT) to understand the effective coordination mechanism between the inhibitor and the mild steel surface. The chemical structure of the tested inhibitor is demonstrated in Figure 1.

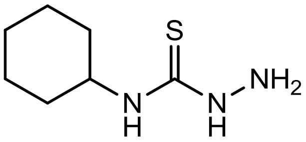

Figure 1: Chemical structure of 4C3T.

2. Experimental

2.1. Mild steel samples

The mild steel samples used in this study were obtained from a metal samples company, and their dimensions were 4.0×2.5×0.1 cm. Gravimetric measurements were carried out using samples with dimensions of 1.0 ×1.0 ×0.1 cm. These samples contained C (0.21), S (0.05), Mn (0.05), Si (0.38), P (0.09), Al (0.01), and Fe (the remainder) in weight percent. The samples were cleaned following conventional G1-03/ASTM [17]. Prior to testing, the mild steel samples were pre-treated by grinding with emery paper, washing with double-distilled water, degreasing with ethanol, and drying at room temperature to remove any surface impurities.

2.2. HCl solution

To create the corrosive environment, 1 M HCl was used, diluted from a 37 % analytical hydrochloric acid obtained from Merck-Malaysia using deionized water. The inhibitor 4C3T was added to the solution at concentrations of 0.1, 0.2, 0.3, 0.4, and 0.5 mM.

2.3. Weight loss analysis

Gravimetric measurements were performed to determine the corrosion inhibition properties of 4C3T on mild steel. The experiments involved immersing the mild steel samples in 1 M HCl solution with various concentrations of the inhibitor for different exposure times (1, 5, 10, 24, and 48 hours) at 303 K. After removal from the solution, the samples were cleaned with deionized water and acetone, dried, and weighed. The corrosion rate was then calculated by averaging the weight loss of three test specimens using equation 1 [18]. Tests were conducted using various concentrations of 4C3T for a 5-hour exposure period to evaluate the impact of temperature.

$$C_R(g.m^{-2}.h^{-1})=\frac{\Delta w}{st} \quad (1)$$

The weight loss of the structural steel was determined by measuring Δw in grams. The area of the specimen was denoted as s in units of square meters, while the immersion time was recorded in hours as t. equations 2 and 3:

$$\theta=\frac{IE(\%)}{100} \quad (2)$$

$$IE(\%)=\frac{C_{R(0)}-C_{R(i)}}{C_{R(0)}} \quad (3)$$

Where $C_{R(0)}$ is the corrosion rate in an untreated environment, $C_{R(i)}$ is the corrosion rate in a treated.

2.4. DFT

The Gaussian 09 software [19] was used for quantum chemical calculations. Optimizing the inhibitor structure in the gaseous phase was conducted using the B3LYP method and the "6-31G^{++}" (d,p) basis set. Koopmans theory [20] was applied to determine the ionization potential (I) and electron affinity (A), which are related to E_{HOMO} and E_{LUMO}, respectively. Equations 4 and 5 were utilized for this purpose.

$$I=-E_{HOMO} \tag{4}$$

$$A=-E_{LOMO} \tag{5}$$

To evaluate the electronegativity (χ), softness (σ), and hardness (η), using the equations 6-8:

$$\chi=\frac{I+A}{2} \tag{6}$$

$$\eta=\frac{I-A}{2} \tag{7}$$

$$\sigma=\eta^{-1} \tag{8}$$

To determine the transported electrons number (ΔN), [21] used equation 9:

$$\Delta N=\frac{\chi_{Fe}-\chi_{inh}}{2(\eta_{Fe}+\eta_{inh})} \tag{9}$$

The electronegativity and hardness values for iron were equal to 7 eV and zero eV, respectively; hence these results lead to equation 10:

$$\Delta N=\frac{7-\chi_{inh}}{2(\eta_{inh})} \tag{10}$$

3. Results and Discussion

3.1. Weight loss measurements

The weight loss method, which was used to determine the corrosion rates and inhibition efficiencies of the mild steel coupons, has some limitations that could affect the results' accuracy. One major limitation of the weight loss method is that it is prone to errors and uncertainties due to the difficulty of accurately measuring the weight of the corroded samples. Even slight variations in the measurement process, such as the duration of washing and drying, could lead to significant errors in the results. Additionally, the weight loss method does not provide information on the nature and morphology of the corrosion products, which can be important in understanding the underlying mechanisms of corrosion inhibition. Furthermore, the weight loss method assumes that the corrosion rate is constant over time, which may not always be true. Corrosion rates may change over time due to variations in the concentration of the corrosive solution or the inhibitor and changes in temperature and other environmental factors, which could result in inaccurate corrosion rate measurements and affect the calculation of inhibition efficiencies.

To mitigate these limitations, it is important to carefully control experimental conditions and measure the weight of the samples with high precision to minimize errors.

3.1.1. Effect of concentration

Figure 2 depicts the outcomes of weight loss tests on mild steel subjected to untreated and treated 1 M HCl solutions. The impact of varying concentrations of 4C3T on the corrosion rate was analyzed. Since HCl is a potent acid, the untreated solution resulted in rapid corrosion. However, an increase in the concentration of 4C3T led to a notable decline in the corrosion rate. Thus, 4C3T acts as an effective protector of mild steel against the harmful impact of HCl. The highest inhibition efficacy was observed at 0.5 mM, with 95 % for 4C3T. 4C3T contains a large molecular structure with hetero-elements such as sulphur and nitrogen atoms that help them adhere to the mild steel surface and create a protective coating. As the concentration of 4C3T increased to 0.5 mM, their effectiveness as corrosion inhibitors also increased. However, at concentrations approaching 1.0 mM, the inhibition efficacy remained nearly constant due to 4C3T particle adsorption on the metal substrate. Additionally, the varied functional groups in 4C3T enhance its ability to prevent corrosion by elevating the electron density of the active sites on the metal surface.

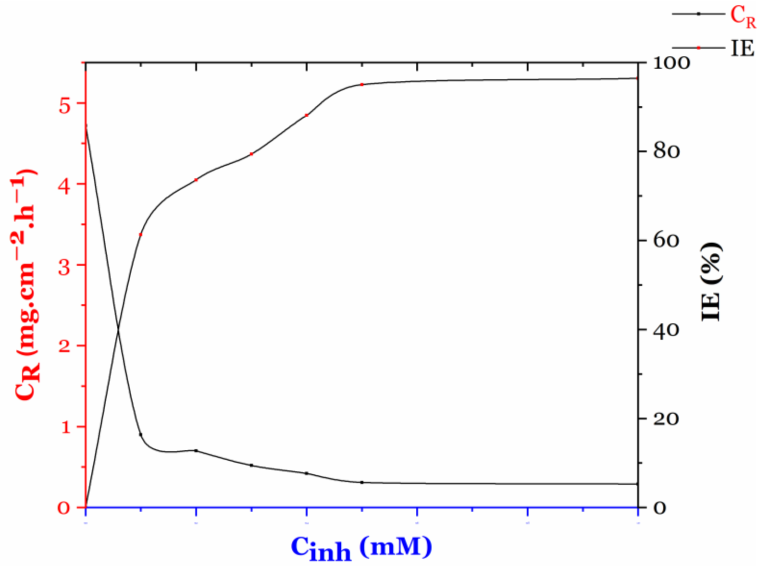

Figure 2: The impact of 4C3T concentration on the corrosion rate and inhibition efficacy of mild steel exposed to 1 M HCl for 5 hours at 303 K.

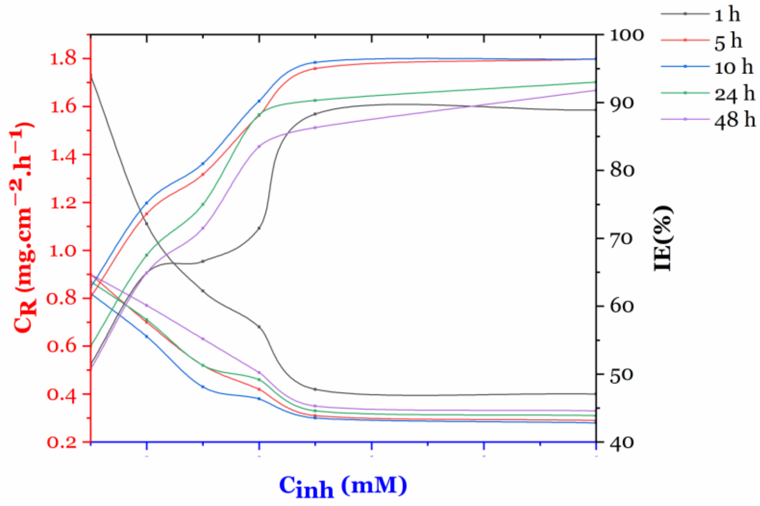

Figure 3: The impact of 4C3T concentration and immersion time on the corrosion rate and inhibition efficacy of mild steel exposed to 1 M HCl at 303 K.

3.1.2. Effect of immersion time

To examine the impact of immersion time on the inhibitory efficacy of 4C3T in reducing corrosion on mild steel, 1 M HCl was treated with varying doses of 4C3T (0.1 to 1.0 mM) for exposure periods ranging from 1 to 48 hours at 303 K. Figure 3 illustrates the findings of the study. During the first 10 hours of immersion, there was a rapid increase in inhibitory efficacy. It remained stable between 10 and 24 hours before gradually decreasing from 24 to 48 hours. Longer exposure times resulted in increased inhibitory effectiveness due to higher concentrations of 4C3T particles adsorbed onto the mild steel surface. As more particles were adsorbed onto the metallic surface, the adsorption density of 4C3T particles also significantly increased. This allowed for physisorption and chemisorption, which are interactions between inhibitor molecules and iron atoms on metallic surfaces. If a few inhibitor molecules leave the surface, the effective area covered by the inhibitor and its inhibitory activity might decrease. The high inhibitory efficacy observed over a long exposure period highlights the stability of the 4C3T particles layer adsorbed in an acidic medium.

3.1.3. Effect of temperature

The study investigated the effects of temperature on the inhibition of mild steel corrosion in acidic solutions treated with 4C3T at concentrations ranging from 0.1 to

1.0 mM. Figure 4 illustrates that as the temperature increased from 303 K to 333 K, the corrosion rate of 4C3T increased, and its inhibition efficiency decreased. The inhibitory effect of 4C3T decreased with increasing temperature, indicating physical adsorption. At high temperatures, 4C3T particles were removed from the metal surface due to adsorption.

At 303 K, the maximum inhibition efficiency for 4C3T was observed at a concentration of 0.5 mM, with 95 % efficiency. However, as the temperature increased, the inhibition efficiency decreased. The inhibitor was less effective at higher temperatures at the highest concentration of 4C3T (1.0 mM) due to physical absorption processes and van der Waals interactions between the 4C3T particles and the mild steel surface.

In the oil and gas production process, the temperature at the bottom of the well is high. Therefore, a suitable corrosion inhibitor should maintain its effectiveness in corrosive media at high temperatures. Figure 4 clearly shows that as the temperature increases, the corrosion rate slightly increases, and the effectiveness of the inhibiting is little affected. This changes is due to the excellent performance of the corrosion inhibitor, which has been specially formulated to maintain its effectiveness even at high temperatures. The importance of an effective corrosion inhibitor in oil and gas production cannot be overstated. Corrosion can cause significant damage to equipment, resulting in costly repairs and downtime. Therefore, it is essential to use a corrosion inhibitor that can withstand the harsh conditions encountered in the production process, including high temperatures and corrosive media. The results shown in Figure 4 provide strong evidence that the corrosion inhibitor used in the production process is highly effective, even at elevated temperatures. It demonstrates the quality of the inhibitor and the expertise of the team that selected and implemented it. The findings of this study underscore the importance of carefully selecting an appropriate corrosion inhibitor for a given production process and ensuring ongoing monitoring and evaluation to ensure continued effectiveness, as highlighted in previous research [22]. Additionally, the study found that increasing the concentration of the inhibitor led to a reduction in corrosion rates at the same temperature, indicating that the concentration of the inhibitor plays a crucial role in enhancing surface coverage of inhibitor chemicals and effectively separating the metallic surface from the corrosive environment [23].

Comparing the inhibitory efficiencies of 4C3T in this study with previously published inhibitors, Figure 5 shows that these inhibitors are suitable for HCl solutions. The results indicate that in the presence of 0.5 mM of 4C3T, the inhibition efficiency reached 96 % at 303 K in a 1 M HCl environment, which surpasses the performance of some previously studied inhibitors [24-53].

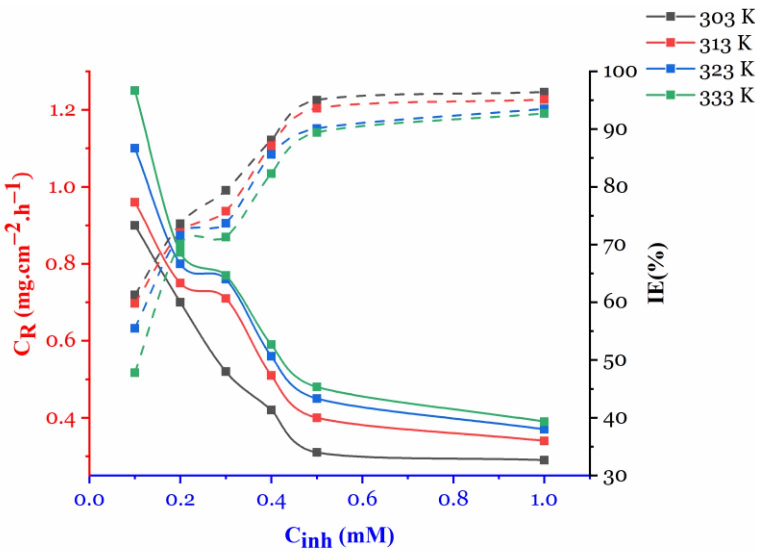

Figure 4: The impact of 4C3T concentration and different temperatures on the corrosion rate and inhibition efficacy of mild steel exposed to 1 M HCl for 5 h.

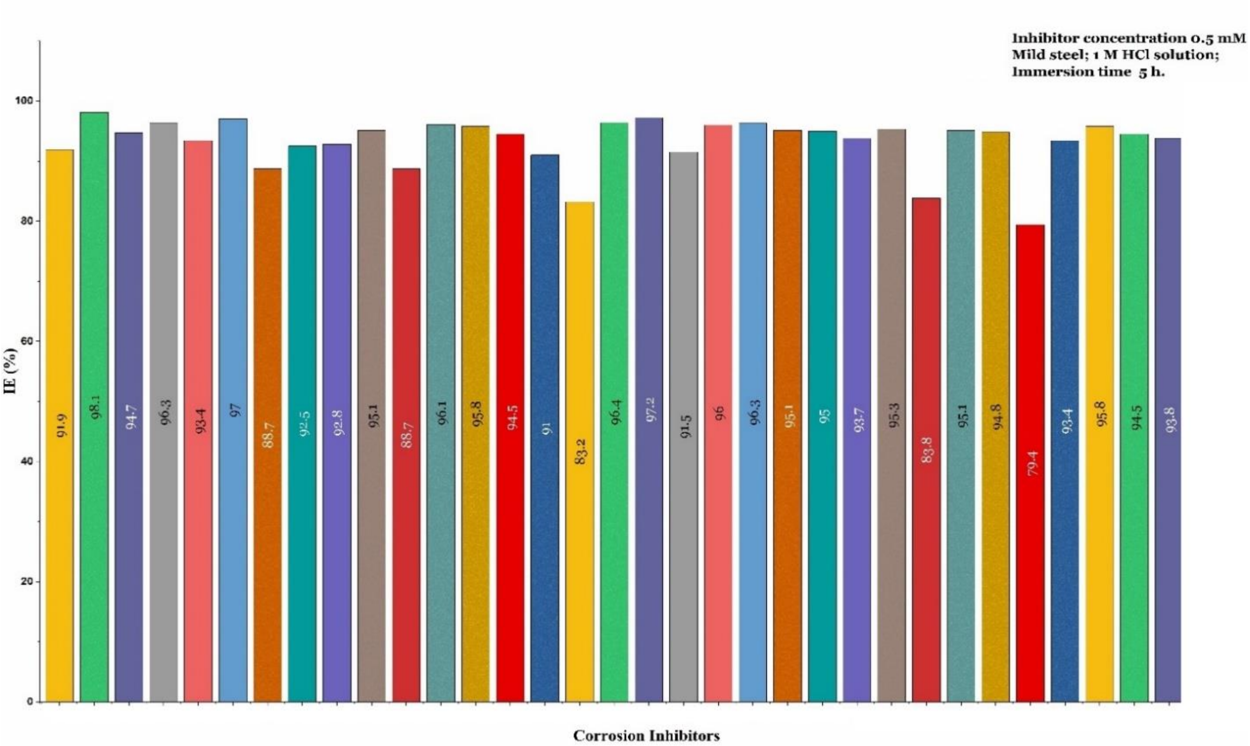

Figure 5: The comparison of tested inhibitors with previously reported inhibitors for corrosion of mild steel in HCl solution.

3.2. Adsorption isotherm

Adsorption isotherms were employed in this study to investigate the mechanism of interaction between 4C3T and the metal surface. Surface coverage (θ) values were determined through gravimetric testing and used to evaluate the most appropriate isotherm model. The Langmuir, Temkin, and Freundlich isotherms were used to analyze the adsorption process, as described in Table 1. Physical or chemical adsorption may have caused the 4C3T particles to adhere to the metal surfaces. Results indicated that the Langmuir adsorption isotherm model was the most suitable for 4C3T with a regression coefficient (R2) of 0.998 at 303 K. The Langmuir isotherm plots between C_{inh}/θ and C_{inh} are represented in Figure 6, and the slope and intercept values for 4C3T were estimated and are presented in Table 1. Equation 11 was used to calculate the adsorption parameters.

$$C_{inh}/\theta = (K_{ads})^{-1} + C \qquad (11)$$

Where C_{inh} is the inhibitor concentration, θ is the area of the tested surface, and K_{ads} is a constant. ΔG_{ads}^{o} and K_{ads} were calculated according to the plot between C/θ and C.

Equation 12 was used to calculate the adsorption parameters ΔG_{ads}^{o} and K_{ads}.

$$\Delta G^{o}_{ads} = -RT\ \ln(55.5K_{ads}) \qquad (12)$$

Where 55.5 is the molar concentration of water, R is the gas constant, and T is Temperature.

The chemisorption mechanism is influenced by the value of ΔG_{ads}^{o}, which should be highly negative, ideally below -40 $kJmol^{-1}$. In contrast, a ΔG_{ads}^{o} value around -20 $kJmol^{-1}$ or less negative indicates physisorption [54-58]. The value of ΔG_{ads}^{o} for 4C3T was determined to be -27.56 $kJmol^{-1}$, indicating that both chemisorption and physisorption mechanisms may be present.

Table 1: The thermodynamic parameters for the 4C3T.

Parameter	303 K	313 K	323 K	333 K
Intercept	0.072	0.078	0.085	0.104
Slope	0.957	0.965	0.978	0.965
R2	0.998	0.998	0.998	0.998

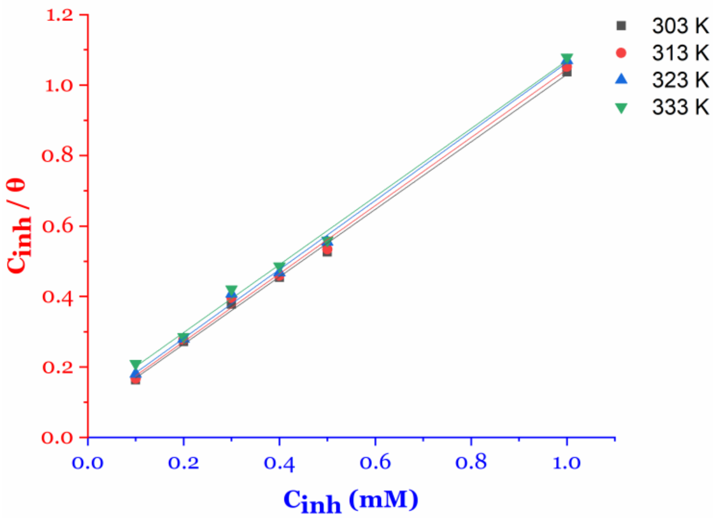

Figure 6: Langmuir isotherm of 4C3T plot for mild steel in HCl.

3.3. Quantum Computations

In general, quantum chemical calculations can provide valuable insights into the mechanism of corrosion inhibition and can help predict potential inhibitors' effectiveness. These calculations typically involve using a computational model to simulate the behavior of the inhibitor molecule in solution and at the metal surface. The choice of basis set and functional for quantum chemical calculations can significantly impact the accuracy and reliability of the results. Commonly used basis sets for quantum chemical calculations include the 6-31G, 6-31G(d), and 6-31+G(d) basis sets, among others. The choice of function, which describes the relationship between electron density and energy, can also significantly affect the accuracy of the results. Common functionals used for corrosion inhibition studies include B3LYP, M06, and PBE. To support the study's findings, we used quantum chemical calculations to investigate the adsorption mechanism of the inhibitor molecule on the mild steel surface and to predict the corrosion inhibition efficiency. The structural properties of 4C3T molecules can be analyzed using the quantum chemical technique, and various thermodynamic parameters can be determined based on the structural parameters of 4C3T at B3LYP/6-311G(d,p) [59, 60]. The Mulliken charges (Table 2) are utilized to identify the inhibitor's adsorption sites [61]. The study outcomes indicate that the negatively charged oxygen and nitrogen atoms are the most favored locations for the inhibitor's adsorption through a donor-acceptor relationship [61]. The benzene ring present in 4C3T molecules supports the formation of complexations between the adsorbate and surface coordination bonds [61]. The highest occupied molecular orbital (HOMO) of 4C3T identifies the molecule's site for electron donation, predominantly observed in the S and N atoms [62]. According to previous studies, the nitrogen, sulfur, and carbon atoms in the molecule are mainly responsible for the molecule's ability to accept electrons, as shown by the shape of the lowest unoccupied molecular orbital (LUMO) [63, 64]. Figure 7 illustrates the equivalent reception sites of 4C3T based on the LUMO shape.

Table 2: The Mulliken charges of 4C3T molecules in the gas phase.

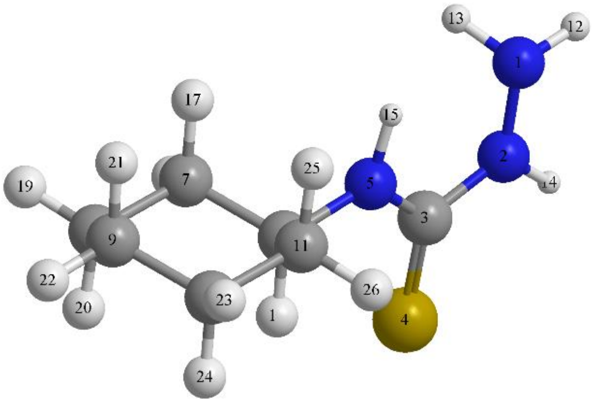

Atom	Charge	Atom	Charge
[N(1)]	-0.161	[C(7)]	-0.074
[N(2)]	0.220	[C(8)]	-0.058
[C(3)]	0.186	[C(9)]	-0.057
[S(4)]	-0.730	[C(10)]	-0.059
[N(5)]	0.028	[C(11)]	-0.068
[C(6)]	0.077	[H(12)]	0.112

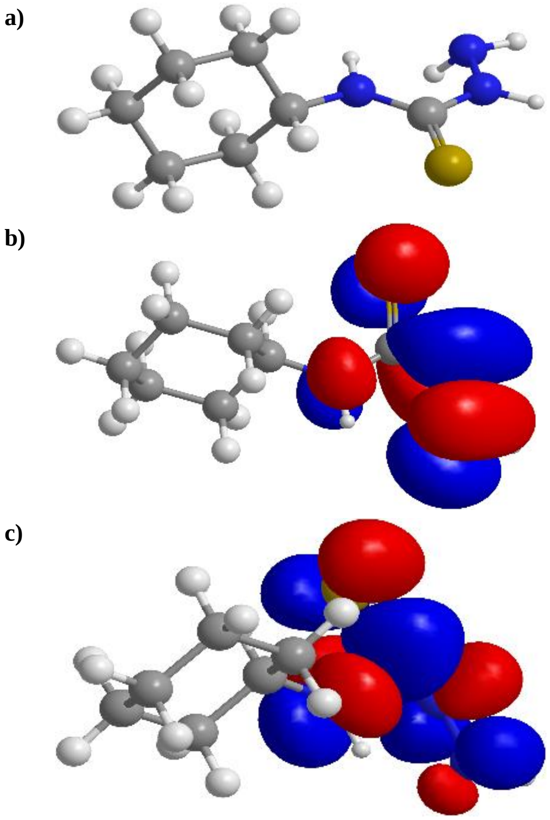

Figure 7: The (a) optimized structure, (b) EHOMO, and (c) ELUMO of 4C3T molecules.

Table 3 shows the results of quantum chemical computations for several parameters such as EHOMO, ELUMO, ΔE, electronegativity (χ), softness (σ), hardness (η), and the number of electrons transported (ΔN) for the inhibitor molecules studied. A higher EHOMO value indicates a better ability of a molecule to donate electrons, which can be transferred from an acceptor molecule with a lower energy empty molecular orbital. For 4C3T, the EHOMO value (-6.139 eV) is consistent with the reported results in Table 2. ELUMO represents a molecule's ability to accept electrons; smaller EHOMO values facilitate this process. Hardness (η) measures the potential chemical change over the total number of atoms, and an increase in η enhances molecule stability. Softness (σ) is a measure of electron cloud polarization, and lower values of ΔE and higher σ are desirable for good corrosion inhibition. The values calculated for 4C3T in Table 2 show that it is a potent corrosion inhibitor with a high ΔN value, indicating better electron exchangeability. These quantitative parameters (EHOMO, ELUMO, ΔE, η, σ, and ΔN) agree well with the test results. The metal's back donation establishes contact between the inhibitor and metal surfaces [65, 66].

Table 3: DFT variables for 4C3T molecules in the gas phase.

Parameter	Value
$I\ eV$	6.139 eV
$A\ eV$	7.927 eV
$E_{HOMO}\ eV$	-6.139 eV
$E_{LUMO}\ eV$	7.927 eV
$\Delta E\ eV$	14.066
$\chi\ eV$	0.89
$\eta\ eV$	-7.033
$\sigma\ eV^{-1}$	-0.14
ΔN	0.5

3.4. Mechanism of inhibition

Organic inhibitors act by adsorbing onto the metal surface, replacing other corrosive species and water molecules [67]. Factors affecting this process include the organic molecule's state in a corrosive environment and the metal surface's charge [68]. In HCl solution, the steel surface is positively charged, attracting chloride ions and leading to the adsorption of cationic species [69].

4C3T, when protonated in 1 M HCl solution, can be electrostatically adsorbed onto the metal surface through physisorption. Nitrogen heteroatoms are released from 4C3T on the surface, forming coordination and back-donating bonds through donor-acceptor interactions (chemisorption) [70-72]. Figure 8 depicts the suggested inhibitory mechanism for 4C3T as a potential inhibitor of mild steel corrosion in 1 M HCl solutions. The coating of 4C3T on the mild steel surface protects the surface from corrosive ions' penetration. The protective coating is believed to form through the interaction of heteroatoms with the metal surface. The mild steel surface's physical adsorption of inhibitor molecules is aided by the electrostatic interaction between the protonated 4C3T molecules and pre-absorbed Cl- ions and the interaction between the inhibitor molecules' electron pairs and the iron's vacant d-orbital [73].

3.5. Potential applications of 4C3T

The findings of this study have important practical implications for industries that rely on mild steel equipment and structures. Using 4C3T as a corrosion inhibitor can provide a cost-effective and environmentally

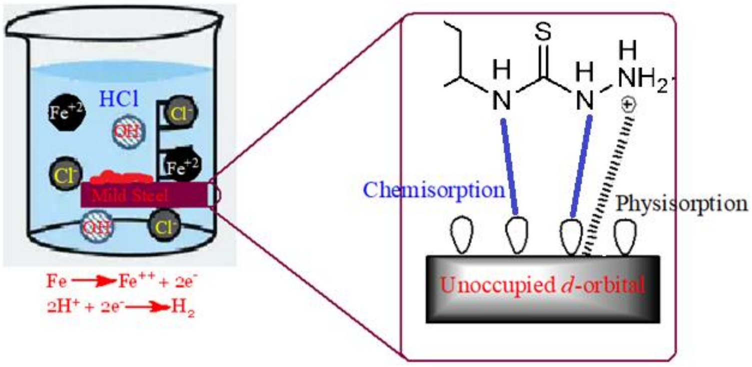

Figure 8: Postulated inhibited mechanism of 4C3T.

friendly method of reducing corrosion in mild steel. The results indicate that a maximal inhibitive efficacy of up to 96 % can be achieved at the optimal concentration of 0.5 mM for a 5-hour immersion period at 303 K. To apply these findings in real-world applications, industries can consider using 4C3T as a corrosion inhibitor in the design and maintenance of mild steel equipment and structures. The optimal concentration and immersion time can be adjusted based on the specific needs and conditions of the application. The Langmuir adsorption isotherms can also be utilized to understand the relationship between the concentration of the inhibitor and the surface coverage of the mild steel, allowing for more accurate and efficient use of the inhibitor.

Additionally, the findings of the quantum chemistry computations can be used to guide the design and development of new and improved corrosion inhibitors. The energies of frontier molecular orbitals (EHOMO & ELUMO) and the energy gap can provide insight into the protection performance of potential inhibitors, allowing for more targeted and effective inhibitor development. Overall, the practical implications of this study suggest that using 4C3T as a corrosion inhibitor can potentially reduce the economic and environmental costs of mild steel corrosion in various industries.

4. Conclusion

In conclusion, the study has demonstrated that 4C3T is an effective inhibitor of mild steel corrosion in 1 M HCl solution. The optimal concentration for inhibitive efficacy was 0.5 mM for a 5-hour immersion period at 303 K, with a maximum inhibitive efficacy of up to 96 %. The study has also shown that the protection performance of 4C3T against mild steel corrosion increases with concentration but decreases slightly with increased immersion time and temperature. The Langmuir adsorption isotherms suggest that 4C3T molecules adsorb onto the metal substrate surface, and both physical and chemical adsorptions are involved in the adsorption mechanism. The observed activation energy values suggest that the chemical adsorption of 4C3T molecules on a mild steel surface is spontaneous. The findings of the quantum chemistry computations also support the weight loss test results, with energies of frontier molecular orbitals and energy gap being consistent with the protection performance. These results have significant implications for future research and practical applications in corrosion inhibition. The study has provided valuable insights into the adsorption mechanism of 4C3T molecules on mild steel surfaces, which could inform the design of more effective corrosion inhibitors. Additionally, the findings highlight the importance of considering immersion time and temperature when assessing the performance of corrosion inhibitors, as well as the need for more environmentally friendly options. Overall, the study provides a promising avenue for developing cost-effective and environmentally friendly corrosion inhibitors for various industries.

5. References

1. N. K. Gupta, M. A. Quraishi, C. Verma, A. K. Mukherjee, Green Schiff's bases as corrosion inhibitors for mild steel in 1 M HCl solution: experimental and theoretical approach, *RSC Adv*., 6(2016), 102076-102087.
2. K. Wan, P. Feng, B. Hou, Y. Li, Enhanced corrosion inhibition properties of carboxymethyl hydroxypropyl chitosan for mild steel in 1.0 M HCl solution, *RSC Adv*., 6(2016), 77515-77524.
3. M. Bobina, A. Kellenberger, J.-P. Millet, C. Muntean, N. Vaszilcsin, Corrosion resistance of carbon steel in weak acid solutions in the presence of l-histidine as corrosion inhibitor, *Corros. Sci.,* 69(2013), 389-395.
4. K. R. Ansari, M. A. Quraishi, Experimental and quantum chemical evaluation of Schiff bases of isatin as a new and green corrosion inhibitors for mild steel in 20% H_2SO_4, *J. Taiwan Inst. Chem. Eng.,* 54(2015), 145-154.
5. A. A. Farag, M. A. Hegazy, Synergistic inhibition effect of potassium iodide and novel Schiff bases on X65 steel corrosion in 0.5 M H_2SO_4, *Corros. Sci.,74(* 2013), 168-177.
6. Sudheer, M. A. Quraishi, 2-Amino-3,5-dicarbonitrile-6-thio-pyridines: new and effective corrosion inhibitors for mild steel in 1 M HCl, *Ind. Eng. Chem. Res.,* 53(2014), 2851-2859.
7. B. Xu, Y. Ji, X. Zhang, X. Jin, W. Yang, Y. Chen, Experimental and theoretical studies on the corrosion inhibition performance of 4-amino-N,N-di-(2-pyridylmethyl)- aniline on mild steel in hydrochloric acid, *RSC Adv.,* 5(2015), 56049-56059.
8. Y. Ji, B. Xu, W. Gong, X. Zhang, X. Jin, W. Ning, Y. Meng, W. Yang, Y. Chen, Corrosion inhibition of a new Schiff base derivative with two pyridine rings on Q235 mild steel in 1.0 M HCl, *J. Taiwan Inst. Chem. Eng.,* 66(2016), 301-312.
9. L. O. Olasunkanmi, I. B. Obot, E. E. Ebenso, Adsorption and corrosion inhibition properties of N-{n-[1-R-5-(quinoxalin-6-yl)-4,5-dihydropyrazol-3-yl]phenyl} methanesulfonamides on mild steel in 1 M HCl: experimental and theoretical studies, *RSC Adv.,* 6(2016), 86782-86797.
10. S. Junaedi, A. A. H. Kadhum, A. Al-Amiery, A.B. Mohamad, M. S. Takriff, Synthesis and characterization of novel corrosion inhibitor derived from oleic acid: 2-Amino-5- Oleyl 1,3,4-Thiadiazol (AOT), *Int. J. Electrochem. Sci.,* 7(2012), 3543-3554.
11. H.S. Aljibori, A.H. Alwazir, S. Abdulhadi, W.K. Al-Azzawi, A. A. H. Kadhum, L. M. Shaker, A. A. Al-Amiery, H.Sh. Majdi, The use of a Schiff base derivative to inhibit mild steel corrosion in 1 M HCl solution: a comparison of practical and theoretical findings, *Int. J. Corros. Scale Inhib.,* 11(2022), 1435-1455.
12. W. K. Al-Azzawi, S. M. Salih, A. F. Hamood, R. K. Al-Azzawi, M. H. Kzar, H. N. Jawoosh, L. M. Shakier, A. Al-Amiery, A. A. H. Kadhum, W. N. R. W. Isahak, M.S. Takriff, Adsorption and theoretical investigations of a Schiff base for corrosion inhibition of mild steel in an acidic environment, *Int. J. Corros. Scale Inhib.*, 11(2022), 1063-1082.
13. D. M. Jamil, A. Al-Okbi, M. Hanon, K.S. Rida, A. Alkaim, A. Al-Amiery, A. Kadhum, A.A.H. Kadhum, Carbethoxythiazole corrosion inhibitor: as an experimentally model and DFT theory, *J. Eng. Appl. Sci.*, 13(2018), 3952-3959.
14. A. Alobaidy, A. Kadhum, S. Al-Baghdadi, A. Al-Amiery, A. Kadhum, E. Yousif, A.B. Mohamad, Eco-friendly corrosion inhibitor: experimental studies on the corrosion inhibition performance of creatinine for mild steel in HCl complemented with quantum chemical calculations, *Int. J. Electrochem. Sci.*, 10(2015), 3961-3972.
15. S. Subhashini, A. Sabirneeza, Gravimetric and electrochemical investigation of water soluble poly(vinyl alcohol-threonine) as corrosion inhibitor for mild steel. In: Proceedings of WCECS, San Francisco, USA, II(2011), 657-662.
16. S. Umoren, M. Solomon, S. Ali, H. Dafalla, Synthesis, Characterization, and utilization of a diallylmethylamine-based cyclopolymer for corrosion mitigation in simulated acidizing environment, *Mater. Sci. Eng.*, 100(2019), 897-914.
17. ASTM, G. G 31-72 American Society for Testing and Materials 1990 Philadelphia.
18. NACE Standard TM 0169/G31-12a. Standard Guide for Laboratory Immersion Corrosion Testing of Metals, (2012).
19. Gaussian 09, Revision D.01, Frisch, M.J.; Trucks, G.W., Schlegel, H.B., Scuseria, G.E., Robb, M.A., Cheeseman, J.R., Scalmani, G., Barone, V., Mennucci, B., Petersson, G.A., Nakatsuji, H., Caricato, M., Li, X., Hratchian, H.P., Izmaylov, A.F., Bloino, J., Zheng, G., Sonnenberg, J.L., Hada, M., Ehara, M., Toyota, K., Fukuda, R., Hasegawa, J., Ishida, M., Nakajima, T., Honda, Y., Kitao, O., Nakai, H.,Vreven, T., Montgomery, Jr., J.A., Peralta, J.E., Ogliaro, F., Bearpark, M., Heyd, J.J., Brothers, E., Kudin, K.N., Staroverov, V.N., Kobayashi, R., Normand, J., Raghavachari, K., Rendell, A., Burant, J.C., Iyengar, S.S., Tomasi, J., Cossi, M., Rega, N., Millam, J.M., Klene, M., Knox, J.E., Cross, J.B., Bakken, V., Adamo, C., Jaramillo, J., Gomperts, R., Stratmann, R.E., Yazyev, O., Austin, A.J., Cammi, R., Pomelli, C., Ochterski, J.W., Martin, R.L., Morokuma, K., Zakrzewski, V.G., Voth, G.A., Salvador, P., Dannenberg, J.J., Dapprich, S.; Daniels, A.D., Farkas, Ö., Foresman, J.B., Ortiz, J.V., Cioslowski, J., Fox, D.J. Gaussian, Inc., Wallingford CT, (2013).
20. Koopmans, T. Ordering of wave functions and eigenenergy's to the individual electrons of an atom. *Physica*, 1(1933), 104-113.
21. S. Al-Bghdadi, M. Hanoon, J. Odah, L. Shaker, A. Al-Amiery, A.A. Benzylidene as Efficient Corrosion

Inhibition of Mild Steel in Acidic Solution. *Proceedings*, 41(2019), 27. https://doi.org/10.3390/ecsoc-23-06472

22. M.M. Solomon, S.A. Umoren, M.A. Quraishi, D. Tripathi, E.J. Abai, Effect of Alkyl Chain Length, Flow, and temperature on the Corrosion Inhibition of Carbon Steel in a Simulated Acidizing Environment by an Imidazoline-Based Inhibitor, *J. Pet. Sci. Eng.*, 187(2020), 106801.
23. B.S. Mahdi, H.S.S. Aljibori, M.K. Abbass, W.K. Al-Azzawi, A.H. Kadhum, M.M. Hanoon, W.N.R.W. Isahak, A.A. Al-Amiery, H.Sh. Majdi, Gravimetric analysis and quantum chemical assessment of 4-aminoantipyrine derivatives as corrosion inhibitors, *Int. J. Corros. Scale Inhib.*,3(202), 1191–1213.
24. A.A. Alamiery, Study of corrosion behavior of N'-(2-(2-oxomethylpyrrol-1-yl) ethyl) piperidine for mild steel in the acid environment, *Biointerface Res. Appl. Chem.*, 12(2022), 3638-3646.
25. A. Alamiery, A. Mohamad, A. Kadhum, M. Takriff, Comparative data on corrosion protection of mild steel in HCl using two new thiazoles, *Data Brief*, 40(2022), 107838.
26. A.M. Mustafa, F.F. Sayyid, N. Betti, L.M. Shaker, M.M. Hanoon, A.A. Alamiery, A.A.H. Kadhum, M.S. Takriff, Inhibition of mild steel corrosion in hydrochloric acid environment by 1-amino-2-mercapto-5-(4-(pyrrol-1-yl)phenyl)-1,3,4-triazole, S. *Afr. J. Chem. Eng.*, 39(2022), 42-51.
27. A.A. Alamiery, Investigations on corrosion inhibitory effect of newly quinoline derivative on mild steel in HCl solution complemented with antibacterial studies, *Biointerface Rese. Appl. Chem.*, 12(2022), 12, 1561-1568.
28. I. A. Alkadir Aziz, I.A. Annon, M.H. Abdulkareem, M.M. Hanoon, M.H. Alkaabi, L.M. Shaker, A.A. Alamiery, W.N.R. Wan Isahak, M.S. Takriff, Insights into corrosion inhibition behavior of a 5-mercapto-1,2,4-triazole derivative for mild steel in hydrochloric acid solution: experimental and DFT studies, *Lubricants*, 9(2021), 122.
29. A. Alamiery, Short report of mild steel corrosion in 0.5 M H_2SO_4 by 4-ethyl-1-(4-oxo4-phenylbutanoyl)thiosemicarbazide, *Tribologi*, 30(2021), 90-99.
30. A.A. Alamiery, W.N.R.W. Isahak, M.S. Takriff, Inhibition of mild steel corrosion by 4-benzyl-1-(4-oxo-4-phenylbutanoyl)thiosemicarbazide: Gravimetrical, adsorption and theoretical studies, *Lubricants*, 9(2021), 93.
31. M.A. Dawood, Z.M.K. Alasady, M.S. Abdulazeez, D.S. Ahmed, G.M. Sulaiman, A.A.H. Kadhum, L.M. Shaker, A.A. Alamiery, The corrosion inhibition effect of a pyridine derivative for low carbon steel in 1 M HCl medium: Complemented with antibacterial studies, *Int. J. Corros. Scale Inhib.*, 10(2021), 1766-1782.
32. A. Alamiery, Corrosion inhibition effect of 2-N-phenylamino-5-(3-phenyl-3-oxo-1- propyl)-1,3,4-oxadiazole on mild steel in 1 M hydrochloric acid medium: Insight from gravimetric and DFT investigations, *Mater. Sci. Energy Technol.*, 4(2021), 398–-406.
33. Alamiery, Anticorrosion effect of thiosemicarbazide derivative on mild steel in 1 M hydrochloric acid and 0.5 M sulfuric Acid: Gravimetrical and theoretical studies, *Mater. Sci. Energy Technol.*, 4(2021), 263–273.
34. Alamiery, W.N.R.W. Isahak, H. Aljibori, H. Al-Asadi, A. Kadhum, Effect of the structure, immersion time and temperature on the corrosion inhibition of 4-pyrrol-1-yln-(2,5-dimethyl-pyrrol-1-yl)benzoylamine in 1.0 m HCl solution, *Int. J. Corros. Scale Inhib.*, 10(2021), 700-713.
35. Alamiery, E. Mahmoudi, T. Allami, Corrosion inhibition of low-carbon steel in hydrochloric acid environment using a Schiff base derived from pyrrole: gravimetric and computational studies, *Int. J. Corros. Scale Inhib.*, 10(2021), 749-765.
36. A.J.M. Eltmimi, A. Alamiery, A.J. Allami, R.M. Yusop, A.H. Kadhum, T. Allami, Inhibitive effects of a novel efficient Schiff base on mild steel in hydrochloric acid environment, *Int. J. Corros. Scale Inhib.*, 10(2021), 634-648.
37. A. Alamiery, L.M. Shaker, T. Allami, A.H. Kadhum, M.S. Takriff, A study of acidic corrosion behavior of Furan-derived Schiff base for mild steel in hydrochloric acid environment: Experimental, and surface investigation, *Mater. Today: Proc.*, 44(2021), 2337-2341.
38. S. Al-Baghdadi, A. Al-Amiery, T. Gaaz, A. Kadhum, Terephthalohydrazide and isophthalo-hydrazide as new corrosion inhibitors for mild steel in hydrochloric acid: Experimental and theoretical approaches, *Koroze Ochr. Mater.*, 65(2021), 12-22.
39. M.M. Hanoon, A.M. Resen, L.M., Shaker, A. Kadhum, A. Al-Amiery, Corrosion investigation of mild steel in aqueous hydrochloric acid environment using n- (Naphthalen-1yl)-1-(4-pyridinyl)methanimine complemented with antibacterial studies, *Biointerface Res. Appl. Chem.*, 11(2021), 9735–-9743.
40. S. Al-Baghdadi, T.S. Gaaz, A. Al-Adili, A. Al-Amiery, M. Takriff, Experimental studies on corrosion inhibition performance of acetylthiophene thiosemicarbazone for mild steel in HCl complemented with DFT investigation, *Int. J. Low-Carbon Technol.*, 16(2021), 181-188.
41. A. Al-Amiery, Anti-corrosion performance of 2-isonicotinoyl-nphenylhydrazinecarbothioamide for mild steel hydrochloric acid solution: Insights from experimental measurements and quantum chemical calculations, *Surf. Rev. Lett.*, 28(2021), 2050058.
42. M.S. Abdulazeez, Z.S. Abdullahe, M.A. Dawood, Z.K. Handel, R.I. Mahmood, S. Osamah, A.H. Kadhum, L.M. Shaker, A.A. Al-Amiery, Corrosion inhibition of low carbon steel in HCl medium using a thiadiazole derivative: weight loss, DFT studies and

antibacterial studies, *Int. J. Corros. Scale Inhib.*, 10(2021), 1812-1828.

43. A. Mustafa, F. Sayyid, N. Betti, M. Hanoon, A. Al-Amiery, A. Kadhum, M. Takriff, Inhibition evaluation of 5-(4-(1H-pyrrol-1-yl)phenyl)-2-mercapto-1,3,4-oxadiazole for the corrosion of mild steel in an acid environment: Thermodynamic and DFT Aspects, *Tribologia*, 38(2021), 39-47.
44. Y.M. Abdulsahib, A.J.M. Eltmimi, S.A. Alhabeeb, M.M. Hanoon, A.A. Al-Amiery, T. Allami, A.A.H. Kadhum, Experimental and theoretical investigations on the inhibition efficiency of N-(2,4-dihydroxytolueneylidene)-4-methylpyridin-2-amine for the corrosion of mild steel in hydrochloric acid, *Int. J. Corros. Scale Inhib.*, 10(2021), 885-899.
45. A.K. Khudhair, A.M. Mustafa, M.M. Hanoon, A. Al-Amiery, L.M. Shaker, T. Gazz, A.B. Mohamad, A.H. Kadhum, M.S. Takriff, Experimental and theoretical investigation on the corrosion inhibitor potential of N-MEH for mild steel in HCl, *Prog. Color, Colorant Coat.*, 15(2022), 111-122.
46. D.S. Zinad, R.D. Salim, N. Betti, L.M. Shaker, A.A. AL-Amiery, Comparative investigations of the corrosion inhibition efficiency of a 1-phenyl- 2-(1-phenylethylidene)hydrazine and its analog against mild steel corrosion in hydrochloric acid solution, *Prog. Color, Colorant Coat.*, 15(2022), 53-63.
47. R.D. Salim, N. Betti, M. Hanoon, A.A. Al-Amiery, 2-(2,4-Dimethoxybenzylidene)-N-phenylhydrazinecarbothioamide as an efficient corrosion inhibitor for mild steel in acidic environment, *Prog. Color, Colorant Coat.*, 15(2021), 45-52.
48. A.A. Al-Amiery, L.M. Shaker, A.H. Kadhum, M.S. Takriff, Exploration of furan derivative for application as corrosion inhibitor for mild steel in hydrochloric acid solution: Effect of immersion time and temperature on efficiency, *Mater. Today: Proc.*, 42(2021), 2968-2973.
49. A.M. Resen, M.M. Hanoon, W.K. Alani, A. Kadhim, A.A. Mohammed, T.S. Gaaz, A.A.H. Kadhum, A.A. Al-Amiery, M.S. Takriff, Exploration of 8-piperazine-1- ylmethylumbelliferone for application as a corrosion inhibitor for mild steel in hydrochloric acid solution, *Int. J. Corros. Scale Inhib.*, 10(2021), 368-387.
50. M.M. Hanoon, A.M. Resen, A.A. Al-Amiery, A.A.H. Kadhum, M.S. Takriff, Theoretical and experimental studies on the corrosion inhibition potentials of 2-((6-methyl-2-ketoquinolin-3-yl)methylene) hydrazinecarbothioamide for mild steel in 1 M HCl, *Prog. Color, Colorant Coat.*, 15(2021), 21-33.
51. F.G. Hashim, T.A. Salman, S.B. Al-Baghdadi, T. Gaaz, A.A. Al-Amiery, Inhibition effect of hydrazine-derived coumarin on a mild steel surface in hydrochloric acid, *Tribologia*, 37(2020), 45-53.
52. A.M. Resen, M. Hanoon, R.D. Salim, A.A. Al-Amiery, L.M. Shaker, A.A.H. Kadhum, Gravimetrical, theoretical, and surface morphological investigations of corrosion inhibition effect of 4-(benzoimidazole-2-yl) pyridine on mild steel in hydrochloric acid, *Koroze Ochr. Mater.*, 64(2020), 122-130.
53. A.Z. Salman, Q.A. Jawad, K.S. Ridah, L.M. Shaker, A.A. Al-Amiery, Selected BIS thiadiazole: synthesis and corrosion inhibition studies on mild steel in HCl environment, *Surf. Rev. Lett.*, 27(2020), 2050014.
54. S. Junaedi, A. Al-Amiery, A. Kadihum, A. Kadhum, A. Mohamad, Inhibitioneffects of a synthesized novel 4-aminoantipyrine derivative on the corrosion of mild steel in hydrochloric acid solution together with quantum chemicalstudies, *Int. J. Mol. Sci.*, 13(2013), 11915-11928.
55. A. Alamiery, W.N.R.W. Isahak, H.S.S. Aljibori, H.A. Al- Asadi, A.A.H. Kadhum, Effect of the structure, immersion time and temperature on the corrosion inhibition of 4- pyrrol-1-yl-n-(2,5-dimethyl-pyrrol-1-yl)benzoylamine in 1.0 M HCl solution, *Int. J. Corros. Scale Inhib.*, *I10(*2021), 700-713.
56. S. Al-Baghdadi, F. Hashim, A. Salam, T. Abed, T. Gaaz, A. Al-Amiery, A.H. Kadhum, K. Reda, W. Ahmed, Synthesis and corrosion inhibition application of NATN on mild steel surface in acidic media complemented with DFT studies, *Results Phys.*, 8(2018), 1178-1184.
57. H.M. Abd El-Lateef, Corrosion inhibition characteristics of a novel salycilidene isatin hydrazine sodium sulfonate on carbon steel in HCl and a synergistic nickel ions additive: a combined experimental and theoretical perspective, *Appl. Surf. Sci.*, 501(2020), 144237.
58. I.B. Onyeachu, I.B. Obot, A.A. Sorour, M.I. Abdul-Rashid, Green corrosion inhibitor for oilfield application I: electrochemical assessment of 2-(2-Pyridyl) benzimidazole for API X60 steel under sweet environment in NACE brine ID196, *Corros. Sci.*, 150(2019), 183-193.
59. S.A. Umoren, M.M. Solomon, Protective polymeric films for industrial substrates: a critical review on past and recent applications with conducting polymers and polymer composites/nanocomposites, *Prog. Mater. Sci.*, 104(2019), 380-450.
60. W.K. Al-Azzawi, A.J. Al Adily, F.F. Sayyid, R.K. Al-Azzawi, M.H. Kzar, H.N. Jawoosh, A.A. Al-Amiery, A.A.H. Kadhum, W.N.R.W. Isahak, M.S. Takriff, Evaluation of corrosion inhibition characteristics of an N-propionanilide derivative for mild steel in 1 M HCl: Gravimetrical and computational studies, *Int. J. Corros. Scale Inhib.*, 11(2022), 1100-1114.
61. H. Ma, S. Chen, B. Yin, S. Zhao, X. Liu, Impedance spectroscopic study of corrosion inhibition of copper by surfactants in the acidic solutions, *Corros. Sci.*, 45(2003), 867-882.
62. G. Banerjee, S.N. Malhotra, Contribution to adsorption of aromatic amines on mild steel surface from HCl solutions by impedance, UV, and Raman spectroscopy, *Corrosion*, 48(1992), 10-15.

63. M. Lebrini, M. Lagrenee, H. Vezin, L. Gengembre, F. Bentiss, Electrochemical and quantum chemical studies of new thiadiazole derivatives adsorption on mild steel in normal hydrochloric acid medium, *Corros. Sci.*, 47(2005), 485-505.
64. S. Deng, X. Li, Inhibition by Jasminum nudiflorum Lindl. leaves extract of the corrosion of aluminium in HCl solution, *Corros. Sci.*, 64(2012), 253-262.
65. G. Karthik, M. Sundaravadivelu, P. Rajkumar, Corrosion inhibition and adsorption properties of pharmaceutically active compound esomeprazole on mild steel in hydrochloric acid solution, *Res. Chem. Intermed*., 41(2015), 1543-1558.
66. M. Farsak, H. Kelesand, M. Keles, A new corrosion inhibitor for protection of low carbon steel in HCl solution, *Corros. Sci.*, 98(2015), 223-232.
67. S.A. Umoren, M.M. Solomon, S.A. Ali, Dafalla, H.D.M. Synthesis, characterization, and utilization of a diallylmethylamine-based cyclopolymer for corrosion mitigation in simulated acidizing environment, *Mater. Sci. Eng. C*, 100(2019), 897-914.
68. H.M. Abd El-Lateef, Corrosion inhibition characteristics of a novel salycilidene isatin hydrazine sodium sulfonate on carbon steel in HCl and a synergistic nickel ions additive: a combined experimental and theoretical perspective, *Appl. Surf. Sci.*, 501(2020), 144237.
69. I.B. Onyeachu, I.B. Obot, A.A. Sorour, M.I. Abdul-Rashid, Green corrosion inhibitor for oilfield application I: electrochemical assessment of 2-(2-Pyridyl) benzimidazole for API X60 steel under sweet environment in NACE brine ID196, *Corros. Sci.*, 150(2019), 183-193.
70. S.A. Umoren, M.M. Solomon, Protective polymeric films for industrial substrates: a critical review on past and recent applications with conducting polymers and polymer composites/nanocomposites, *Prog. Mater. Sci.*, 104(2019), 380-450.
71. M.M. Solomon, S.A. Umoren, M.A. Quraishi, D. Tripathi, E.J. Abai, Effect of alkyl chain length, flow, and temperature on the corrosion inhibition of carbon steel in a simulated acidizing environment by an imidazoline-based inhibitor, *J. Pet. Sci. Eng.*, 187(2020), 106801.
72. R. Solmaz, G. Kardaş, M. Çulha, B. Yazici, M. Erbil, Investigation of adsorption and inhibitive effect of 2-mercaptothiazoline on corrosion of mild steel in hydrochloric acid media, *Electrochim. Acta*, 53(2008), 5941-5952.
73. W.K. Al-Azzawi, A.J. Al Adily, F.F. Sayyid, R.K. Al-Azzawi, M.H. Kzar, H.N. Jawoosh, A.A. Al-Amiery, A.A.H. Kadhum, W.N.R.W. Isahak, M.S. Takriff , Evaluation of corrosion inhibition characteristics of an N-propionanilide derivative for mild steel in 1 M HCl: Gravimetrical and computational studies, *Int. J. Corros. Scale Inhib.*, 11(2022), 1100-1114.

How to cite this article:
A. Mohammed, A. Y. I. Rubaye, W. K. Al-Azzawi, A. Alamiery, Investigation of the Corrosion Inhibition Properties of 4-Cyclohexyl-3-Thiosemicarbazide on Mild Steel in 1 M HCl Solution. Prog. Color Colorants Coat., 16 (2023), 347-359.

PROGRESS
IN COLOR, COLORANTS AND COATINGS

available online @ www.pccc.icrc.ac.ir
Progress in Color Colorants Coating 16 (2023), 361-375

Ministry of Science, Research and Technology
Institute for Color Science & Technology

Evaluation of Coatings Suitability for Buried SS316L Pipelines

S. Ghosal*[1], R. Dey[1], B. Duari[2]
[1] Deptartment of Metallurgical and Materials Engineering, Jadavpur University, P.O. Box: 700032, Kolkata, India.
[2] Corrosion Specialist, A/172 Lake Gardens, P.O. Box: 700045, Kolkata, India.

ARTICLE INFO

Article history:
Received: 30 Jan 2023
Final Revised: 10 May 2023
Accepted: 12 May 2023
Available online: 03 Sep 2023

Keywords:
SS316L pipes
Polymeric coatings
SEIR test
EIS test
Coatings suitability

ABSTRACT

Six polymeric coatings viz 3LPE, 3p/2p CAT, PU, VE, LE, and HSS have been selected, and each type of coating has been applied separately on SS316L pipe external surface. The test samples were subjected to Specific Electrical Insulation Resistance (SEIR) test in 0.1 mol/liter of NaCl solution and the Electrochemical Impedance Spectroscopy (EIS) test in 3.5 % NaCl solution. After completion of the tests, SEIR values of PU, 3LPE, and LE are found to be about 2.5×10^9, 8.9×10^8, and 3.9×10^8 ohm.m^2, respectively. In contrast, the electrochemical impedance values at low frequencies (100 mHz) of 3LPE, 3p/2p CAT, and HSS are found to be about 7.9×10^{11}, 5.4×10^{11}, and 4.5×10^{11} ohm.cm^2, respectively. The experimental results are analyzed, and the ranking of coatings has been made based on each test's performance. The overall ranking of coatings is evaluated for the determination of the suitability of the coating for buried SS316L pipelines in the petroleum, petrochemical, and natural gas industries. Prog. Color Colorants Coat. 16 (2023), 361-375© Institute for Color Science and Technology.

1. Introduction

The petrochemical products are transported via buried SS316L pipelines. These pipelines are installed mostly buried and marginally overground. Overground SS316L pipelines do not need corrosion protection due to 1-3 nm (nanometre) thick chromium oxide (Cr_2O_3) passive layer [1, 2]. In buried condition, an uncoated SS316L pipeline is excellent in high-resistivity soil with a good drainage system [3]. Still, an uncoated SS316L pipeline is uncertain in low-resistivity soil with chloride ions (Cl^-) and an oxygen deficiency [4]. Cl^- ions destroy the passive layer and lead to forming of corrosion pits on the SS316L surface [5]. The porous corrosion products cover pits and remain undetectable until they leak [6]. Localized pitting corrosion penetrates rapidly to the thickness of the SS316L pipeline and perforates the SS316L pipeline within a few days [7]. The mechanism of pitting corrosion and the subsequent failure of buried SS316L pipeline are shown in Figures 1 a and b. It is, therefore, imperative to apply external polymeric (organic) protective coatings on buried SS316L pipelines for the safe transportation of petrochemical products.

A thorough literature survey, including analysis of research papers, reveals that so far, most of the studies on polymeric coatings focused primarily on the analysis of coatings performances and suitability for buried carbon steel pipelines. Many researchers have devoted research efforts to studying metallic and organic coatings on SS316L substrates for marine environments or to studying the pitting corrosion of SS316L under thermal insulation. But, to date, less attention has been paid to the research on coatings performances and suitability for buried SS316L pipelines, and there is a research gap that remains unanswered in this field. To address this outstanding

---

*Corresponding author: * ghosal.surajit@gmail.com

Doi: 10.30509/pccc.2023.167085.1203

gap, the present study has chosen six external polymeric coatings commonly used for buried carbon steel pipelines in the petroleum, petrochemical, and natural gas industries for buried SS316L pipelines. Each type of coating has been applied separately on each 4-inch SS316L pipe external surface after surface preparation. The test samples extracted from the coated SS316L pipes have been subjected to SEIR and EIS tests to investigate the coatings' electrical and electrochemical properties, barrier, or degradation properties. The experimental data are evaluated by comparing the coating's performances and determining the suitability of the coating for buried SS316L pipelines in the petroleum, petrochemical, and natural gas industries.

2. Experimental

2.1. Chemical composition analysis and corrosion tests of SS316L material

Test samples were drawn from 4-inch SS316L pipes for chemical composition analysis and corrosion tests. Cyclic potentiodynamic polarization test [8] was conducted at 25 °C using a three-electrode system within a glass cell filled up with 3.5 % sodium chloride (NaCl) solution according to ASTM Standard Test Method G61 [9]. After 1 hour of immersion, scanning was done at a rate of 10 mV/minute within a potential range from - 400 mV to + 600 mV with Gill AC Potentiostat with 5 channels, Make ACM Instruments [10]. Critical Pitting Potential (CPP, E_{PIT}) values were evaluated from the polarization plots. Significant pitting corrosion was observed under Scanning Electron Microscopy (SEM), Model No. EVO 40, Make: Carl Zeiss AG [11]. A critical Pitting Temperature (CPT) test was conducted at 22-24 °C in reagent grade 6 % ferric chloride ($FeCl_3$) solution as per ASTM Standard Test Method G48 [12] in determining the minimum temperature to produce a pitting attack on the SS316L surface.

2.2. Surface preparation of SS316L pipes

The external surfaces of 4-inch SS 316L pipes were prepared by fused alumina fine particles for a high level of adhesion [13]. Surfaces were made dry and free from contamination prior to coating. Fused alumina particles, original pipe surface, and pipe surface after blasting are shown in Figure 2 a, b, and c, respectively.

2.3. Types of polymeric coatings

Six generic types of polymeric coatings have been selected, and each type of coating has been applied separately on each 4-inch SS316L pipe external surface after surface preparation. The generic types of coatings are as follows:

1) 3Layer Polyethylene (**3LPE**), 2) 3ply/2ply Cold Applied Tape (**3p/2p CAT**), 3) Solvent-free Liquid-applied Polyurethane (**PU**), 4) Non-crystalline Visco-Elastic polyolefin with polymeric tape outer wrap (**VE**), 5) Solvent-free Liquid-applied Epoxy (**LE**) and 6) Polyethylene-based Heat-Shrinkable Sleeve (**HSS**).

The specifications that address requirements for qualification, application and testing of external coatings for buried or submerged carbon steel pipelines in the petroleum, petrochemical and natural gas industries are considered applicable to external coatings for buried SS316L pipelines. Brief descriptions of coatings, including application method and drying time, are given below:

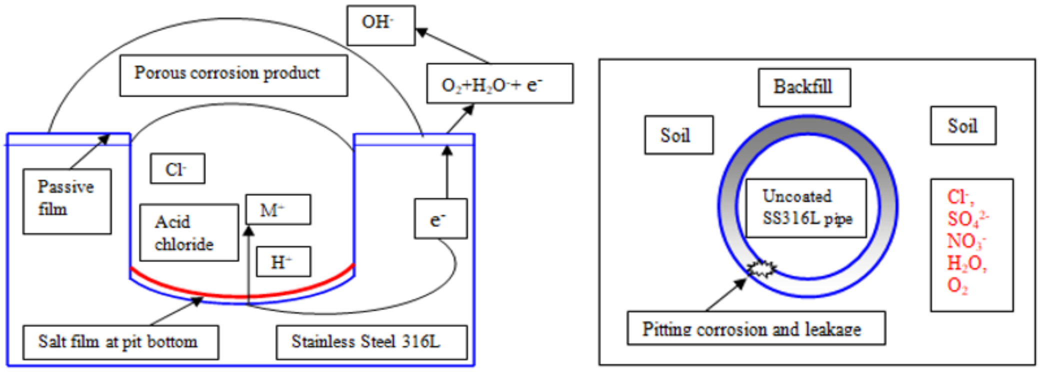

(a) (b)

Figure 1: (a) Schematic diagram on mechanism of pitting corrosion, (b) Failure of buried SS316L pipeline.

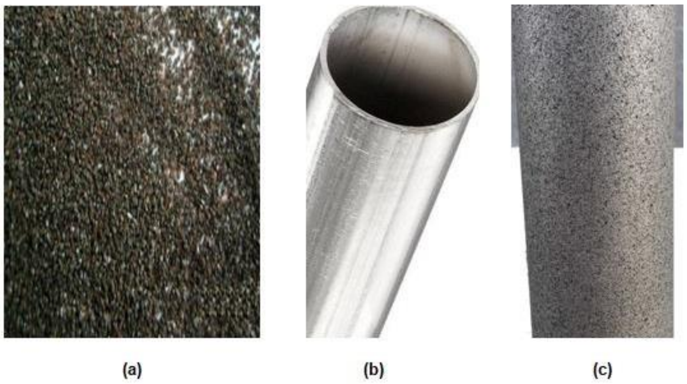

Figure 2: Surface preparation of SS316L pipe - (a) fused alumina fine particles, (b) original pipe surface and (c) pipe surface after blasting.

1) 3Layer polyethylene (3LPE)

This coating system is plant-applied three-layer side extruded polyethylene and conforms to the requirements as per ISO 21809-1 [14]. This anti-corrosion system consists of a high-performance fusion bonded epoxy primer (FBE, minimum 200 microns) first layer followed by a copolymer adhesive second layer (a maleic anhydride grafted polyethylene compound, about 200-250 microns) and the third layer is an outer layer of high-density polyethylene, HDPE (about 2400-2600 microns) with UV stabilizers, which provides tough, durable protection. After blasting and cleaning the pipe from contamination, the pipe is heated by induction heating at about 200 °C. FBE powder is sprayed on this heated pipe surface. FBE easily melts and provides excellent adhesion to steel. The adhesive layer is applied by extrusion before the gel time of FBE coating. Extruded polyethylene layer is applied over the adhesive layer immediately. 3LPE coated pipe is then sent for water quenching and holiday detection test. This coating system is applied in the plant only. This coating system provides corrosion protection of buried pipelines at operating temperatures from - 40 to 80 °C.

2) 3ply/2ply Cold applied tape (3p/2p CAT)

The cold-applied multilayer coating system conforms to the requirements as per ISO 21809-3 [15] and consists of a liquid adhesive primer (butyl rubber), a 3ply anti- corrosion inner layer (HDPE and butyl rubber co-extruded coating), and a mechanical outer layer (MDPE with UV stabilizers). After blasting, the pipe surface is made clean & dry and free from contamination. A liquid adhesive primer (about 80-100 microns) is applied uniformly on the pipe surface. 3ply anti-corrosion inner layer (tape thickness about 800 microns) is applied spirally (with no less than a 50 % overlap) over the primer when it is dry to touch. The outer layer (tape thickness of about 500 microns) is also applied spirally (with no less than a 50 % overlap) over the inner layer. The applied thickness of 3p/2p CAT is about 2500 microns or more. This coating system is applied in the plant and the field. This coating system provides corrosion protection of buried pipelines at the maximum operating temperature of 55±5 °C.

3) Liquid-applied polyurethane (PU)

An aromatic thermoset polyurethane is a reaction product of a polyol (resin) and diphenylmethane diisocyanate (MDI, activator). Liquid-applied PU coating is solvent free (100 % volume solid) and conforms to the requirements as per ISO 21809-3. After thoroughly mixing the resin and activator (typically 3:1 ratio in volume), the coating is applied by using heated plural component airless equipment to the blast-cleaned pipe surface to achieve a thickness of about 1000-1500 microns in a single coat. This coating system is applied in the plant and the field. This coating system provides corrosion protection of buried pipelines at operating temperatures from - 20 to 80 °C.

4) Non-crystalline visco-elastic polyolefin with polymeric tape outer wrap (VE)

This cold-applied non-crystalline, non-cross-linked, non-reactive poly-isobutene wrap (about 2000-2500 microns thick) has a direct bond to the substrate. and conforms to the requirements as per ISO 21809-3. Over poly-isobutene wrap, an ultraviolet-resistant flexible polyvinyl chloride (PVC, about 500 microns thick) tape coated with a rubber resin adhesive is applied. This coating system is applied in the plant and in the field. This system provides corrosion protection for buried pipelines at the maximum operating temperature of 60 °C.

5) Liquid-applied epoxy (LE)

A high-build solvent-free (100 % volume solid) consists of two-component (part-A and part-B) novolac based epoxy and conforms to the requirements as per ISO 21809-3. After thoroughly mixing part A and part B (usually 3.5:1 ratio in volume), the coating is applied by using heated plural component airless equipment to the blast-cleaned pipe surface to achieve a thickness of about 800-1500 microns in a single coat. This coating system is usually applied in the field. This coating system provides corrosion protection of buried pipelines at the maximum operating temperature from - 20 to 80 °C.

6) Heat-Shrinkable Sleeve (HSS)

A wrap-around heat-shrinkable sleeve replicates the plant-applied 3LPE coating and and conforms to ISO 21809-3. The first layer is solvent free two component liquid epoxy primer (about 200 microns), the second layer is copolymer hot melt adhesive (about 200 microns), and the third layer is radiation cross-linked HDPE with UV stabilizers (about 2000-2500 microns thick). The blast-cleaned pipe surface is heated at about 80 °C, and solvent-free two-component liquid epoxy primer is applied to the pipe surface. Heat-Shrinkable Sleeve is wrapped around immediately over the wet epoxy. The sleeve is then heated with a propane torch until it shrinks and fits tightly around the joint. This coating system is mostly applied in the field for field joints and is sometimes applied in the plant for pipe bend joints. This coating system provides corrosion protection of buried pipelines at the maximum operating temperature of 80 °C.

2.4. Preparation of test samples - thickness measurements and holiday tests

The test samples of the coating materials were prepared after cold cutting pipe segments from main 4-inch coated pipes to conduct SEIR and EIS tests. The SEIR and EIS tests were carried out for each coating of the three samples. DeFelsko digital thickness gauge, Model No. PosiTector 6000, Make DeFelsko Inspection Instruments [16] performed the thickness measurement of the coating. The entire surface of each coating was subjected to a holiday test by the holiday detectors, Model Nos. DC-05 (up to 5 kV) and SD-120 (from 8kV to 30 kV), Make Associate Electronics [17] applying voltage based on the type of coating and thickness as per NACE Standard SP0274 [18] to ensure each coating surface was free from holidays (pinholes or defects).

2.5. SEIR tests of coatings

SEIR test is a very simple and convenient experimental method that covers a procedure for quantitatively measuring the specific electrical insulation resistance of a coating by applying a Direct Current (DC). Three test samples of each coating were immersed vertically in 0.1 mol/liter of NaCl solution (0.58 % NaCl solution) in the plastic container according to International Standard ISO 21809-3. Caltech Specific Electrical Insulation Resistance Tester, Model No, performed SEIR test. SISR-05, Make: Caltech Engineering Services [19] at 23-25 °C for 100 days of immersion. The submerged pipe end of the coated sample was sealed with a non-conductive sealant so that there was no contact with the NaCl solution. During each measurement, the pipe end of the coated sample in the open air and not immersed was connected to the positive pole of the DC power supply. The negative pole of the DC power supply was connected to the counter electrode, a copper rod of 10 cm^2. The measurements were taken at intervals with an applied voltage of 100V. A schematic diagram of the SEIR test and a coated sample under SEIR testing are shown in Figure 3a and b, respectively. Six types of coated test samples immersed in NaCl solutions in plastic containers are shown in Figure 4.

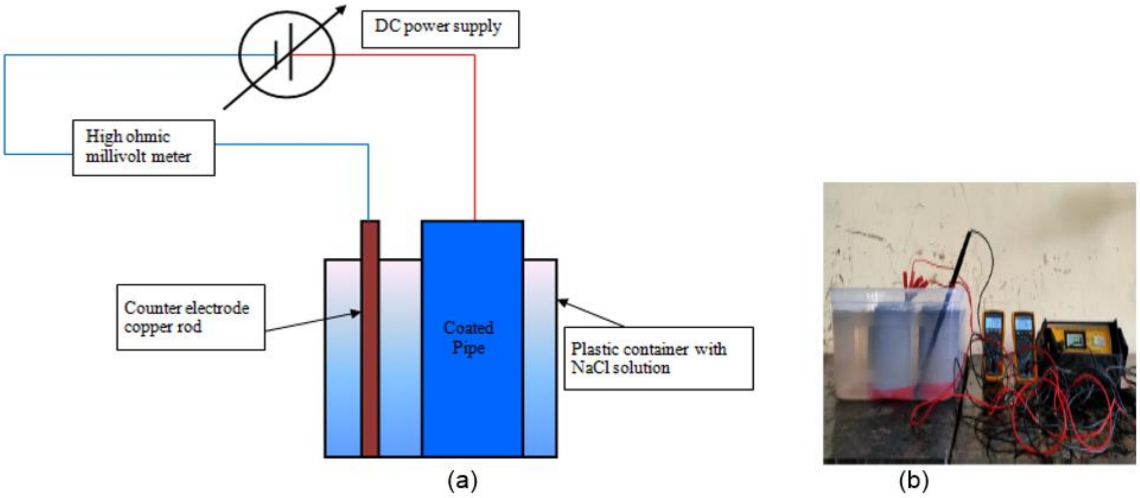

Figure 3: (a) Schematic diagram of SEIR test and (b) A coated sample under SEIR testing.

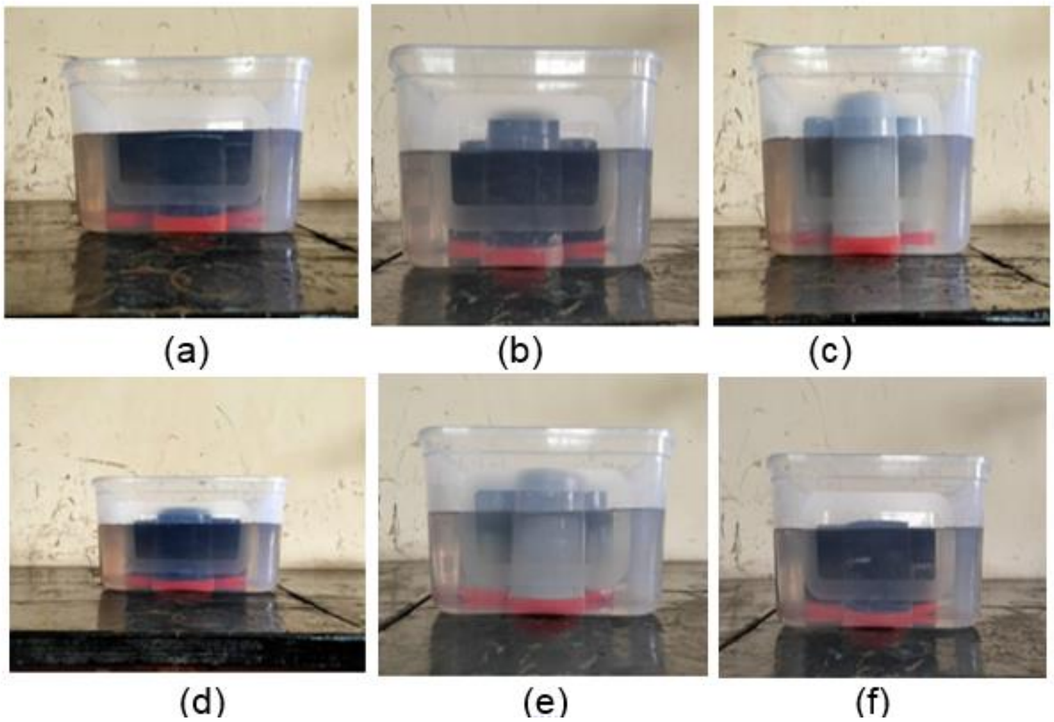

Figure 4: Coated test samples –(a) 3LPE, (b) 3p/2p CAT, (c) PU, (d) VE and (e) LE, (f) HSS.

2.6. EIS tests of coatings

EIS test method is an Alternating Current (AC) impedance method for measuring the impedance and capacitance of a coating quantitatively, for investigating the electrical and electrochemical properties, barrier, or degradation properties of a coating [20-22]. EIS measurements, and data generated within short testing times are more reliable to predict the long-term performance of coatings. Therefore, EIS is a well-established method to investigate the corrosion resistance and anti-corrosion performance of protective coatings [23]. The experimental procedure for collecting electrochemical impedance data was performed according to ASTM Standard Practice G106 [24] with the attached cells consisting of glass tubes cemented to coated SS316L pipes. The attached cell contained a coated pipe surface as Working Electrode (WE), a graphite rod as Counter Electrode (CE), and a Saturated Calomel Electrode (SCE) as Reference Electrode (RE). The attached cell was filled with 3.5 % NaCl solution.

CE and RE were inserted into the solution. EIS tests were done on three-layer samples by GAMRY Instruments, Model No. Reference 600+, Make GAMRY Instruments [25] at 23-25 °C for 14 days. The measurements were carried out on the 1st day, 7th day, and 14th day at open circuit potential with an applied AC voltage of 100 mV_{rms} in amplitude in the frequency range of 100 kHz - 10 mHz. During data collection of electrochemical impedances and capacitances, the samples were placed inside the Faraday cage to minimize electromagnetic interference and noise. A Schematic circuit diagram of the EIS test and a coated sample inside the Faraday cage under testing are shown in Figures 5a and b, respectively. Six types of coated test samples with attached cells are shown in Figure 6.

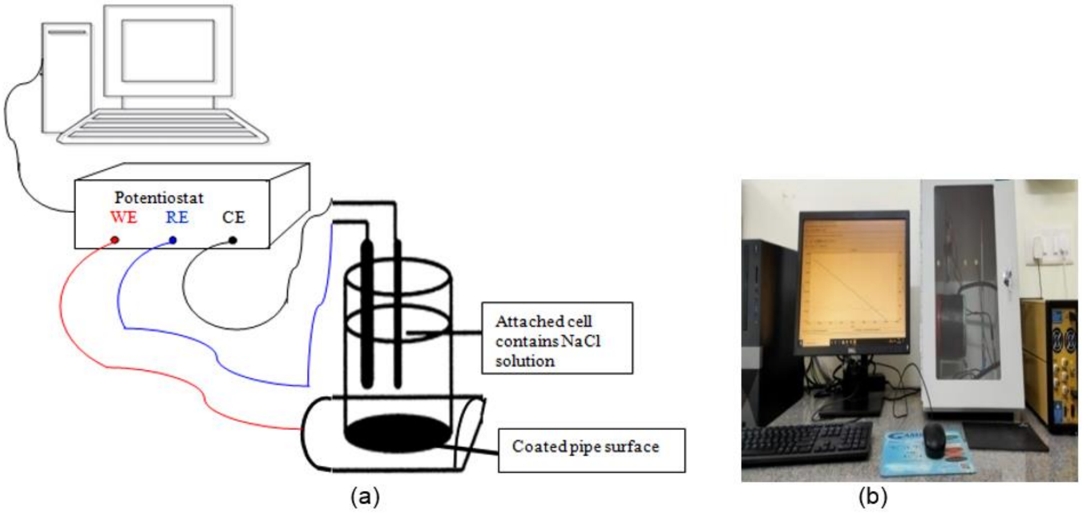

(a) (b)

Figure 5: (a) Schematic diagram of EIS test and (b) A coated sample under EIS testing.

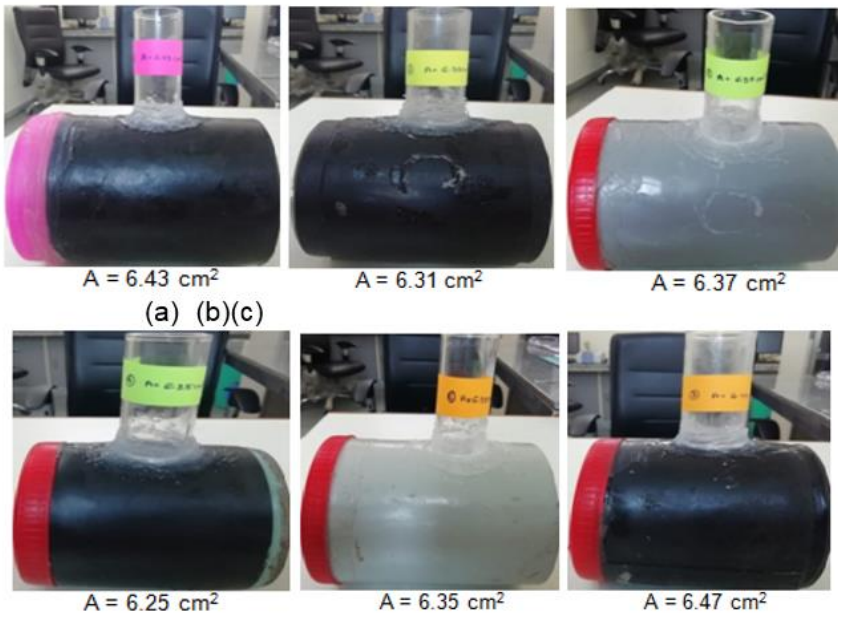

Figure 6: Coated test samples–(a) 3LPE, (b) 3p/2p CAT,(c) PU, (d) VE and (e) LE, (f) HSS (A=attached cell area in cm^2).

3. Results and Discussion

3.1 Chemical composition analysis and corrosion tests results of SS316L material

The results of the chemical composition analysis and corrosion tests of SS316L are reported in Table 1 and Table 2, respectively. The cyclic potentiodynamic polarization plots of test samples are shown in Figure 7.

The chemical composition analysis of SS316L conforms to ASTM Standard Specification A312 [26]. It is observed from the cyclic potentiodynamic polarization plots that the current increases steeply to $E_{PIT,}$ which indicates the onset of stable pits formation from the transient metastable pitting. From $E_{PIT,}$ the current increases sharply, indicating the transition to transpassive corrosion, a state of rapid dissolution of metal resulting in significant pitting corrosion, and the destruction of protective Cr_2O_3 passive film on the SS316L surface in the presence of Cl^- ions. Significant pitting corrosion has been observed under Scanning Electron Microscopy (SEM) examination after the cyclic potentiodynamic polarization test, as shown in Figure 8. CPTs have been found to be 15-16 °C, which indicates that SS316L is susceptible to localized pitting corrosion in chloride-bearing environments much below room temperature.

Table 1: Chemical composition analysis of SS316L.

Test Sample	C %	Mn%	S %	P %	Si %	Cr %	Ni %	Mo%	N (ppm)*	Fe %
Sample 1	0.021	1.24	0.005	0.042	0.26	16.32	10.05	2.03	380	Bal.
Sample 2	0.022	1.25	0.004	0.043	0.27	16.08	10.06	2.03	395	Bal.
Sample 3	0.018	1.27	0.004	0.043	0.20	16.29	10.05	2.04	440	Bal.

(ppm)* - parts per million Bal. - balance amount

Table 2: Corrosion test results of SS316L.

Test Sample	E_{PIT} (mV) vs. SCE *	CPT (^{0}C)	Mass loss corrosion rate (g/cm^2)
Sample 1	361	16	0.02071
Sample 2	363	15	0.02598
Sample 3	380	16	0.01519

SCE * - saturated calomel electrode as the reference electrode

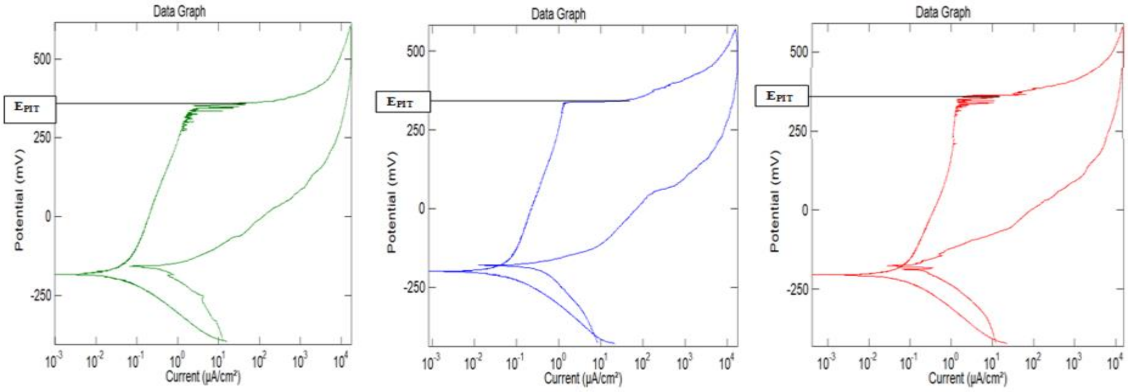

Figure 7: Cyclic potentiodynamic polarization plots of SS316L test samples.

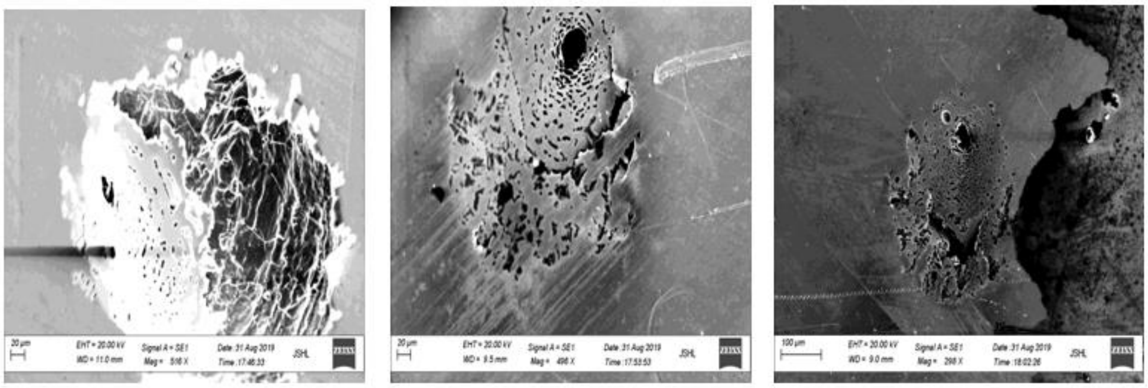

Figure 8: SEM photographs on pitting corrosion of SS316L samples after polarization test.

3.2. Thickness measurements and holiday tests results of coatings

The thickness measurement report and the applied voltages for holiday tests are shown in Table 3.

3.3. SEIR test results

SEIR values of the coatings are shown in Figure 9. From these graphs, the initial SEIR values of 3LPE, PU, and LE coatings are found to be greater than 10^9 ohm.m^2, whereas SEIR values of 3p/2p CAT, VE, and HSS are found to be greater than 10^8 ohm.m^2. Six coatings with such high initial specific electrical resistances reveal perfect insulators that yield higher corrosion protection. After 100 days of immersion, SEIR values of coatings are found to be reduced. This phenomenon is likely to happen due to exposure of a coating to a corrosive environment over some time and due to water absorption by the polymeric coating on metal substrate resulting in loss of insulating properties and corrosion protection efficiency.

To differentiate the performances of six types of coatings, a comparison has been drawn based on the SEIR values versus 100 days of immersion in 0.1mol/liter of NaCl solution (0.58 % NaCl solution) at 23-25 °C and is shown in Figure 10. It appears from Figure 10 that PU has the highest SEIR value. In comparison with other coatings, PU has better-insulating resistance than 3LPE, and 3LPE has better resistance than LE. VE has shown better resistance than 3p/2p CAT and HSS. Therefore, the ranking of six types of coatings concerning their performance in SEIR testing is found to be PU-1, 3LPE-2, LE-3, VE-4, 3p/2p CAT-5, and HSS-6, where '1' represents the highest performance.

Table 3: Thickness Measurement (in mm) and Holiday Test (in KV) of coatings.

Type of coating	1	2	3	4	5	6	7	8	Av.*	Vol.**	Holidays
3LPE	2.96	2.93	2.89	2.93	2.98	2.86	2.85	2.80	2.9	20	Nil
3p/2p CAT	2.48	2.52	2.55	2.49	2.51	2.52	2.45	2.48	2.5	19	Nil
PU	1.7	1.65	1.49	1.5	1.48	1.57	1.58	1.43	1.55	8	Nil
VE	3.03	3.09	3.07	2.95	2.91	3.03	2.89	3.1	3.0	22	Nil
LE	0.96	1.06	0.92	0.97	0.92	0.9	0.92	0.95	0.95	5	Nil
HSS	2.31	2.22	2.45	2.3	2.46	2.24	2.2	2.22	2.3	18	Nil

Av.* - arithmetic mean of thickness **Vol.**** - minimum applied voltage

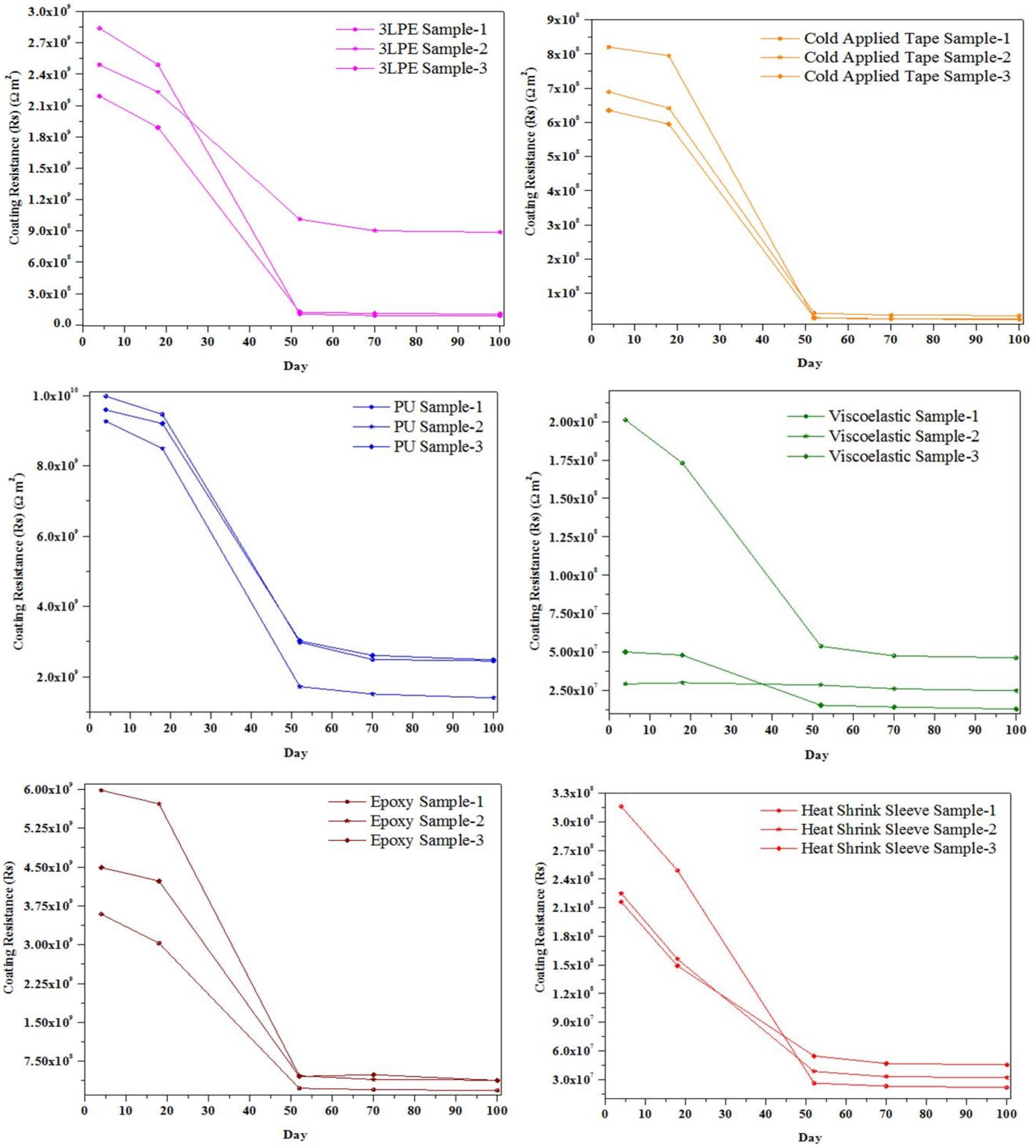

Figure 9: SEIR values of six coatings.

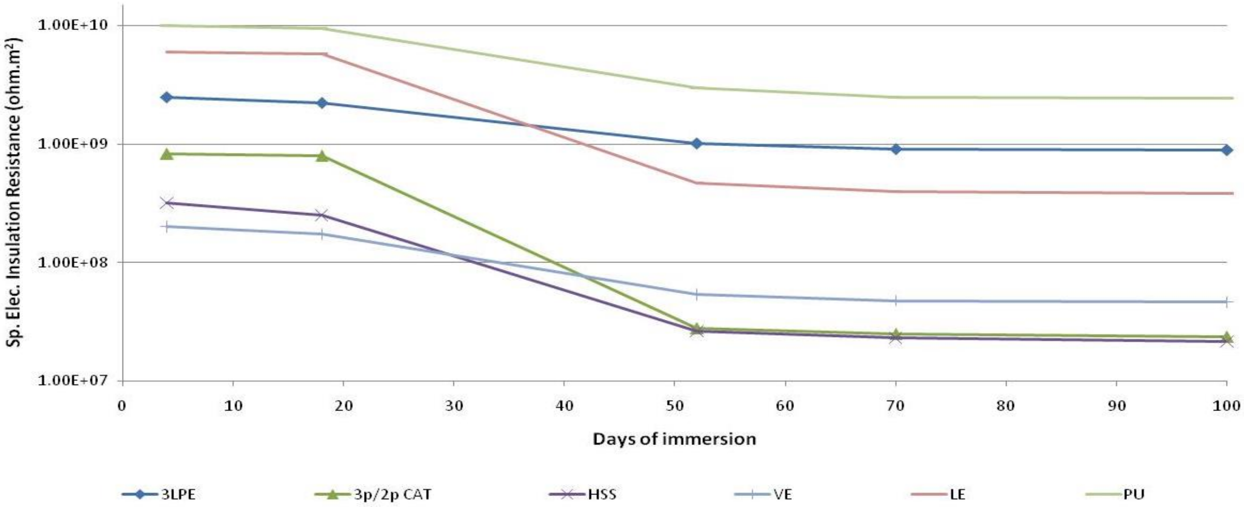

Figure 10: A comparison of SEIR values of six coatings for 100 days of immersion in 0.1mol/liter of NaCl solution at 23-25 °C.

3.4. EIS tests results

The Bode plots represent the data and spectra generated during EIS tests. These plots are interpreted as impedance magnitudes, |Z| in ohm.cm^2 (left side Y1 vertical axis in log scale) and phase angles, Φ in degree (right side Y2 vertical axis) versus the measured frequencies in Hertz (Hz) (horizontal X axis in log scale). A common legend has been used for the Bode plots of six types of coatings and is shown in Figure 11. The Bode plots of six types of coatings are shown in Figure 12 and Figure 13.

It is observed from the Bode plots of six types of coatings that the impedance values versus frequencies are diagonal, and their slopes are -1 [27]. Six types of coatings have shown high impedance values at the lowest frequencies, which are greater than 10^{11} ohm.cm^2, although little variations in impedance values have been observed for HSS, VE, and LE. The impedance values of six coatings types are also greater than 10^5 ohm.cm^2 at higher frequencies. Overall, six types of coatings are found to be good insulators.

Phase angles of 3LPE and 3p/2p CAT versus frequencies are found to be almost – 90 ° and a little less than – 90 °, respectively. It has been revealed that 3LPE and 3p/2p CAT behave as better capacitors. The variations of phase angles at lower frequencies have been observed on PU, VE, LE, and HSS coatings, and the phenomena indicate that there is a likelihood of permeating water, oxygen, ions, and corrosive species through the coatings into the metal substrates beneath due to exposure to the corrosive environments over some time and the coatings may lose insulating properties. Water causes swelling by transporting ions into the coating. When water uptake is low, the coating resistance is high because of low permeation of oxygen, ions, and corrosive species. It has been reported that diffusion is a prime mechanism of water absorption in polymeric coating and plays a significant role on water uptake. One of the studies conducted by EIS on polymeric coating has reported that there are four different stages for water uptake by the coating and they are (1) water absorption rapidly in the initial days, (2) increased water uptake with a slower rate, (3) saturation of water, and (4) lastly, a further increase in water absorption [28].

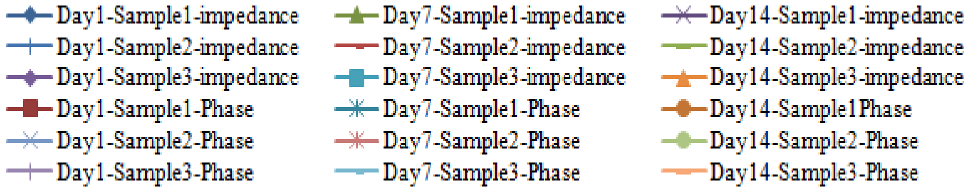

Figure 11: Common legend for the Bode plots of six coatings

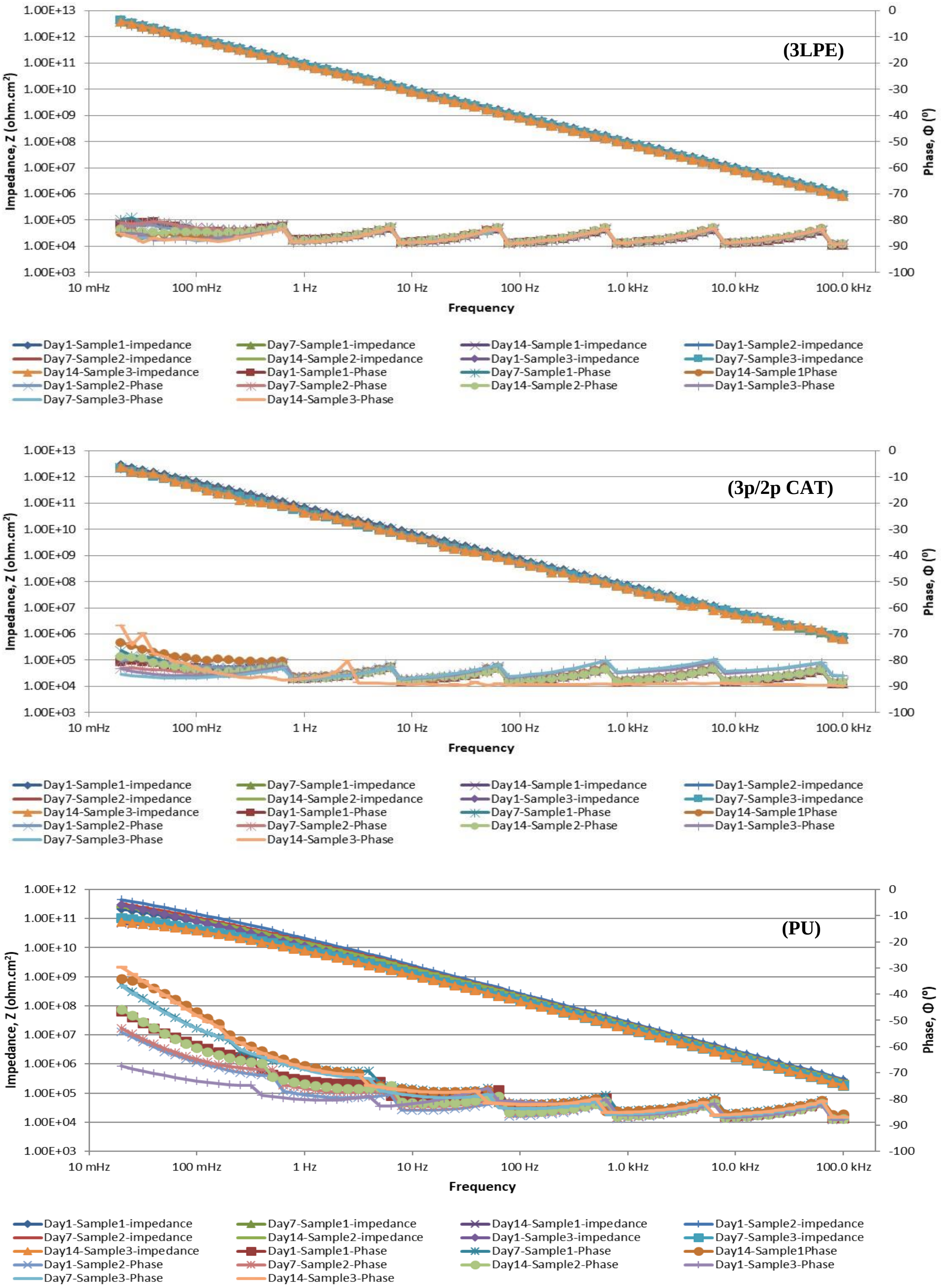

Figure 12: Bode plots of 3LPE, 3p/2p CAT and PU.

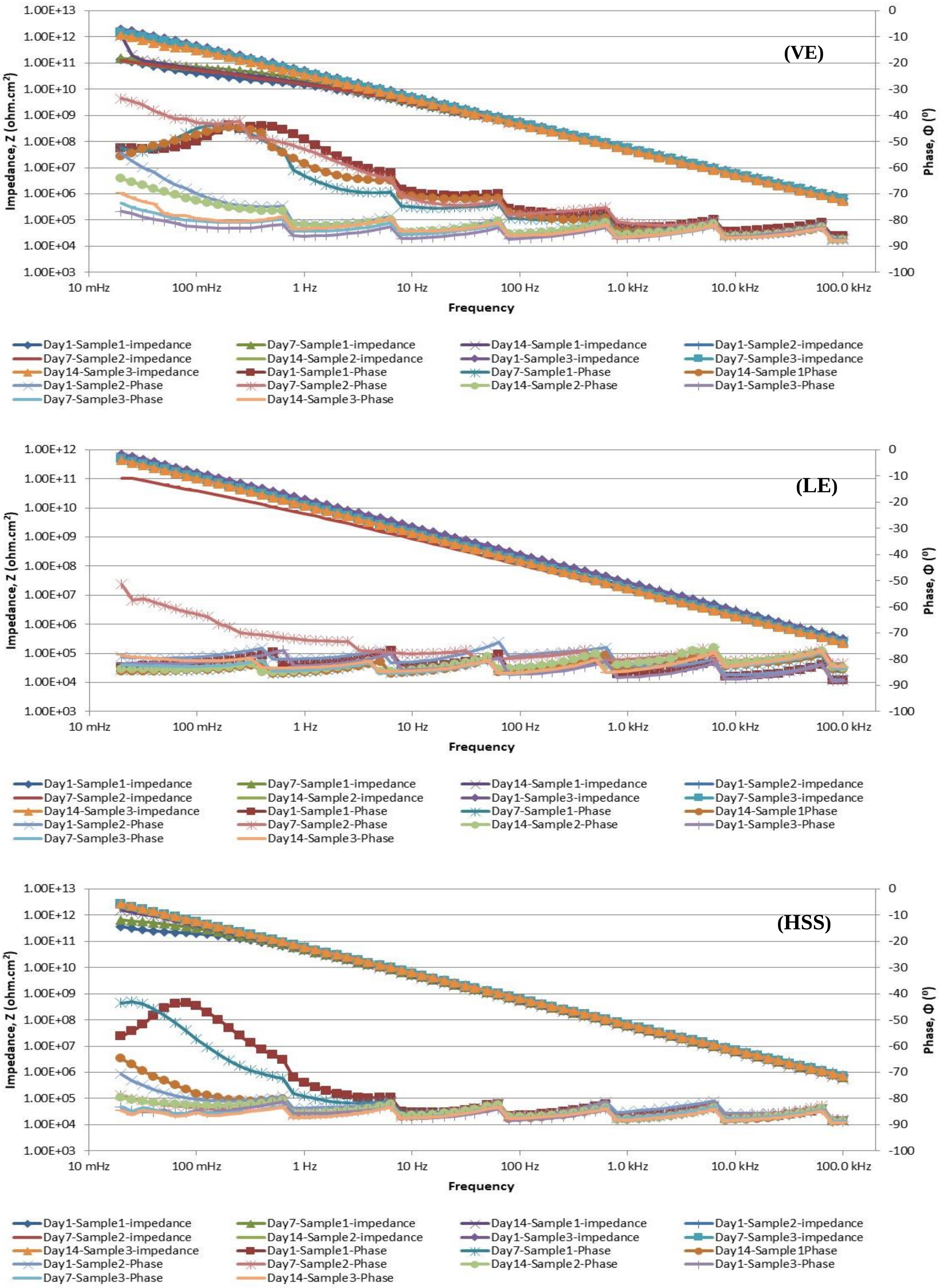

Figure 13: Bode plots of VE, LE and HSS

To distinguish the performances of six types of coatings, a comparison has been drawn based on the impedance values concerning cell areas of 1 cm^2 with an applied AC voltage of 100 mV$_{rms}$ in amplitude at a frequency of 100 mHz (0.1 Hz) versus 14 days of immersion in 3.5 % NaCl solution at 23-25 °C [29] and is shown in Figure 14**.** It is apparent from Figure 14 that 3LPE has the highest impedance value. Compared with other coatings, 3LPE has shown better impedance properties than 3p/2p CAT, which is better than HSS. Therefore, the ranking of six types of coatings concerning their performances in EIS testing is found to be 3LPE-1, 3p/2p CAT-2, HSS-3, VE-4, LE-5, and PU-6, where '1' represents the highest performance.

EIS results usually demonstrate that for the same coating type, the coating impedance increases with increasing coating thickness [30]. But, in this study when a comparison of coatings performances has been made, a linear. Relationship between coating impedance and coating thickness is not observed.

The ranking of the coatings from SEIR and EIS tests have been analyzed to determine an overall ranking, as shown in Table 4.

If the overall ranking is compared to the suitability of use, where the coating performs well in both SEIR and EIS tests, 3LPE is best suited for buried SS316L pipelines.

There may be two opinions for the second best coating, where the suitability factor is the same for 3p/2p CAT and PU. Some industries give more importance to EIS over SEIR because EIS measures impedance and capacitance quantitatively and provides information on the electrochemical and corrosion processes of the coating and metal substrate beneath

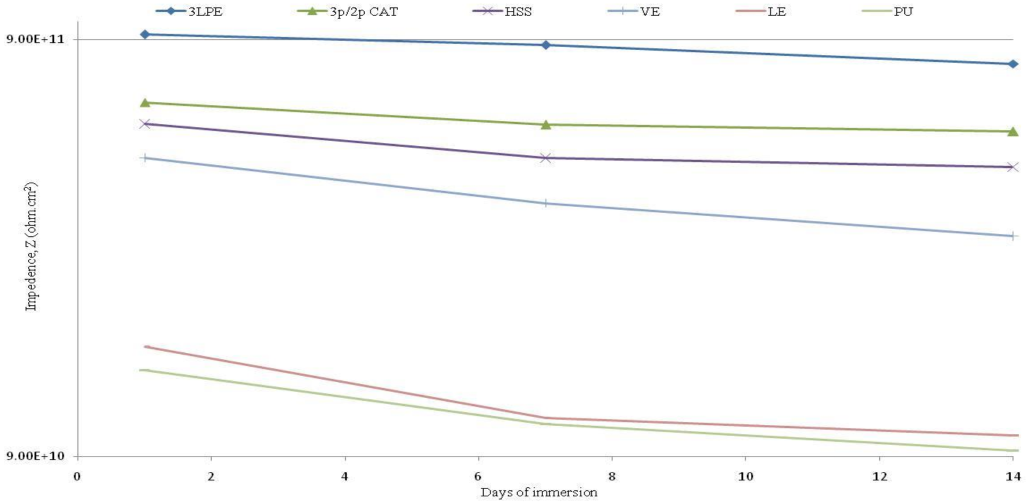

Figure14: A comparison of impedance values of six coatings with respect to cell areas of 1 cm^2 with an applied AC voltage of 100 mVrms at 100 mHz for 14 days of immersion in 3.5 % NaCl solution at 23-25 °C.

Table 4: Overall ranking of six coatings.

Type of coating	Order of ranking		Suitability factor (arithmeticmean of standing)	Overall ranking (Note-A)
	SEIR test	EIS test		
3LPE	2	1	1.5	1
3p/2p CAT	5	2	3.5	2(Note-B)
PU	1	6	3.5	2 (Note-B)
VE	4	4	4.0	4(Note-B)
LE	3	5	4.0	4(Note-B)
HSS	6	3	4.5	6

Note-A: overall ranking “1” represents the highest performance
Note-B: overall ranking in preference to either the EIS test or SEIR test

the coating for pipelines buried in soil or submerged in water. For them, 3p/2p CAT is ranked second, and PU is third. Some other industries prefer to SEIR over EIS because SEIR measures quantitatively the net specific electrical insulation resistance of the coating for pipelines buried in soil or submerged in water. PU is ranked second for them, and 3p/2p CAT is third.

In line with the above reasoning behind 3p/2p CAT and PU, the overall ranking of VE and LE coatings are found to be either fourth or fifth, with the same suitability factor. Lastly, HSS is found to be in the sixth rank.

4. Conclusions

The experimental data collected from SEIR and EIS tests have been evaluated for the suitability of the coating for buried SS316L pipelines. It appears that 3LPE is best suited among the coatings. Other coatings used in the petroleum, petrochemical, and natural gas industries differ in opinion. Some industries prefer EIS over SEIR because EIS measures impedance and capacitance quantitatively and provides information on the electrochemical and corrosion processes of the coating and metal substrate beneath the coating. According to EIS, 3p/2p CAT is better than PU. Some other industries prefer SEIR over EIS because of the simplicity of the SEIR test, and the data collected from the SEIR test are easy to interpret the electrical insulation resistance properties of the coating. Under SEIR, PU is better than 3p/2p CAT. In brief, the present study has revealed that 3LPE is the best coating, and barring 3LPE, 3p/2p CAT & PU are better coatings for buried SS316L pipelines in the petroleum, petrochemical, and natural gas industries.

Acknowledgments

The authors gratefully acknowledge the cooperation and assistance of the Gujarat Industrial Research and Development Agency (GIRDA), Seal for Life, and Jindal Stainless Steel Laboratories in providing access to testing facilities and data. It is also acknowledged the guidance and great help provided by K.B.Singh & Associates to timely conduct all testings

5. References

1. Lawrence J. Korb and David L. Olson, ASM Handbook, Vol. No.13, Corrosion, ASM International, Ohio, USA, 1992, 3020.
2. C.-O.A. Olsson, D. Landolt, Passive films on stainless steels-chemistry, structure and growth, *Electrochimica Acta*, 4(2003), 1093.
3. Guidelines for use of stainless steel in the ground, Technical FAQ No.7, Australian Stainless Steel Development Association (ASSDA).
4. L. Sjögren, G. Camitz, J. Peultier, S. Jacques, V. Baudu, F. Barrau, B. Chareyre,A. Bergquist, A. Pourbaix, P. Carpentiers, Corrosion resistance of stainless steel pipes in soil, *European Commission, Technical Steel research*, Final report (2008), 15.
5. A. John Sedriks, Corrosion of Stainless Steels, Chapter 4, John Wiley & Sons, Inc., Hoboken New Jersey, Second Edition, 1996, 102.
6. D.A.Jones, Principles and Prevention of Corrosion, Chapter 7, Macmillan Publishing Company, New York, 1996, 198.
7. Stephen D. Cramer and Bernard S. Covino, Jr., ASM Handbook, Vol. No.13B, Corrosion: Materials, ASM International, Ohio, USA, 2005, 62.
8. Robert G. Kelly, John R. Scully, David W. Shoesmith, and Rudolph G. Buchheit, Electrochemical Techniques in Corrosion Science and Engineering, Chapter 3, Marcel Dekker, Inc. New York, 2003, 104-107.
9. Standard test method for conducting cyclic potentiodynamicpolarization measurements for localized corrosion susceptibility of Iron-, Nickel-, or Cobalt-based alloys, Annual Book of ASTM Standard, ASTM Standard, G61, 2003.
10. Gill AC Potentiostat with 5 channels, ACM Instruments, the Silver Works, Aynsome Lane, Cartmel, Grange-Over-Sands, Cumbria, LA11 6HH, United Kingdom.
11. Carl Zeiss SEM Model No. EVO 40, Carl Zeiss AG, Oberkochen, Baden-Württemberg Germany.
12. Standard test methods for pitting and crevice corrosion resistance of stainless steels and related alloys by use of ferric chloride solution, Annual Book of ASTM Standard, ASTM Standard, G48, 2003.
13. Paint coating stainless steels, British Stainless Steel Association (BSSA), 2018.
14. International Standard ISO 21809-1, “Petroleum and natural gas industries - External coatings for buried or submerged pipelines used in pipeline transportation systems-Part 1: Polyolefin coatings (3-layer PE and 3-layer PP)”.
15. Petroleum and natural gas industries - external coatings for buried or submerged pipelines used in pipeline transportation systems-Part 3: Field joint coatings, the International Organization for Standardization, International Standard, 21809, 2016.

16. DeFelsko digital thickness gauge, Model No. PosiTector 6000, DeFelsko Corporation, 800 Proctor Avenue, Ogdenburg, NY 13669-2205, USA.
17. Holiday detectors, Model Nos. DC-05 and SD-120, Associate Electronics, 322, Vraj Siddhi Tower, Market Char Rasta, Rajmahal Road, Vadodara-390 001, India.
18. High-voltage electrical inspection of pipeline coatings, NACE International, NACE Standard, SP0274, 2011.
19. Caltech specific electrical insulation resistance tester, Model No. SISR-05, Caltech Engineering Services, D-104, Twin Arcade, Marol, Andheri East, Mumbai-400059, India.
20. Evgenij Barsoukov, J. Ross Macdonald, Impedance Spectroscopy - Theory, Experiment, and Applications, Chapter 4, John Wiley & Sons, Inc., Hoboken New Jersey, Second Edition, 2005, 419.
21. Bobbi Jo Merten, Coating evaluation by electrochemical impedance spectroscopy (eis), Materials and Corrosion Laboratory, U.S. Department of the Interior, Bureau of Reclamation, December 2015.
22. F. Mansfeld and C.H. Tsai, Determination of coating deterioration with EIS. I. Basic relationships, *Corrosion* 47 (12) (1991), 958–963.
23. M. Mirzaee, M. Rezaei Abadchi, A. Fateh, A. Zolriasatein, Investigation of corrosion properties of modified epoxy and polyurethane organic coating on steel substrate, *Prog. Color Colorants Coat.*, 15 (2022), 25-36.
24. Standard practice for verification of algorithm and equipment for electrochemical impedance measurements, Annual Book of ASTM Standard, ASTM Standard, G106, 2003.
25. GAMRY Reference 600+, GAMRY Instruments, 734 Louis Drive, Warminister, PA 18974.
26. Standard specification for seamless, welded, and heavily cold worked austenitic stainless steel pipes, Annual Book of ASTM Standard, ASTM Standard, A312, 2009
27. E. Akbarinezhad, M. Bahremandi, H.R. Faridi, F. Rezaei, Another approach for ranking and evaluating organic paint coatings via electrochemical impedance spectroscopy, *Corrosion Sci.*, 51(2009), 356-363.
28. F. Dolatzadeh, S. Moradian, M. M. Jalili, Effect of nano silica on moisture absorption of polyurethane clear coats as studied by EIS and gravimetric methods, *Prog. Color Colorants Coat.*, 3(2010), 92-100.
29. Linda G.S. Gray, Bernard R. Appleman, A tool to predict remaining coating life? *JPCL*, 2(2003).
30. Ken Holyoake, Jiangnan Yuan, Electrochemical impedance spectroscopy measurements of barrier coatings, ARMATEC Environmental Ltd, 05(1999).

How to cite this article:
S. Ghosal, R. Dey, B. Duari, Evaluation of Coatings Suitability for Buried SS316L Pipelines. Prog. Color Colorants Coat., 16 (2023), 361-375.

PROGRESS
IN COLOR, COLORANTS AND COATINGS

available online @ www.pccc.icrc.ac.ir
Progress in Color Colorants Coating 16 (2023), 377-385

Ministry of Science, Research and Technology
Institute for Color Science & Technology

Performance of Thermophilic Aerobic Membrane Reactor (TAMR) for Carpet Cleaning Wastewater

Kh. R. Kalash*, M. H. Al-Furaiji, A. R. Alazraqi
Environment and Water Directorate, Ministry of Science and Technology, P.O. Box: 20392, Baghdad, Iraq

ARTICLE INFO

Article history:
Received: 30 Jan 2023
Final Revised: 04 June 2023
Accepted: 06 June 2023
Available online: 03 Sep 2023

Keywords:
Anionic surfactants
Wastewater
Thermophilic
Carpet cleaning wastewater
Methylene blue

ABSTRACT

Managing sewage has become increasingly important at both the national and international levels, largely due to uncertain future options for recovery and disposal. Due to this, it is necessary to develop innovative technology that can reduce pollutants such as surfactants to mitigate the problem at its source. Surfactants are the kind of pollutants that can pose health and environmental risks. This paper aims to study the efficiency of the removal of methylene blue active substances as an anionic surfactant (MBAS) and chemical oxygen demand (COD) from carpet cleaning wastewater using a thermophilic aerobic membrane reactor (TAMR). A laboratory-scale reactor was monitored daily for a month during this study. The removal efficiencies of MBAS and COD were 92 and 95 %, respectively. This study demonstrated that the TAMR process could resist high-stress situations (sudden load peaks) and withstand high surfactant concentrations, making it the ideal pretreatment option. For MBAS removal, the TAR and UF processes combined led to higher removal yields. MBAS was removed almost completely (>92 %) by the TAMR+UF procedure. Moreover, membrane cleaning operations and fouling problems are discussed. Prog. Color Colorants Coat. 16 (2023), 377-385© Institute for Color Science and Technology.

1. Introduction

Chemicals such as dyes, metals, and antibiotic drugs are commonly found in wastewater [1]. These chemicals are known to enter the environment through wastewater and cause profound effects on the environment [2]. While it is widely known that certain chemicals in water are beneficial, they can also threaten human health [3]. Wastewater from washing industries such as laundry, carpet cleaning, and car washing offers combinations of different levels, including suspended solids, turbidity, chemical oxygen demand (COD), and surfactants. In most communities and carpet cleaning situations, wastewater can be discharged by pouring it into a sink, toilet, bathtub, or other drainage systems as long as it is connected to the municipal sewer infrastructure.

For instance, certain surfactants in high concentrations can cause adverse effects on humans [4]. A surfactant is a substance that has a unique structure that contains both hydrophilic and hydrophobic moieties [5]. It can be used in various industries, such as cleaning and textiles. The cationic surfactants are positively charged, anionic surfactants are negatively charged, and non-ionic surfactants have a non-ionized hydrophilic group [3]. Each type of surfactant is produced differently. For instance, the total production of cationic surfactants is only 10 %. The production of different kinds of surfactants is not the same. For example, the total output of MBAS is 60 %, while the production of

---

*Corresponding author: * khairirs@gmail.com
Doi: 10.30509/pccc.2023.167094.1201

TAS is 30 % [6]. Due to environmental protection regulations, the use of surfactants has been regulated in many consumer products [7]. However, these chemicals' excessive production and discharge into the environment have continued [8]. Due to the continuous use of surfactants, the environment is still vulnerable to toxicity. Therefore, removing these harmful substances could be challenging [6]. These industrial laundries are mainly responsible for producing wastewater produced by various levels of suspended solids with varying turbidity and COD [9]. The main problem is the removal of dirt from the fabrics [10].

The removal of surfactants involves chemical and electrochemical processes [11], photocatalytic degradation, membrane technology and chemical precipitation [12], adsorption [13], and various biological methods [14]. There are merits and limitations to each approach. Wastewaters containing surfactants are challenging to treat by biological processes, such as activated sludge, because of low degradation kinetics and foam production [15]. Although chemical and physic-chemical treatments are generally considered effective in removing surfactants, they can also cause high operating costs [10]. For illustration, high surfactant concentration can lead to the depletion of adsorbent materials. Biological processes could provide an alternative to conventional waste disposal methods [6, 8, 16]. However, their disadvantages are usually considered when compared to the alternatives.

A thermophilic aerobic membrane reactor (TAMR) was tested in this study to overcome this disadvantage. Thermophilic treatments show low sludge production (0.02-0.1 kgVSS /kgCOD removed). In contrast to mesophilic conditions, WW treatment plants can reduce their total costs by 50 percent due to sludge management costs [17]. Reduced sludge production may be due to increased metabolic activities at higher temperatures rather than reproduction and growth or increased endogenous respiration, which means bacteria consume more COD for maintenance than cellular growth [17]. Furthermore, their biodegradable substrate removal kinetics is around 3-10 times greater than those under mesophilic conditions [18]. By using a UF membrane in conjunction with a thermophilic aerobic reactor (TAR), the biomass is retained at high concentrations (up to 190 kg TSS m^{-3}) of total suspended solids (TSS). This concentration can be handled, thus reducing the size of the reactor [1].

The study was conducted on a bench-scale wastewater reactor with TAR+ ultrafiltration (UF). The reactor was monitored for over one month by using real wastewater has been characterized. Moreover, information on membrane cleaning operations and fouling problems is obtainable. The current study aimed to study and reveal that TAMR may be utilized as a pretreatment to reduce the concentration of MBAS and takes advantage of its stability by using UF for polishing.

2. Experimental

2.1. Carpet cleaning wastewater

The wastewater samples were collected from a carpet cleaning plant in Al Najaf, Iraq. The characterization of the wastewater used in our experimental study is given in Table 1.

Shakeri et al. [19] stated the wastewater characteristics from hospital laundry as surfactant and COD ranged between 3.19-6.48 mg/L and 650-1,080 mg/L, respectively. Changani et al. [6] also detected that the wastewater from the carpet cleaning industry's average effluent characteristics was a detergent of 55.51 mg/L and COD of 367.4 mg/L. Furthermore, MBAS, COD, turbidity, electrical conductivity, and pH were detected as353-25 mg/L, 229-1446 mg/L, 137-2250 NTU, 250-1,890 µs/cm, and 7.7-8.2, respectively, of wastewater from car wash station [20]. Table 1 shows concentrations of all contaminants measured in the current study were within the range stated in the significant literature and relevant. The effluent analyses were performed on a sample withdrawn from the supernatant. COD was analyzed using a digestion reactor (LT200, Hach, USA) and spectrophotometer (DR 5000 UV-Vis, Hach, Germany). Water and

Table 1: The characterization of the wastewater used in the experimental study.

Parameter	Unit	Concentration
COD	mg/L	499-650
Turbidity	NTU	100-133
MBAS	mg/L	17.8-20.2
Conductivity	mS/m	0.77-0.88
pH	-	8.5-9.1

Wastewater Standard Methods have been used to quantify COD in raw influent WW (APHA, 2012) [21]. MBAS was measured with a spectrophotometer (DR 3900 UV-Vis, Hach, Germany) according to the method suggested by Chitikela et al. [22]. The nephelometric method [21] was used to analyze turbidity using a spectrophotometer (2100 AN, Hach, Germany). The MBAS, COD, and turbidites removal efficiency (R) (%) was calculated using the formula shown in Eq. 1. The MBAS content was determined after filtration with UF membranes. Other parameters were determined for effluent as obtained.

$$\text{Surfactants removal }(\%)=\frac{C_{in}-C_{out}}{C_{in}}\times 100 \qquad (1)$$

Where C_{in} and C_{out} are the concentration of Influent and Effluent wastewater.

A pH meter and thermometer (model SenTix® 940, WTW-IDS) were used in the TAMR reactor for simultaneous pH and temperature measurement. A probe model TetraCon® 925 was used to measure electrical conductivity.

2.2. Bioreactor configuration

Aerobic conditions were imposed upon the TAMR bioreactor made of Plexiglas and having a volume of 10 L. There were two sampling ports on the reactor body, each at a different height, as shown in the schematic diagram Figure 1). There were two main sections in this apparatus: the main one was where wastewater and activated sludge met, and the second section was where UF membranes were sited. A compressor, air diffuser, and O2 from the oxygen cylinder provided aeration from the bottom of the column. A peristaltic pump was used to pump continuous wastewater into the system from the feed tank. The treated wastewater was also discharged from the upper part of the reactor into UF membranes. At different temperatures, the lab-scale bioreactor was operated with a programmable logic controller for different cycle times: 30 minutes for aeration, 10 minutes for settling, and 2 minutes for effluent withdrawal.

3. Results and Discussion

3.1. Characterization of the wastewater

Although the characteristics of carpet cleaning wastewater can vary, the variation can be observed due to the various procedures utilized. The carpet-cleaning wastewater influent was treated with a pilot-scale treatment system. The results revealed that the high concentration of multiple surfactants and COD allowed the wastewater to achieve high electrical conductivity and pH. The results showed that the conductivity reported between 0.77-0.88 and pH was 8.5–9.1, respectively, as shown in Table 1. The concentration of the surfactants was within the range obtained by literature reports. pH values were lower than those seen in other tests as well. WW had the same electrical conductivity as Collivignarelli et al. [23] but a higher one than Ciabattia et al. [24].

3.2. The overall removal efficiency of organic matter and surfactant wastes

The average output and input concentrations of COD were 100 and 561 mg/L. Removal efficiency for COD was estimated between 70.55-94.99 %. Figure 3 shows that the process stability is still good despite the increase in COD value. A high level of process and quality stability was also observed during the experiments.

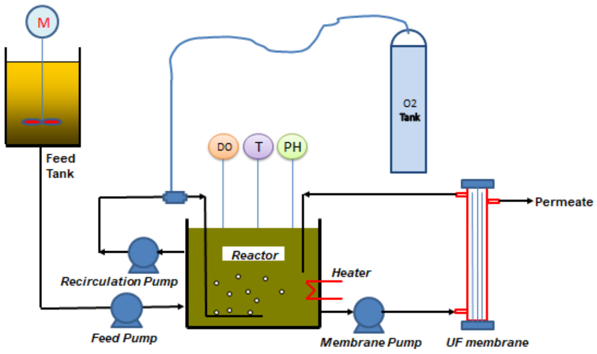

Figure 1: Experimental setup of TAMR**.**

Figure 2: The TAMR beanch scale.

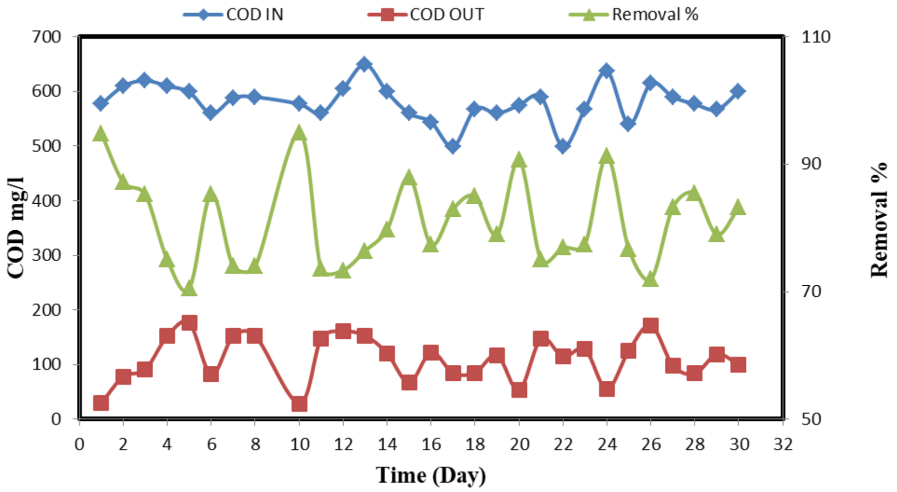

Figure 3: Concentrations of COD input and output and removal efficiency.

Figure 4 shows concentrations of anionic surfactants (MBAS). The MBAS average removal efficiencies were between 70.1 and 90.1 %, respectively, so the effluent concentration was between 1.465 and 5.44 mg/L. Despite high COD and MBAS, the TAMR process performed exceptionally well with 94.99 and 90.1% removal yields for COD and MBAS, respectively.

The TMAR reactor is an effective and valid process for removing MBAS and is the novelty of this research. There is a great deal of variability in the data obtained in this study compared to some provided by the literature. In our test, the removal efficiency of surfactant concentration was 90.1 %, which agrees with that reported by Collivignarelli et al. [23, 25, 26] but significantly higher than that reported by Ciabattia et al. [24] and one order of magnitude higher than Ostar-Turk et al. [27] even COD removal.

Figure 5 shows concentrations of biological oxygen demand (BOD). The BOD average removal efficiencies were 82 and 94 %, respectively, so the effluent concentration was consistently between 34 and 14 mg/L. Even with high BOD, the TAMR process performed exceptionally well with a 94.99 % removal yield for BOD.

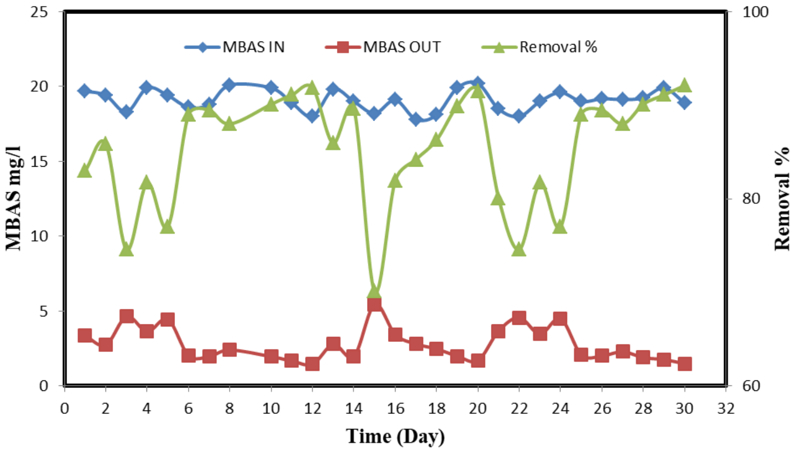

Figure 4: MBAS concentrations and removal yields of the TAMR experiment.

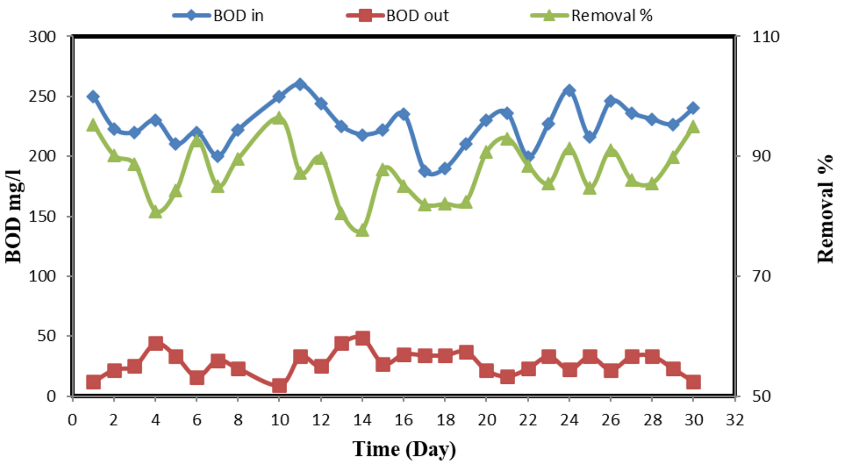

Figure 5: Concentrations of BOD input and output and removal efficiency.

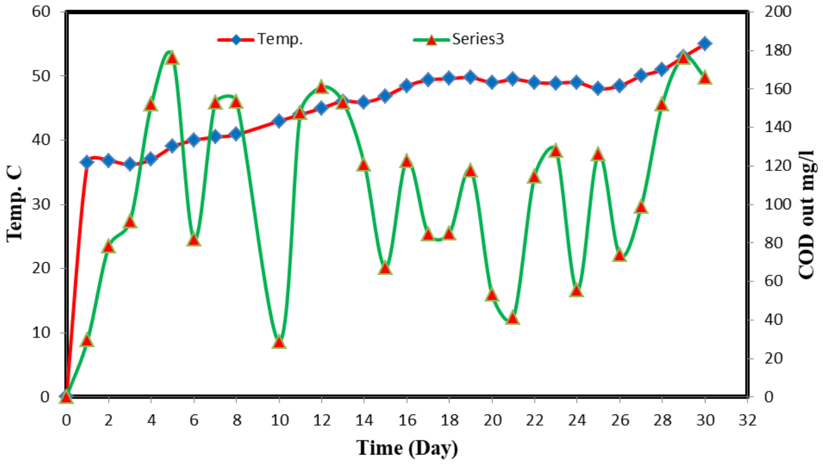

Figure 6: Effect of temp. on COD concentration.

3.3. The effect of temperature on performance removal of COD and surfactant wastes

The experimental performance improved over time due to installing a heater for temperature control (between 45 and 48 °C). When the temperature is higher than 50°C, COD removal yields are significantly reduced, as shown in (Figures 6 and 7). The high removal rate of biodegradable substrates (up to 10 times higher than those measured in mesophilic conditions [28], is mainly due to the fast hydrolysis of the organic substance at thermophilic temperature. That allows substrate solubilization and its availability for oxidation.

3.4. UF investigations during experimental setup

3.4.1. NTU investigations

Turbidity rejection was not disturbed in all cases and always maintained ≥98-99 %, as shown in Figure 8.

3.4.2. Flux investigations for short term

The correlation of flux decline with time was conducted to obtain preliminary information about the fouling tendency of the membrane. The behavior of the permeate flux as a function of the operation time was studied quickly. Figure 9 shows that the UF permeate flux appears very stable with the operating time, indicating that fouling is not a problem on the UF system during 150 min operation. During the UF, the temperature increased again (54±2 °C) due to the working conditions. Therefore, more favorable permeation rates can be achieved due to decreased viscosity [29]. Permeate flux was expressed as volume per unit membrane area per unit time, e.g., Lm^{-2} h^{-1} (LMH).

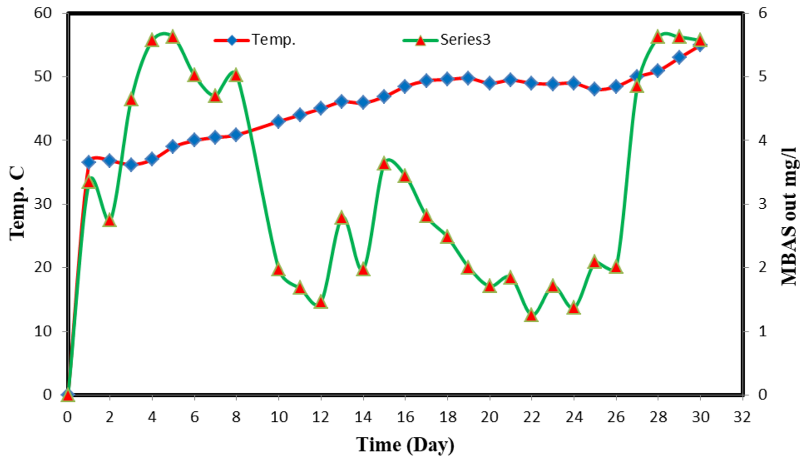

Figure 7: Effect of temp. on MBAS concentration.

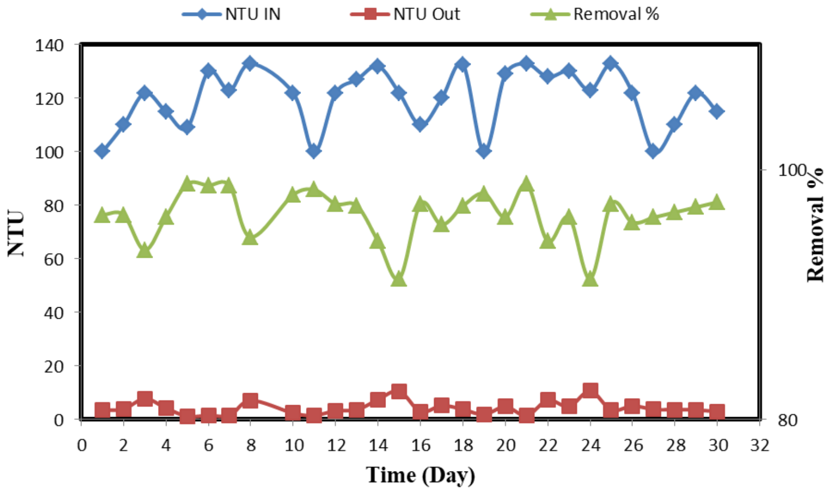

Figure 8: Concentrations of NTU input and output and removal efficiency.

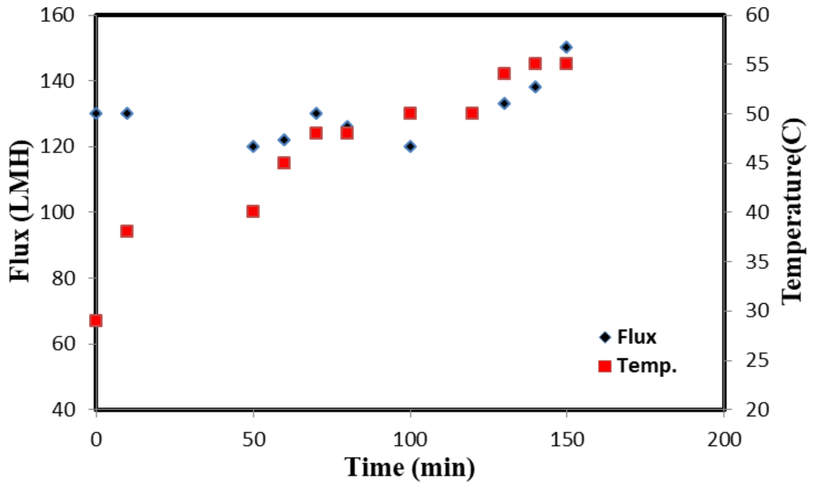

Figure 9: The behavior of the permeate flux as a function of the operation time and temperature.

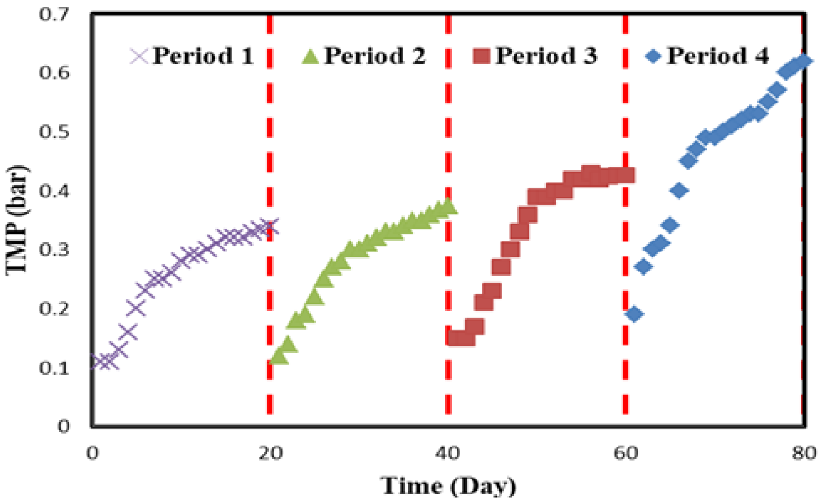

Figure 10: Transmembrane pressure (TMP) change in the UF process.

3.4.3. Membranes: fouling and cleaning for long term

As part of this study, the feed, retentate, and permeate pressures in the vessel were measured, father more transmembrane pressure was calculated as described in Eq. 2.:

$$\text{TMP (bar)}=\frac{P_F\text{-}P_R}{2}\text{-}P_P \qquad (2)$$

Whera P_F, P_R, and P_P represent the feed, retention, and permeate pressures.

Figure 10 shows that the transmembrane pressure increased significantly in the long term. It was observed that the membranes were being subjected to organic fouling and the presence of inorganic precipitates. The membrane cleaning was not different between the lines. The process consisted of four passages, and each was carried out at the highest temperature permitted by the membranes. pH levels are brought nearer to neutral by rinsing with demineralized water. The cleaning operations for the membranes were performed at various times. These tests revealed that the membranes did not exhibit organic fouling problems. Since cleaning the membranes is essential to reduce the formation of inorganic fouling, they are regularly washed at least once in a 60-minute operation.

4. Conclusions

The study results revealed that combining the TAMR+UF process can achieve an optimal removal of MBAS and COD was 92.15 to 95%, respectively, with a different OLR. The colored wastes did not cause inhibition of the thermophilic biomass; surfactants were removed up to efficiencies as high as 92.1 %, even at the highest OLR values. The plant was fully monitored for more than one month to confirm the presence of certain surfactants in the wastewater. The TAMR+UF combination has the potential to provide an excellent polishing treatment. Moreover, membrane cleaning operations and fouling problems are discussed.

Acknowledgments

The authors gratefully acknowledge the scientific support of the Environment and Water Directorate, Ministry of Science and Technology, Baghdad, Iraq.

5. References

1. G. Bertanza, M.C. Collivignarelli, B.M. Crotti, R. Pedrazzani, Integration between chemical oxidation and membrane thermophilic biological process, *Water Sci. Technol.* 61 (2010), 227-234.
2. C. Dumas, S. Perez, E. Paul, X. Lefebvre, Combined thermophilic aerobic process and conventional anaerobic digestion: Effect on sludge biodegradation and methane production, *Bioresour. Technol.*, 101 (2010), 2629-2636.

3. K. R. Kalash, M. Al-Furaiji, A. N. Ahmed, Kinetic Characteristics and the Performance of Up-Flow Biological Aerated Filters (UBAF) for Iraqi Municipal Wastewater, *Pollution*., 8 (2022), 621-636.
4. C. Ramprasad, L. Philip, Surfactants and personal care products removal in pilot scale horizontal and vertical flow constructed wetlands while treating greywater, *Chem. Eng*., 284 (2016), 458-468.
5. M. Lechuga, M. Fernández-Serrano, E. Jurado, J. Núñez-Olea, F. Ríos, Acute toxicity of anionic and non-ionic surfactants to aquatic organisms, *Ecotoxicol. Environ. Saf*., 125 (2016), 1-8.
6. T. Sharma, Impact of anionic surfactant on stability, viscoelastic moduli, and oil recovery of silica nanofluid in saline environment, *J. Pet. Sci. Eng*., (2020), 107634.
7. M. Palmer, H. Hatley, The role of surfactants in wastewater treatment: Impact, removal and future techniques: A critical review, *Water Res*., 147 (2018), 60-72.
8. European Commission, Regulamento n^{o}648/2004, *Off. J. Eur. Communities*., L 269 (2000), 1-15.
9. K. Jardak, P. Drogui, R. Daghrir, Surfactants in aquatic and terrestrial environment: occurrence, behavior, and treatment processes, *Environ. Sci. Pollut. Res*., 23 (2016), 3195-3216.
10. C. O. C. Nascimento, M. T. Veit, S. M. Palácio, G. C. Gonçalves, M. R. Fagundes-Klen, Combined application of coagulation/flocculation/sedimentation and membrane separation for the treatment of laundry wastewater, *Int. J. Chem. Eng*., 2019 (2019), 1-13.
11. S. Bering, J. Mazur, K. Tarnowski, M. Janus, S. Mozia, A.W. Morawski, The application of moving bed bio-reactor (MBBR) in commercial laundry wastewater treatment, *Sci. Total Environ.,* 627 (2018), 1638-1643.
12. M. Al-Furaiji, B. Waisi, K. Kalash, M. Kadhom, Effect of polymer substrate on the performance of thin-film composite nanofiltration membranes, *Int. J. Polym. Anal. Charact*., 27 (2022), 316-325.
13. N. S. Ali, K. R. Kalash, A. N. Ahmed, T. M. Albayati, Performance of a solar photocatalysis reactor as pretreatment for wastewater via UV, UV/TiO_2, and UV/H_2O_2 to control membrane fouling, *Sci. Rep*., 12(2022), 16782.
14. S. Mohsen Alardhi, J. M. Alrubaye, T. M. Albayati, Removal of methyl green dye from simulated waste water using hollow fiber ultrafiltration membrane, IOP *Conf. Ser. Mater. Sci. Eng*., 928(2020), 20-52.
15. S. T. Kadhum, G. Y. Alkindi, T. M. Albayati, Determination of chemical oxygen demand for phenolic compounds from oil refinery wastewater implementing different methods, *Desalin. WATER Treat*., 231(2021), 44-53.
16. H. J. Al-Jaaf, N. S. Ali, S. M. Alardhi, T. M. Albayati, Implementing of eggplant peels as an efficient bio-adsorbent for treatment of oily domestic wastewater, *Desalin. WATER Treat*., 245(2022), 226-237.
17. A. Abeynayaka, C. Visvanathan, Mesophilic and thermophilic aerobic batch biodegradation, utilization of carbon and nitrogen sources in high-strength wastewater, *Bioresour. Technol*., 102(2011), 2358-2366.
18. J. Duncan, A. Bokhary, P. Fatehi, F. Kong, H. Lin, B. Liao, Thermophilic membrane bioreactors: A review, *Bioresour. Technol*., 243(2017), 1180-1193.
19. H. U. Cho, S. K. Park, J. H. Ha, J. M. Park, An innovative sewage sludge reduction by using a combined mesophilic anaerobic and thermophilic aerobic process with thermal-alkaline treatment and sludge recirculation, *J. Environ. Manage*., 129(2013), 274-282.
20. E. Shakeri, M. Mousazadeh, H. Ahmadpari, I. Kabdasli, H. A. Jamali, N. S. Graça, M. M. Emamjomeh, Electrocoagulation-flotation treatment followed by sedimentation of carpet cleaning wastewater: optimization of key operating parameters via RSM-CCD, *Desalin. Water Treat*., 227(2021), 163-176.
21. M. M. Emamjomeh, H. A. Jamali, Z. Naghdali, M. Mousazadeh, Carwash wastewater treatment by the application of an environmentally friendly hybrid system: an experimental design approach, *Desalin. Water Treat*., 160 (2019), 171-177.
22. W. E. Federation, APHA, AWWA, WEF. Standard Methods for examination of water and wastewater, *An. Hidrol. Médica*., 5(2012), 185-186.
23. S. Chitikela, S. K. Dentel, H. E. Allen, Modified method for the analysis of anionic surfactants as methylene blue active substances, *Analyst*., 120(1995), 2001-2004.
24. M. C. Collivignarelli, A. Abbà, G. Bertanza, G. Barbieri, Treatment of high strength aqueous wastes in a thermophilic aerobic membrane reactor (TAMR): Performance and resilience, *Water Sci. Technol*., 76(2017), 3236-3245.
25. I. Ciabattia, F. Cesaro, L. Faralli, E. Fatarella, F. Tognotti, Demonstration of a treatment system for purification and reuse of laundry wastewater, *Desalination*., 245(2009), 451-459.
26. M. C. Collivignarelli, A. Abbà, G. Bertanza, M. Setti, G. Barbieri, A. Frattarola, Integrating novel (thermophilic aerobic membrane reactor-TAMR) and conventional (conventional activated sludge-CAS) biological processes for the treatment of high strength aqueous wastes, *Bioresour. Technol*., 255(2018), 213-219.
27. M. C. Collivignarelli, M. Carnevale Miino, M. Baldi, S. Manzi, A. Abbà, G. Bertanza, Removal of non-ionic and anionic surfactants from real laundry wastewater by means of a full-scale treatment system, *Process Saf. Environ. Prot*., 132(2019), 105-115.
28. S. Šostar-Turk, I. Petrinić, M. Simonič, Laundry wastewater treatment using coagulation and membrane filtration, *Resour. Conserv. Recycl*., 44(2005), 185-196.

29. T. M. Lapara, J. E. Alleman, Thermophilic aerobic biological wastewater treatment, *Water Res.*, 33 (1999), 895–908.
30. J. M. P. E. O. M. R. Wiesner, Water treatment membrane processes, 9th ed., New York, NY : *McGraw-Hill*, 1996., 1996.

How to cite this article:
Kh. R. Kalash, M. H. Al-Furaiji, A. R. Alazraqi, Performance of Thermophilic Aerobic Membrane Reactor (TAMR) for Carpet Cleaning Wastewater. Prog. Color Colorants Coat., 16 (2023), 377-385.

PROGRESS IN COLOR, COLORANTS AND COATINGS

available online @ www.pccc.icrc.ac.ir

Progress in Color Colorants Coating 16 (2023), 387-398

Ministry of Science, Research and Technology
Institute for Color Science & Technology

Investigation of Equilibrium, Isotherm, and Mechanism for the Efficient Removal of 3-Nitroaniline Dye from Wastewater Using Mesoporous Material MCM-48

A. E. Mahdi[1], N. S. Ali[2], K. R. Kalash[3], I. K. Salih[4], M. A. Abdulrahman[1], T. M. Albayati*[1]

[1] Department of Chemical Engineering, University of Technology-Iraq, P.O. Box: 35010, Baghdad, Iraq.

[2] Materials Engineering Department, College of Engineering, Mustansiriyah University, P.O. Box: 1000, Baghdad, Iraq.

[3] Environment and Water Directorate, Ministry of Science and Technology, Baghdad, Iraq.

[4] Department of Chemical Engineering and Petroleum Industries, Al-Mustaqbal University College, P.O. Box: 51001, Babylon, Iraq.

ARTICLE INFO

Article history:
Received: 06 March 2023
Final Revised: 08 June 2023
Accepted: 10June 2023
Available online: 10 Sep 2023

Keywords:
3-Nitrobenzenamine
Adsorption kinetics;
Adsorption thermodynamic
Wastewater treatment
Adsorption mechanism

ABSTRACT

In this work, the MCM-48 mesoporous material was prepared and characterized to apply it as an active adsorbent for the adsorption of 3-Nitroaniline (3-Nitrobenzenamine) from wastewater. The MCM-48 characterizations were specified by implementing various techniques such as; scanning electron microscopy (SEM), Energy dispersive X-Ray analysis (EDAX), X-ray diffraction (XRD), Brunauer-Emmett-Teller (BET) surface area, pore size distribution (PSD), and Fourier transform infrared (FTIR). The batch adsorption results showed that the MCM-48 was very active for the 3-Nitroaniline adsorption from wastewater. The adsorption equilibrium results were analyzed by applying isotherms like Langmuir and Freundlich. The maximum experimental uptake of 3-Nitroaniline according to type I Langmuir adsorption was found to be 89 mg g^{-1} approximately. The Langmuir model is superior to the Freundlich model for the adsorption of 3-Nitroaniline onto the mesoporous material MCM-48. The results demonstrated that 3-Nitroaniline regression coefficients are so high (0.99), the pseudo 2nd order hypothesis for the adsorption mechanism process appears to be well-supported. The findings of adsorption isotherms and kinetics studies indicate the adsorption mechanism is a chemisorption and physical adsorption process. In a thermodynamic analysis, a spontaneous and exothermic adsorption has been observed. Prog. Color Colorants Coat. 16 (2023), 387-398© Institute for Color Science and Technology.

1. Introduction

Wastewater produced by manufacturing locations can be treated in sewage treatment stations. The majority of industrial operations, including chemical and petrochemical plants, petroleum refineries, and chemical plants, have their own unique facilities to handle their effluent water [1]. The non-volatile stable substance 3-nitroaniline ($C_6H_6N_2O_2$), also referred to as meta-nitroaniline and m-nitroaniline, is frequently used as a dyeing agent. An aniline with a nitro functional group in position 3 is known as a 3-nitroaniline. It is described as "not easily compostable" and having "low bioaccumulation potential" and is stable in neutral, acidic, or alkaline conditions. It is used as a chemical intermediate for azo coupling component 17 and the dyes disperse yellow 5 and acid blue 29. The chemical is changed to other substances (dyestuffs and *m*-nitrophenol) during the dyeing process and application

---

*Corresponding author: * Talib.M.Naieff@uotechnology.edu.iq

Doi: 10.30509/pccc.2023.167111.1205

of natural dyes along with nanoparticles to finding definite properties [2-4]. Many serious environmental problems were caused by wastewater containing 3-nitroaniline, because of its carcinogenic properties and high toxicity. Present technologies for a stream of wastewater remediation and recycling also include technology of membrane encompassing reverse ultra-filtration (UF), microfiltration (MF), and osmosis) RO) [5-8]. Membrane systems have alternatives, such as chemically based oxidation processes and air/oxygen-based on non or oxidation. The first class comprises advanced oxidation processes (AOPs), which produce hydroxyl radicals that are then used for oxidation by using hydrogen peroxide, UV light, and ozone [9-12]. The second class consists of wet air, catalytic wet air, and dry oxidation [13-15]. Another type of treatment used in wastewater cleanup is adsorption. Adsorption techniques have been used to eliminate organic and inorganic contaminants from wastewater, with a particular emphasis on the usage of various materials as the preferred adsorbent. It may be said that the regeneration of the used adsorbent materials is a time-consuming and expensive procedure [13]. Because of this, there is interest in creating new adsorbents to remove contamination in the aqueous waste stream [14, 15]. Based on the size, shape, and other characteristics of a molecule, such as polarity, Zeolites can reject or selectively adsorb certain compounds. This means that they can act as adsorbents. Organ clays have been the focus of several investigations on organic molecule adsorption from aqueous solutions. There have been reports on silicate [16], mesoporous materials [17], modified and unmodified zeolites [18]. For application in separation procedures as an adsorbent, the candidate MCM-48 appears to be more promising. Scientists have been very interested in the mesoporous material such as MCM-41, MCM-48, and SBA-15 because of its potential use as supports of catalyst, catalysts, drug delivery, and absorbents [19, 20]. These material properties are high thermal stability, specific pore volume up to 1.2 cm^3g^{-1}, surface areas (1000-1500 m^2g^{-1}), a narrow pore-size distribution, and ‘‘non-cytotoxic’’ properties [21]. Mesoporous silica-based materials, including MCM-48, have been developed as efficient catalyst carriers, adsorbents, and cutting-edge drug delivery systems. [22]. This is due to their very considerable thermal stabilities, porous morphologies, extremely large surface areas, and highly reactive surfaces for the presence of the silanol groups [23, 24].

The main aim of the present research was to investigate the removal of 3-Nitroaniline ($C_6H_6N_2O_2$) from wastewater solutions by applying MCM-48 as an efficient adsorbent. The adsorption isotherms, kinetics, and thermodynamic were examined. Moreover, the adsorption mechanism of 3-Nitroaniline wastewater onto the surface of MCM-48 adsorbent was studied in a batch adsorption process. Finally, regeneration and desorption kinetics were also tested for MCM-48 to discover the actual adsorbent utility and its applicability for reusability in a continuous adsorption system. To our knowledge, no publishing results is recommending on the investigation of 3-Nitroaniline (3-Nitrobenzenamine) removal from aqueous solution by MCM-48 adsorbent. It is acquiring special recognition and considers as a promising alternative to conventional water treatment in textile industries.

2. Experimental

2.1. Chemicals

The chemicals applied for this work were cetyl trimethyl ammonium bromide $C_{19}H_{42}BrN$ (CTAB; purity >98%) as a surfactant, tetraethyl orthosilicate $Si(OC_2H_5)_4$ (TEOS; purity > 98 % (as a silica source, sodium hydroxide (NaOH), hydrochloric acid (HCl), and 3-Nitroaniline (3-Nitrobenzenamine) ($C_6H_6N_2O_2$). All reactants were analytically purchased from Sigma Aldrich Chemical Company. All materials were applied without additional purification.

2.2. Preparation of MCM-48

According to the preparation method outlined by [25-27], MCM–48 was synthesized. The following steps were used to create MCM-48 in a representative preparation: 90 g of deionized water mixed with 10 g of CTAB. 1 g of NaOH was then mixed with the solution after it had been rapidly agitated at 35 °C for 40 minutes. Eleven cm^3 of TEOS was added, after stirring the solution for 60 minutes at 35 °C, and the mixture was then stirred at this temperature for another 30 min. Final heating of the combination was place in an autoclave under static conditions for 24 hours at 150 °C; the resultant MCM-48 was then cooled down for 1 hour, filtrated, and rinsed with distilled H_2O before being dry at ambient temperature. The produced sample was then calcined for 6 hours at a temperature of 650 ºC applying a ramp rate for heating 2 °C/min.

2.3. Characterization

The MiniFlex (Rigaku) diffractometer was used to record the patterns of small-angle XRD in ambient settings using Cu K radiation ($\lambda = 1.5406$Å). The X-ray tube was run at 40 kV and 30 mA, and the data were reported in the 2θ range of 0.5-8° with a 2 step size of 0.01 and a step time of 10s. The formulae $n\lambda = 2d\sin\theta$ and $\alpha_o = 2d100/\sqrt{3}$ were applied to determine the unit cell and d-spacing characteristics. The pore analyzer of a micrometrics ASAP 2020 was used to assess the adsorption and desorption of nitrogen using N_2 physisorption at -196 °C. All specimens were degassed in the degas adsorption analyzer port for 3 hours at 350 °C and vacuum ($p < 10^{-5}$ mbar). The BET method was used to calculate the specimens' BET-specific surface areas for the relative pressure range of 0.05 to 0.25. With the use of the Barrett-Joyner-Halenda (BJH) approach, which is based on thermodynamics, the distributions of pore size were specified from the isotherm desorption branch. The quantity of liquid N_2 adsorbed at $P/P_0 = 0.995$ was used to calculate the total pore volume. This information was obtained from the N_2 isotherm's adsorption branch. Through the use of the unit cell parameter(α_o) and pore size diameter, the pore walls thickness (t_W) was estimated (d_P). Using BET analysis (4V/A), the average mesopore sizes for the single specimens were calculated from the data of nitrogen sorption. SEM was carried out on a JEOL (JSM-5600 LV). EDAX is an analytical method that creates the adsorbent elemental analysis to determine the composition of chemicals when combined with SEM. Using a NICOLET 380 FT-IR spectrometer, the solid samples' infrared spectra were measured were in the 4000 to 400 cm^{-1} range at areas with 4 cm^{-1} resolutions in transmission mode at ambient temperature.

2.4. Experiments of batch adsorption

To assess 3-Nitroaniline isotherms of adsorption onto the adsorbents at 25 °C, batch adsorption tests were performed. By dissolving 0.2 g of 3-Nitroaniline in 1 litre of distilled water, stock solutions of 3-Nitroaniline were created. At 25 °C, experiments of batch adsorption were used to assess the 3-Nitroaniline adsorption over the adsorbents. Then, 10 concentrations (0-0.2 g/L) were used to create a calibration curve using a UV-Spectrometer (model HP 8453) calibrated to 25 °C. λmax was discovered to be 278 nm for 3-Nitroaniline. The calibration was necessary to compare final absorbance with beginning absorbance. In 100 mL conical flasks, 15 different concentrations of the aforementioned solutions were created, starting from 0.001 - 0.06 g/L. 100 mL of each was added to 0.01g MCM-48, which was then stirred in several positions at 150 rpm for an hour at room temperature (25 °C). This made it possible for the mesoporous substance MCM-48 to completely mix with the mixture. Following the adsorption procedure, equal quantities of the solutions were centrifuged for five minutes at 3500 rpm using a centrifuge (model Hermle Z 200 A). This allowed the zeolite to completely separate from the solution and enable analysis with a UV-spectrophotometer (TU1900) operating at a wavelength of 278 nm. According to the following equation, the (%R) of 3-Nitroaniline was calculated (Eq.1) [28]:

$$\%R=\frac{Co\text{-}Ce}{Co}\times 100\% \tag{1}$$

Using the following equation, the amount of adsorption (qe) was determined (Eq.2) [29]:

$$qe=\frac{V(Co\text{-}Ce)}{m} \tag{2}$$

Where, qe (mg / g) denotes the adsorption amount, V (L) is the 3-Nitroaniline solution volume, m (g) is the mass of the absorbent applied used in the experiments, C_0 (mg/L) and C_e (mg/L) are the initial and equilibrium concentration of 3-Nitroaniline, respectively [30].

2.5. Adsorbent's reuse

The regeneration was studied applying an exhausted MCM-48 adsorbent. Following the 3-Nitroaniline adsorption solutions onto MCM-48, the mixture was filtered, the discarded adsorbent material that had uptake 3-Nitroaniline was rinsed in a sizable amount of H_2O until no 3-Nitroaniline remained in solution, and then dried under vacuum conditions at 60 °C for the duration of an entire night. Several adsorption-desorption cycles were achieved in order to examine the MCM-48 material's resilience and potential for regeneration.

3. Results and Discussion

3.1. Synthesized materials characterization

The prepared MCM- 48 was subjected to SEM and EDAX characterization procedures. At a magnification of 1000, SEM pictures of this material are displayed in

Figure 1a. The peaks on the EDAX graph in Figure 1b show the components' average weight % values that C, O, and Si made up the zeolite. To get accurate average weight % for each of the components, EDAX graphs were created for a number of different locations on the SEM pictures.

As can be displayed in Figure 2a, the MCM-48 small angle XRD patterns before and after adsorption exhibit a strong mesostructured-descriptive diffraction peak at around 2θ of 0.9^{o}. Furthermore, two further peaks, indexed as (2 1 1), and (2 2 0) were seen in the XRD patterns. Two reflection peaks at 2θ less than 3^{O} and a string of sporadic weak peaks in the range 3.5^{O}–5.5^{O} are indexed to the Ia3d cubic structure. When compared to comparable peaks described in the literature, the peaks acquired in our investigation match those reported there quite well [31]. The outcomes shown in Table 1 illustrate how MCM-48 has a periodic ordered structure and very stable before and after adsorption.

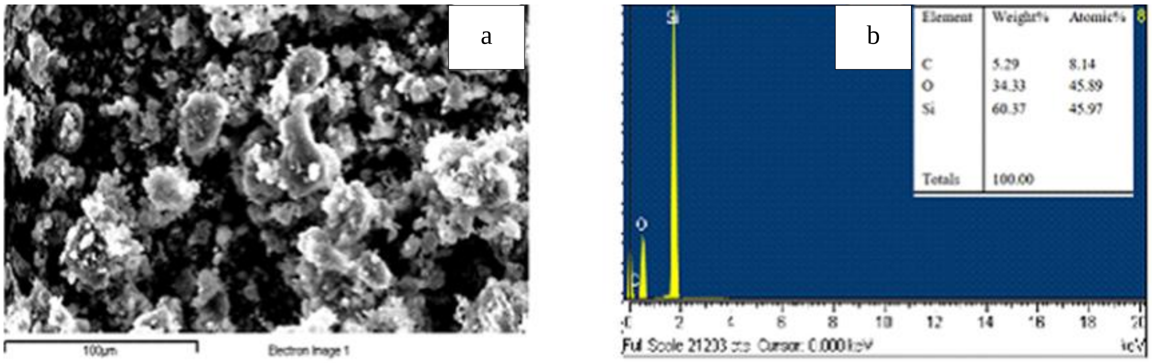

Element	Weight%	Atomic%
C	5.29	8.14
O	34.33	45.89
Si	60.37	45.97
Totals	100.00	

Figure 1: (a) SEM picture of MCM-48 at a 1000x magnification. (b) A typical MCM-48 EDAX picture.

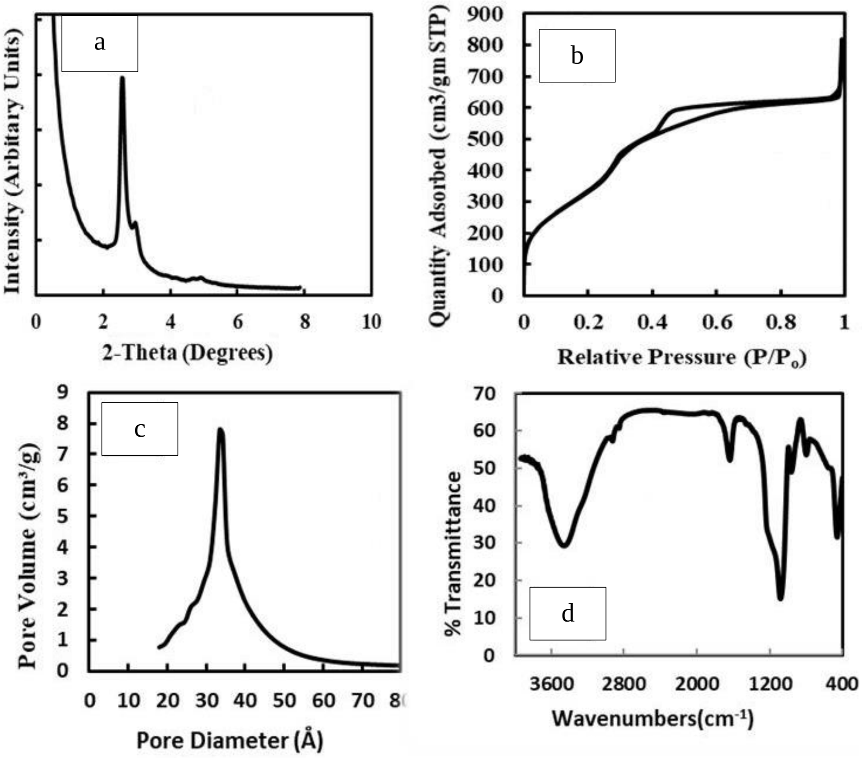

Figure 2: MCM-48 (a) X-ray diffraction pattern before and after adsorption (b) isotherms of nitrogen adsorption – desorption, (c) BJH pore size distribution, and (d) FT-IR spectra.

Table 1: MCM-48's physicochemical characteristics.

Sample	S_{BET} (m^2/g)	V_P (cm^3/g)	$V_{\mu P}$ (cm^3/g)	D_P (nm)	a_o (nm)	t_{wall} (nm)
MCM-48	1450	1.5	0.7	3.4	3.7	0.5

According to Figure 2b, the N_2 adsorption isotherms of MCM-48 have a type IV isotherm and a type H1 hysteresis loop. A small pore size distribution is indicated by sharp adsorption and desorption branches. The sharpness and height of the capillary condensation process in the isotherms, in general, represent the uniformity of the pore size for mesoporous molecular sieves. In the relative pressure (P/P_0) range of 0.05 to 0.25, the MCM-48 displays type IV isotherm, as illustrated in Figure 2b. Together with the structural features discovered by nitrogen adsorption investigations, Table 1 explains the sample's specific surface area, pore size, pore volume, and wall thickness together with the structural characteristics obtained from nitrogen adsorption studies.

Figure 2c displays the pore size distribution (PSD) for the MCM-48. The content produced by CTAB: NaOH: The pore size distribution of TEOS is broad and centered at 35 Å. A mesopores higher amount was discovered for the basic synthesization, which created the most evident pore size dispersion and had a fairly regular organization [32]. Figure 2d displays the FT-IR spectrum of MCM-48, which includes the characteristic Si-O-Si bands at 1082, 964,799, and 460 cm^{-1}. Stretching vibrations either Si OH or Si O Si can be attributed to the absorption band at around 960 cm^{-1}. Because of the existence of the surface OH groups and the strong H_2 bonding interactions between them, the wide band at approximately 3463 cm^{-1} is caused. Finally, the band at about 1637 cm^{-1} can be attributed to the distortion modes of the OH bonds of adsorbed H_2O [33].

3.2. 2-Nitroaniline adsorption

3.2.1. Contact time effect

The contact time duration was determined for the 3-Nitroaniline solution to adsorb it onto MCM-48 in order to attain equilibrium as indicated in Figure 3. λmax was discovered to be 278 nm for 3-Nitroaniline. The adsorption of 3-Nitroaniline solutions is clearly much influenced by time. The amount adsorbed on the nanoporous material zeolite was quantified for this purpose. The findings showed that equilibrium was established in under 20 minutes. It may take less time to attain balance. As a result, 60 minutes was specified to be the ideal contact time for the adsorbent. So, for the MCM-48 adsorbent to get saturated with analysis, just a very little contact time is needed. The adsorption capacity was greatly increased by higher cationic surfactant concentrations and their high availability in the pores of the adsorbent. This finding is significant, since one of the key factors taken into account for an efficient system of wastewater treatment is the equilibrium time. Therefore, in all experiments, adsorption was let to continue for 1 hour [34].

3.2.3. Effect of agitation rotary speed

The adsorption of hazardous solutes was examined by changing the agitation rotary speed from 0 to 200 rpm while maintaining a concentrated solution and contact time constant. The removal of harmful 3-Nitroaniline solutions rose when the agitation rotary speed was raised from 0 to 150 rpm; however, it then remained constant. This suggests that an agitation rotary speed in the 150-200 rpm range is enough to ensure the surfactants optimum cationic sites present in the pores of MCM-48 adsorbent are rapidly made available for absorption. The best agitation rotary speed for the remaining studies was determined to be 150 rpm [35].

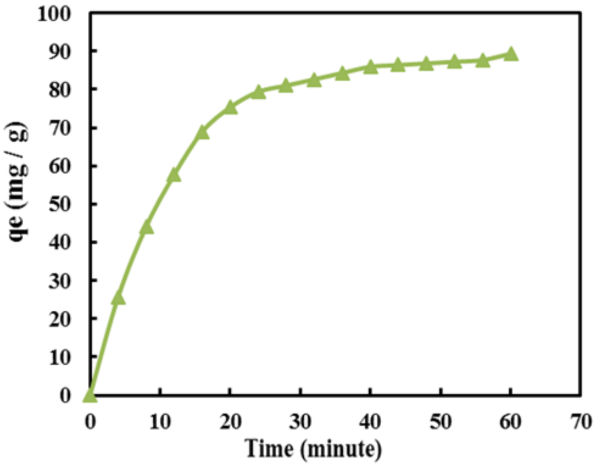

Figure 3: Contact time effect on the 3-Nitroaniline adsorption.

3.2.4. Concentration effect

As a 2-Nitroaniline initial concentration function C_0, Figure 4 depicts the % removal of 3-Nitroaniline estimated from Eq. 1. Approximately 64% of the 3-Nitroaniline content, which was initially 4 mg dm^{-3}, is removed from solution. The % removal of 3-Nitroaniline was decreased with the increased concentration at a constant mass of MCM-48. This reduces the amount of concentrated solution material that gradually absorbs more material. The quantity that may adsorb into the pores decreases when the maximum absorption of the MCM-48 pores is approached [36].

3.4 Adsorption isotherm

Figure 5 depicts the 3-Nitroaniline compound's adsorption isotherms, where Ce represents the adsorbate equilibrium concentration in solution at equilibrium and qe represents the adsorbate adsorbed per gram of MCM-48. 3-Nitroaniline molecule was generally adsorbed throughout a variety of concentrations, demonstrating the efficiency of MCM-48 in the removal of 3-Nitroaniline from aqueous solutions as an adsorbent. An essential driving factor for overcoming all ion and molecule mass transfer resistances between the solid phases and aqueous is the initial adsorbate concentration [37]. The initial solution concentration in the current investigation is adjusted from 4 - 60 mg/L however, the adsorbent dose stays constant at 0.01 g/100 mL. Figure 5 shows that when the equilibrium adsorption capacity increases, the initial 3-Nitroaniline concentration also rises.

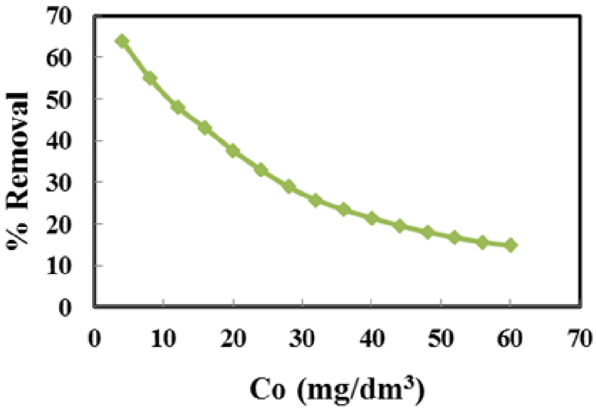

Figure 4: Initial 3-Nitroaniline concentration impact on removal efficiency at contact time=60 min and MCM-48 dosage=0.01 g.

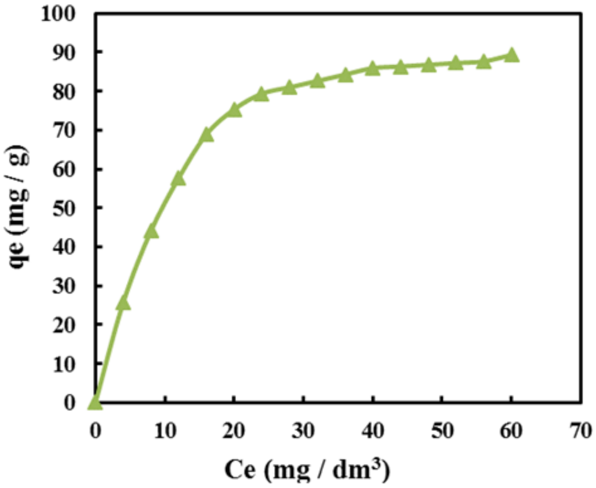

Figure 5: Isotherms of adsorption onto MCM-48 with 0.01g/100 mL adsorbent.

The uptake of equilibrium adsorption for 3-Nitroaniline rose from 20-89 mg/g as the starting concentration solution of 3-Nitroaniline was increased from 4 to 60 mg/L. This is because of the excess in number of 3-Nitroaniline molecules of poisonous solutes vying for the few remaining sites of binding onto the adsorbent's surface. According to the finding shown in Figure 5, cationic surfactants that include MCM-48 have a very high uptake for 3-Nitroaniline adsorption. As seen in Figure 2d, silanol groups (Si-OH) constitute significant sites of adsorption on the MCM-48surface. These sites are present in this substance in addition to cationic sites that were provided by a cationic template. It appears that a key determinant in the adsorption of 3-Nitroaniline on the surface of MCM-48 is the number of sorption sites. This can be explained by the fact that there are initially lots of empty surface sites accessible for adsorption. It was also proposed that as time went on, a potent attraction force developed between the molecules of 3-Nitroaniline and the sorbent. Due to saturation, it is difficult to fill the remaining open surface sites, which may also be related to a lack of accessible sorption sites towards the conclusion of the adsorption process [38].

The adsorption isotherms for 3-Nitroaniline compound have profiles that are consistent with Type I Langmuir adsorption; the quantity adsorbed rose gradually until it reached values in the 25-89 mg g^{-1} range [39]. The study of adsorption isotherms has been done so as to model the adsorption behavior.

According to Figures 6a and b, the Freundlich and Langmuir isotherm models were used to assess the 3-Nitroaniline species adsorption process. Equations of Langmuir and Freundlich are given in equations 3 and 4, respectively.

$$\frac{Ce}{qe}=\left(\frac{1}{bqmax}\right)+\left(\frac{1}{qmax}\right)Ce \qquad (3)$$

$$\text{Log qe}=\text{Log KF}+\left(\frac{1}{n}\right)\text{Log Ce} \qquad (4)$$

Graphing the Eq. 3 linear form of, or Ce/qe vs. Ce, which was applied to determine the constants of Langmuir and maximal uptake or capacity qmax, corroborated type I adsorption. According to Table 2 and Figure 9a, the Langmuir profile for the 3-Nitroaniline molecule is a straight line, supporting Type I adsorption. R^2 values are 0.99. Figure 6 displays the linearized isotherm data using the Langmuir equation. Table 2 lists the regression coefficients. R^2=0.99, a high correlation coefficient, denotes strong agreement between the parameters. 3-Nitroaniline has an adsorption ability to create monolayers that may reach up to 100 mg/g, according to the constant qmax. The value of the adsorption energy constant, b, for 3-Nitroaniline is 0.5 dm^3/mg. The Freundlich equation was also fitted to the similar data, which is seen in Figure 6b. Table 2 provides the constants of regression. The correlation coefficient values demonstrate how closely the data follow the Langmuir equation. The 3-Nitroaniline component adsorption on mesoporous materials is better depicted by the Langmuir model than by the Freundlich model. Furthermore, 3-Nitroaniline has 1/n values that are smaller than 1, which is a sign of a high adsorption intensity [40].

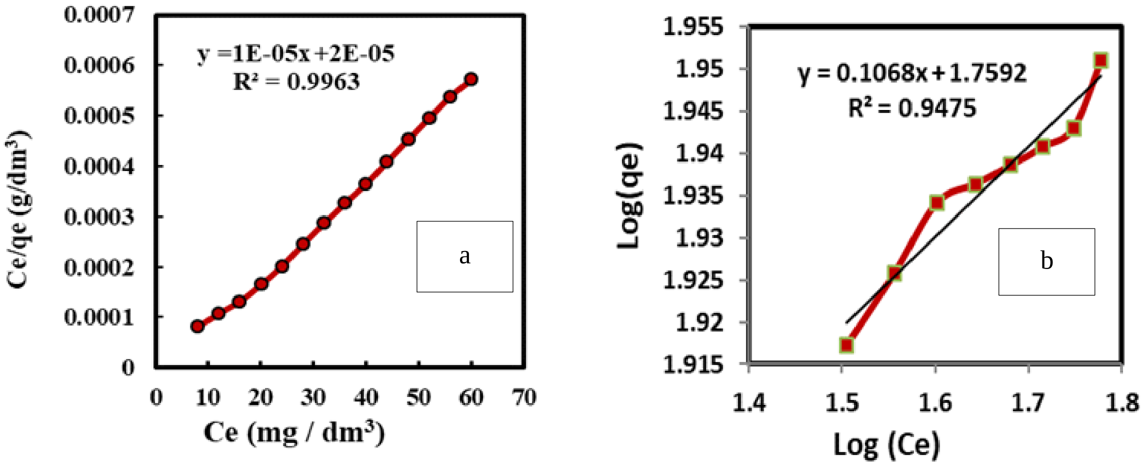

Figure 6: 3-Nitroaniline adsorption on MCM-48 according to (a) Langmuir, and (b) Freundlich isotherms.

Table 2: Constant of Langmuir and Freundlich for 3-Nitroaniline adsorption on MCM-48.

Adsorb ate	Langmuir constants				Freundlich constants	
	qmax ($mg.g^{-1}$)	b ($dm^3.mg^{-1}$)	R^2	K_F	1/n	R^2
3-nitroaniline	100	0.5	0.9963	57.438	0.1068	0.9475

3.5. Adsorption kinetics

One of the most important elements that defines the effectiveness of adsorption is the rate of 3-Nitroaniline adsorption by MCM-48. A pseudo-first and second order model have been applied to explain kinetics of 3-Nitroaniline adsorption. Figures 7a and b illustrate how pseudo-first- and second-order kinetics models were used to analyze the 3-Nitroaniline kinetics of adsorption onto MCM-48. Table 3 contains the results for the kinetic model parameters and the correlation coefficients (R^2). According to Table 3, the theoretical values (qe cal.) calculated from the pseudo-first-order kinetic model gave substantially different values when compared to experimental values (qe exp.). As a result, the pseudo 1st order kinetic model is representing this adsorption system well. The theoretical (qe cal.) and the experimental values (qe exp.) were calculated using the pseudo 2nd order kinetic model are extremely close to each other, as shown in Table 3. The coefficients R^2 value is also quite near to 1, which supports the validity of the pseudo-second-order equation. In the current research, the adsorption data were analyzed applying two important kinetic models. The integrated pseudo-first-order rate equation is written as [41]:

$$\text{Log}\left(qe-qt\right)=\text{Log}qe-k_1t \tag{5}$$

The adsorbed 3-Nitroaniline quantity at equilibrium time t is shown by qe and qt, respectively. k_1 : is the pseudo-first-order adsorption equilibrium rate constant. The pseudo-second-order equation is [42]:

$$\frac{t}{qt}=\frac{1}{k_2qe^2}+\frac{1}{qe}t \tag{6}$$

k_2: is the rate constant of pseudo-second-order.

Figures 7a and b explain the findings of Pseudo-first and second order models were used to fit the experimental data, respectively. The results from the adsorption kinetics are extremely well matched by the pseudo-second order model, as shown in Figure 7b. Given that 3-Nitroaniline regression coefficients are so high (0.99), the pseudo 2nd order hypothesis for the adsorption mechanism process appears to be well-supported [43].

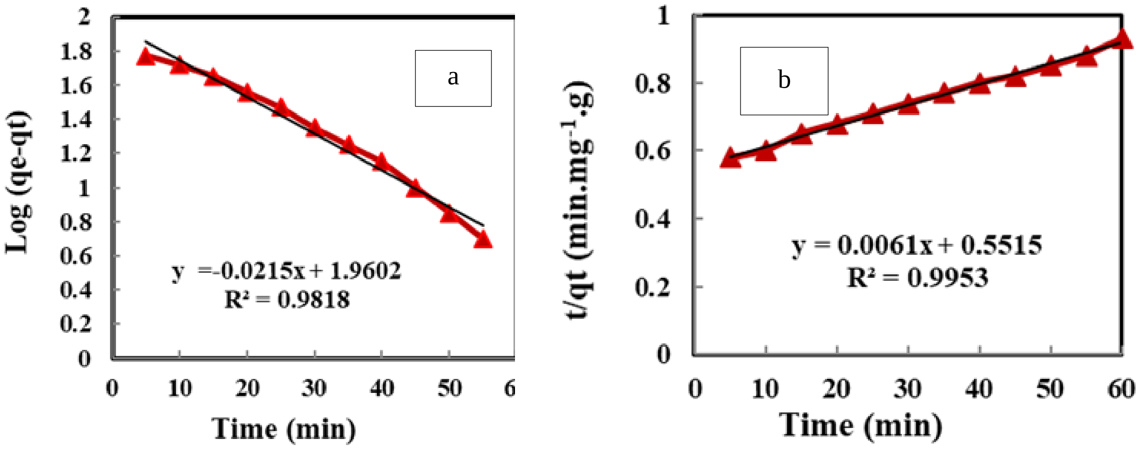

Figure7: (a) Pseudo 1st and (b) 2nd order kinetics for the 3-Nitroaniline adsorption on MCM-48.

Table 3: Kinetics parameters values for 3-Nitroaniline adsorption on MCM-48.

Adsorbates	qe.exp. (mg/g)	Pseudo-first order constants			Pseudo-second order constants		
		qe.cal. (mg/g)	K_1 (g/mg.min)	R^2	qe.cal. (mg/g)	K_2 (g/mg.min)	R^2
3-Nitroaniline	65	91	0.0215	0.981	163	$6.747*10^{-5}$	0.995

3.6. Adsorption thermodynamics

As shown in Figure 8, the thermodynamic parameters for the adsorption of 3-Nitroaniline at different temperatures are given in Table 4 by the plot of the linear Van't Hoff equation (ln kc versus 1/T). The negative values of ΔG for applied temperatures are a sign of spontaneous sorption. Besides, the value of ΔS was negative, demonstrating that the adsorption process could reduce chaos degree of the system, Furthermore, the value of ΔS was negative, showing that the sorption process reduced chaos. while the negative value of enthalpy ΔH indicates that the sorption is exothermic.

3.7. Adsorption mechanism

To understand the adsorption mechanism process, it is important to know the structure of the adsorbent and adsorbate as shown in Figure 9 3-Nitroaniline molecule is an organic chemical substance, particularly a primary aromatic amine. It consists of an amino group attached to a benzene ring. On the other hand, MCM-48 adsorbent is the most common molecular sieves of mesoporous materials that is intensively investigated by researchers. The most notable feature of the MCM-48 is that despite having an amorphous silica wall, it has a long-range organized structure and consistent mesoporous. This important material has the majority of silanol group. Based on the structure of the 3-Nitroaniline, MCM-48 and experimental results of kinetic, FTIR and EDX analysis, the adsorption mechanism of 3-Nitroaniline onto MCM-48 adsorbent can be determined. Based on FTIR results, the strong adsorption band of at – C = C–group was decreased in intensity and shifted from 1681 to 1600 cm^{-1} owing to π–π interactions between 3-Nitroaniline molecule with – C = C– onto the surface of MCM-48. While the band of – OH groups was increased in intensity and a slight shift from 3330 to 3335 owing to hydrogen bond formation between the $–N(CH_3)_2$ group of 3-Nitroaniline molecules and the – OH group in the MCM-48 surface. The band of C = O stretch vibration of carboxylic acid was a slight increase in intensity due to electrostatic attraction between a cationic $^+N(CH_3)_3^+$ group of MG molecules with the negative charge of COOH group onto the MCM-48 surface. According to the results of adsorption isotherms and kinetics study, the adsorption mechanism is a chemisorption and physical adsorption process. Therefore, these results provide enough evidence to support the 3-Nitroaniline adsorption onto the MCM-48 surface by different mechanisms such as hydrogen bonding, electrostatic interaction and π-π interactions [44, 45].

Table 4: Thermodynamic parameters for the sorption 3-Nitroaniline on MCM-48 at different temperatures.

Adsorbent	T/^{0}K	Kc L/ g	ΔG kJ/mol	ΔH kJ/mol	ΔS J /mol. k	R^2
MCM-48	298	11.11	-5.83	-23.84	-60.21	0.9721
	308	7.44	-5.03			
	318	6.07	-4.66			

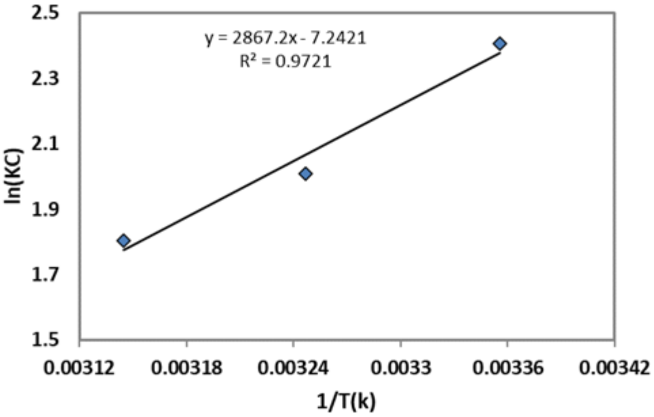

Figure 8: Plot of ln Kc versus 1/T for 3-Nitroaniline sorption by 0.01g of MCM-48 (C_o=10, time=60 min, RPM=150).

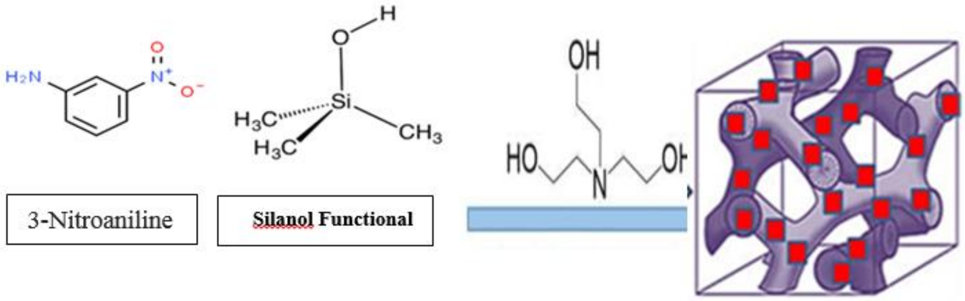

Figure 9: Mechanism adsorption of 3-Nitroaniline onto MCM-48 adsorbent.

3.8. Adsorbent reuse

The possibility of recycling the adsorbent was examined for applying a depleted MCM-48 after regeneration. For the purpose of proving that the MCM-48 could be regenerate by removing the adsorbates, desorption investigations were carried out. When using the MCM-48 again, it is crucial to establish that desorption takes place. According to the results of the trials, 3-Nitroaniline was effectively and efficiently desorbed into deionized water in a single cycle, with an efficiency of over 90 %. It can be seen from this that used materials may be recycled. It is possible to perform a more thorough investigation to learn more about desorption, including the impacts of solution concentration, adsorbate loading, temperature, etc. The focus of this essay does not extend to this study [46].

4. Conclusion

In this study, 3-Nitroaniline was easily adsorbed from an aqueous adsorbate solution utilizing from the MCM-48 mesoporous material. According to a linear analysis with R^2 values of 0.99, 3-Nitroaniline molecules matched to Type I Langmuir adsorption. Under appropriate experimental circumstances, nanoporous material demonstrated considerable aniline adsorption capacity; as a result, it may be suggested as a practical adsorbent. The Langmuir adsorption isotherm was discovered the best suited with the experimental, indicating monolayer adsorption on a homogeneous surface. The Langmuir isotherm was used to calculate the theoretical and experimental maximal adsorption capacity of 100 mg g^{-1}, and 89 mg g^{-1}, respectively. The pseudo-second-order model can forecast the dynamics of adsorption. Adsorption isotherms and kinetics models indicate that chemical and physical adsorption are the two processes involved in the adsorption mechanism. It is obvious from the negative Gibbs free energy change of the adsorption that it is a spontaneous adsorption. Adsorption is an exothermic process as indicated by the negative enthalpy change. At equilibrium, 3-Nitroaniline adsorption decreases with increasing temperature.

Acknowledgments

The authors are grateful to the Department of Chemical Engineering at the University of Technology-Iraq, the Mustansiriyah University/ College of Engineering/ Materials Engineering Department Baghdad-Iraq, the Department of Chemical and Petroleum Industries Engineering, Al-Mustaqbal University College.

5. References

1. A. Al-Nayili, H. Sh. Majdi, T. M. Albayati, N. M. Cata Saady., Formic acid dehydrogenation using noble-metal nanoheterogeneous catalysts: towards sustainable hydrogen-based energy, *Catal.* 12(2022), 324-336.
2. S. M. Alardhi, J. M. Alrubaye, T. M. Albayati, Removal of methyl green dye from simulated waste water using hollow fiber ultrafiltration membrane, 2nd International Scientific Conference of Al-Ayen University (ISCAU-2020).
3. J. O'Brien, T.F. O'Dwyer, T. Curtin, A novel process for the removal of aniline from wastewaters, *J. Hazard. Mater.*, 159(2008), 476-482.
4. M. Sadeghi-Kiakhani, E. Hashemi, Study on the effect of pomegranate peel and walnut green husk extracts on the antibacterial and dyeing properties of wool yarn

treated by chitosan/Ag, chitosan/Cu nano-particles, *Prog. Color Colorants Coat.*, 16(2023), 221-229.

5. C. Ko, S. Chen, Enhanced removal of three phenols by lactase polymerization with MF/UF membranes, *Bioresour. Technol.*, 99(2008), 2293-2298.
6. N. S. Ali, K. R. Kalash, A. N. Ahmed & T. M. Albayati, Performance of a solar photocatalysis reactor as pretreatment for wastewater via UV, UV/TiO_2, and UV/H_2O_2 to control membrane fouling, *Sci. Rep.*, 12(2022), 16782.
7. N.S. Abbood, N.S. Ali, E.H. Khader, H.Sh. Majdi, T.M. Albayati, N.M. Cata Saady, Photocatalytic degradation of cefotaxime pharmaceutical compounds onto a modified nanocatalyst, *Res. Chem. Intermed.*, 49(2023), 43-56.
8. A.L. Ahmad, K. Y. Tan, Reverse osmosis of binary organic solute mixtures in the presence of strong solute-membrane affinity, *Desalin*, 165(2004), 193-199.
9. V.V. Goncharuk, D.D. Kucheruk, V.M. Kochkodan, V.P. Badekha, Removal of organic substances fromaqueous solutions by reagent enhanced reverse osmosis, *Desalin*, 143(2002), 45-51.
10. T. Hirakawa, T. Daimon, M. Kitazawa, N. Ohguri, C. Koga, N. Negishi, S. Matsuzawa, Y. Nosaka. An approach to estimating photocatalytic activity of TiO_2 suspension by monitoring dissolved oxygen and superoxide ion on decomposing organic compounds, *J. Photochem. Photobiol.*, 190(2007), 58-68.
11. A. M. Amat, A. Arques, M. A. Miranda, S. Segu´ı, R.F. Vercher, Degradation of rosolicacid by advanced oxidation processes: ozonation vs. solar photocatalysis, *Desalin*, 212(2007), 114-122.
12. G. L. Puma, P. L. Yue, Effect of the radiation wavelength on the rate of photocatalyticoxidation of organic pollutants, *Ind. Eng. Chem. Res.*, 41(2002), 5594-5600.
13. B. M. Nader, Performance of advanced methods for treatment of wastewater: UV/TiO_2, RO and UF, *Chem. Eng. Process.*, 43(2004), 935-940.
14. R. Morent, J. Dewulf, N. Steenhaut, C. Leys, H. Van Lagenhove, Hybrid plasmacatalyst system for the removal of trichloroethylene from air, *J. Adv. Oxid. Technol.*, 9(2006), 53-58.
15. J. Levec, A. Pintar, Catalytic wet-air oxidation processes: a review, *Catal. Today*, 124(2007), 172-184.
16. S.K. Bhargava, J. Tardio, H. Jani, D.D. Akolekar, K. Foeger, M. Hoang, Catalytic wet-air oxidation of industrialwaste streams, *Catal. Surv. Asia*, 11(2007), 70-86.
17. C. H. Ko, C. Fan, P. N. Chiang, M. K. Wang, K. C. Lin, *p*-Nitrophenol, phenol and aniline sorption by organo-clays, *J. Hazard. Mater.*, 149(2007), 275-282.
18. S. Razee, T. Masujima, Uptake monitoring of anilines and phenols using modified zeolites, *Anal. Chim. Acta.*, 464(2002), 1-5.
19. N. A. Atiyah, T. M. Albayati, M. A. Atiya, Functionalization of mesoporous MCM-41 for the delivery of curcumin as an anti-inflammatory therapy, *Adv. Powder Technol.*, 33(2022), 103417.
20. N. A. Atiyah, T. M. Albayati, M. A. Atiya., Interaction behavior of curcumin encapsulated onto functionalized SBA-15 as an efficient carrier and release in drug delivery, *J. Mol. Struct.*, 1260(2022), 132879.
21. E. Narita, N. Horiguchi, T. Okabe, Adsorption of phenols, cresols and benzyl alcohol from aqueous solution by silicalite, *Chem. Lett.*, 6(1985), 787-790.
22. U. S. Taralkar, M. W. Kasture, P .N. Joshi, Influence of synthesis condition on structure properties of MCM-48, *J. Phys. Chem. Sol.*, 69(2008), 2075-2081.
23. L. Pajchel, W. Kolodziejski. Synthesis and characterization of MCM 48/hydroxyapatite composites for drug delivery: Ibuprofen incorporation, location and release studies, *Mater. Sci. Eng. C*, 91(2018), 734-742.
24. M. Shaban, M. R. Abukhadra, A. Hamd, R. R. Amin, A. A. Khalek. Photocatalytic removal of Congo red dye using MCM-48/Ni_2O_3 composite synthesized based on silica gel extracted from rice husk ash; fabrication and application, *J. Environ. Manage.*, 204(2017), 189-199.
25. R. Nejat, A. R. Mahjoub, Z. Hekmatian, A. Tahereh. Pd-functionalized MCM-41 nanoporous silica as an efficient and reusable catalyst for promoting organic reactions, *RSC Adv.*, 5(2015), 16029-16035.
26. A. M. Doyle, B. K. Hodnett, Synthesis of 2-cyanoethyl-modified MCM-48 stable to surfactant removal by solvent extraction: Influence of organic modifier, base and surfactant, *Micropor*, *Mesopor. Mater.*, 58(2003), 255-261.
27. A. M. Doyle, E. Ahmed, B. K. Hodnett, The evolution of phases during the synthesis of the organically modified catalyst support MCM-48, *Catal. Today*, 116(2006), 50-55.
28. N. S. Ali, N. M. Jabbar, S. M. Alardhi, H. Sh. Majdi, T. M. Albayati, Adsorption of methyl violet dye onto a prepared bio-adsorbent from date seeds: isotherm, kinetics, and thermodynamic studies, *Heliyon*, 8(2022), e10276,
29. W. A. Muslim, T. M. Albayati, S. K. Al-Nasri, Decontamination of actual radioactive wastewater containing ^{137}Cs using bentonite as a natural adsorbent: equilibrium, kinetics, and thermodynamic studies, *Sci. Rep.*, 12(2022), 13837.
30. Y. A. Abd Al-Khodor, T. M. Albayati, Real heavy crude oil desulfurization onto nanoporous activated carbon implementing batch adsorption process: equilibrium, kinetics, and thermodynamic studies, *Chem. Afr.*, 6(2023), 747-756
31. S. Han, J. Xu, W. Hou, X. Yu, and Y. Wang, Synthesis of high-quality MCM-48 mesoporous silica using Gemini surfactant dimethylene- 1,2-bis (dodecyldimethylammonium bromide), *J. Phys. Chem. B*, 108(2004), 15043-15048.
32. Z. Qiang, X. Bao, W. Ben, MCM-48 modified magnetic mesoporousnanocomposite as an attractive

adsorbent for the removal of sulfamethazine from water, *Water Res.*, 47(2013), 4107-4114.

33. T. M. Al-Bayati, Removal of aniline and nitro-substituted aniline from wastewater by particulate nanoporous MCM-48, *Part. Sci. Technol.*, 32(2014), 616-623.
34. H. Tian, J. Li, L. Zou, Z. Mua and Z. Hao, Removal of DDT from aqueous solutions using mesoporous silica materials, *J. Chem. Technol. Biotechnol.* 84(2009), 490-496.
35. T. M. Albayati, A. M. Doyle. Purification of aniline and nitrossubistituted aniline contaminants from aqueous solution using beta zeolite, *Chem. Bulgarian J. Sci. Edu.*, 23(2014), 105-114.
36. S. Fauzia, H. Aziz, D. Dahlan, R. Zein. Study of equilibrium, kinetic and thermodynamic for removal of Pb(II) in aqueous solution using Sago bark (Metroxylon sago), AIP Conference Proceedings 2023, 020081 (2018).
37. T. M. Albayati, A. M. Doyle., Shape-selective adsorption of substituted aniline pollutants from wastewater, *Adsorpt. Sci. Technol.*, 31(2013), 459-468.
38. T. M. Albayati, A. A. Sabri, D. B. Abed, Adsorption of binary and multi heavy metals ions from aqueous solution by amine functionalized SBA-15 mesoporous adsorbent in a batch system, *Desalin. Water Treat.*, 151(2019), 315-321.
39. R. Saad, K. Belkacemi, S. Hamoudi, Adsorption of phosphate and nitrate anions on ammonium-functionalized MCM-48: effects of experimental conditions, *J. Colloid Interface. Sci*., 311(2007), 375-381.
40. A. T. Khadim, T. M. Albayati, N. M. Cata Saady, Desulfurization of actual diesel fuel onto modified mesoporous material Co/MCM-41, *Environ. Nanotechnol. Monit. Manag.*, 17(2022), 100635.
41. S. T. Kadhum, G. Y. Alkindi, T. M. Albayati, Remediation of phenolic wastewater implementing nano zerovalent iron as a granular third electrode in an electrochemical reactor, *Int. J. Environ. Sci. Technol*., 19(2022), 1383-1392.
42. S. T. Kadhum, G. Y. Alkindi, T. M. Albayati, Determination of chemical oxygen demand for phenolic compounds from oil refinery wastewater implementing different methods, *Desalin. Water Treat.*, 231(2021), 44-53.
43. E. H. Khader, R. H. Khudhur, N. S. Abbood, T. M. Albayati, Decolourisation of anionic azo dye in industrial wastewater using adsorption process: investigating operating parameters, *Environ. Process.*, (2023), DOI: 10.1007/s40710-023-00646-7.
44. A. Amari, H.S.K. Alawamleh, M. Isam, M. A. J. Maktoof, H. Osman, B. Panneerselvam, M. Thomas, Thermodynamic investigation and study of kinetics and mass transfer mechanisms of oily wastewater adsorption on UIO-66–$MnFe_2O_4$ as a metal–organic framework (MOF), *Sustain*., 15(2023), 2488.
45. A. Q. Alorabi, M. Azizi, Effective removal of methyl green from aqueous environment using activated residual Dodonaea Viscosa: equilibrium, isotherm, and mechanism studies, *Environ. Pollut. Bioavailab.*, 35(2023), 2168761.
46. H. J. Al-Jaaf, N. S. Ali, S. M. Alardhi, T. M. Albayati, Implementing eggplant peels as an efficient bio-adsorbent for treatment of oily domestic wastewater, *Desalin. Water Treat.*, 245(2022), 226-237.

How to cite this article:
A. E. Mahdi, N. S. Ali, K. R. Kalash, I. K. Salih, M. A. Abdulrahman, T. M. Albayati, Investigation of Equilibrium, Isotherm, and Mechanism for the Efficient Removal of 3-Nitroaniline Dye from Wastewater Using Mesoporous Material MCM-48. Prog. Color Colorants Coat., 16 (2023), 387-398.

PROGRESS
IN COLOR, COLORANTS AND COATINGS

available online @ www.pccc.icrc.ac.ir

Progress in Color Colorants Coating 16 (2023), 399-408

Ministry of Science, Research and Technology
Institute for Color Science & Technology

Synthesis and Characterization of Well-dispersed Zinc Oxide Quantum Dots in Epoxy Resin Using Epoxy Siloxane Surface Modifier

F. Asadi[1], A. Jannesari*[1], A.M. Arabi[2]

[1.] Department of Resin and Additives, Institute for Color Science and Technology, P.O. Box: 16765-654, Tehran, Iran.

[2.] Department of Inorganic Pigments and Glaze, Institute for Color Science and Technology, P.O. Box: 16765-654, Tehran, Iran

ARTICLE INFO

Article history:
Received: 04 Apr 2023
Final Revised: 08 June 2023
Accepted: 10 June 2023
Available online: 11 Sep 2023

Keywords:
ZnO QDs
Surface modification
Transmission electron microscopy
Nanocomposites.

ABSTRACT

Zinc oxide quantum dots were synthesized using poly (dimethyl siloxane) diglycidyl ether terminated, as surface modifiers (SAs) in different concentrations by precipitation method. The epoxy siloxane modifier was chosen in order to improve the compatibility with the polymeric matrix and gain better dispersion. ZnO QDs with size of about 3 nm with optimum properties were synthesized. Structural characteristics and optical properties of synthesized ZnO quantum dots were investigated using Fourier Transform Infrared spectroscopy (FTIR), X-ray diffraction (XRD), photoluminescence (PL) and UV-Vis spectroscopy. They were powdered, purified and finally dispersed in 3 treatment levels in epoxy resin Matrix and they were distributed uniformly in the epoxy resin. The effect of these nanoparticles on the curing process of epoxy resin and 1,3-bis (aminomethyl) cyclohexane (1,3BAC) hardener was investigated using differential scanning calorimetry (DSC). The nanocomposites containing 0.05, 0.1 and 0.15 % ZnO nanoparticles presented respectively 3.6, 15.05, and 12.76 % lower heat flows than the epoxy resin which confirms the barrier effect of these nanoparticles on the activity of epoxy and amine. Prog. Color Colorants Coat. 16 (2023), 399-408© Institute for Color Science and Technology.

1. Introduction

In recent years, semiconductor nanocrystals, also named quantum dots, have attracted a lot of attention due to their unusual optical behavior [1-8]. By controlling the size and structure of quantum dots, their bandgap and emission wavelength can be changed in the infrared to ultraviolet range and they can have a bright and stable emission [8]. Zinc oxide with a wide band gap of 3.37 ev and a critical Bohr radius of about 1.4-3.5 nm is used in many applications including solar cells, sensors, medical applications, and optical diodes [1, 2, 9, 10]. Especially because it is non-toxic and environmentally friendly, widely used in biology and optical imaging [8, 11] and can be used to enhance the resistance of polymers to UV radiation [12-15] However, there are still many challenges regarding their synthesis and cheapening and industrialization, which is why they are used in a limited way in industry [8]. Another major challenge of quantum dots is that they do not have colloidal stability and after a short period of time after synthesis, they undergo the Ostwald ripening and precipitate in reaction medium [11]. Extensive applications require specific nanostructure and in fact needs functionalization and modification of their surface [2, 11, 16-18]. Quantum dots with uniform

---

*Corresponding author: * Jannesari-a@icrc.ac.ir

Doi: 10.30509/pccc.2023.167118.1210

particle size distribution and strong emission can be produced using appropriate surface modifiers during the synthesis process [12, 19]. Stabilization of nanoparticles via organic functionalization, commercially with PMMA, PEG, PVA and Silanes, can be a good strategy to control the agglomeration and surface defects of the nanoparticles [19-21]. However, purified and powdered particles cannot be well dispersed and uniformly distributed in polymer, which limits their use [12]. Zhang et al. used four different materials including 3-mercaptopropyl tri-methoxysilane, polyvinylpyrrolidon, aminopropyl trimethoxysilane and tetraethyl orthosilicate as capping agents to modify the surface of ZnO quantum dots to control their size and proved by TEM that all sizes were below 10 nm [8, 22]. In another work, Liu, used diethylenetriamine (DETA) as ligands to modify the surface of ZnO QDs, it not only passivates the surface defects of ZnO but also suppress the overwhelming electron injection in the QLED [23]. Huang et al. used g-(2,3-epoxypropoxy)-propytrimethoxysilane surface modifier in the synthesis of ZnO QDs. Their synthesized nanoparticles showed very uniform dispersion in epoxy resin and strong luminescence in both dissolved and dry conditions [12]. Wang successfully used Holmium acetylacetonate to create compatibility between zinc oxide quantum dots and epoxy and achieved a uniform dispersion of these nanoparticles with a size of 3 nm in the epoxy substrate and excellent optical properties [24]. In our last work, we investigated the influence of the presence of ZnO QDs synthesized with epoxy siloxane surface modifier on the structural and morphological properties as well as curing behavior of Epoxy Siloxane [25].

In this study, we synthesized zinc oxide quantum dots in the presence of poly (dimethyl siloxane) diglycidylether terminated as surface modifier in four different concentrations via precipitation method. It is assumed that active epoxide groups in the structure of this modifier can create strong physical or chemical bonds with inorganic groups on the surface of ZnO and their compatibility with Matrix leads to good dispersion of QDs in epoxy [20]. Characterization of the synthesized nanoparticles was performed using FTIR, X-ray diffraction, PL and UV-Vis. On the other hand, the effect of these quantum dots on the curing process of epoxy and 1,3-BAC hardener was investigated using DSC. The effect of these nanoparticles on the optical properties of nanocomposite was also investigated. A fairly uniform distribution of these nanoparticles in the epoxy was obtained due to the presence of epoxy groups in the structure of the surface modifier, which made it compatible with the matrix [12].

2. Experimental

2.1. Materials

Zinc acetate dehydrate ($Zn(Ac)_2.2H_2O$,0.99 %), NaOH (99 %,), ethanol (absolute) and n-heptane were supplied from Merck (Germany). Poly (dimethyl siloxane), diglycidyl ether terminated resin (epoxy-siloxane resin) with an average Mn Mw of 800 g/mol and EEW of 490 g/mol was purchased from Sigma-Aldrich (Germany) and used as a surface modifier in the synthesis process of nanoparticles. Bisphenol A based liquid epoxy resin with Epoxide Equivalent Weight (EEW) of 185-192 g/eq was provided by Khuzestan Petrochemical Co., (Iran) and used as a matrix resin in the preparation of nanocomposites. The curing agent was 1,3-Bis (amino methyl) cyclohexane (1,3-BAC) from Sigma-Aldrich (Germany) with Mw of 142.2 g/mol and Amine value of 789 mg KOH/g.

2.2. Synthesis of ZnO quantum dots

ZnO solutions containing 0.02 M NaOH and epoxy-siloxane as surface modifier (SA) at four different amounts (0.1, 0.5, 1 and 2 g) in 50 mL ethanol were heated at 60 °C for 30 min. 0.002 mol (0.37 g) $Zn(Ac)_2.2H_2O$ was directly added to the solution and then heated at 70 °C for 1 h [1]. After that, ZnO QDs were precipitated by n-heptane and the obtained white powder was washed in deionized water and ethanol five times in order to purify the ZnO QDs. Then, they were dried in vacuum for 24 h [1, 2]. The amount of SA was set at 0.1, 0.5, 1 and 2 g which were named as ZQ01, ZQ05, ZQ1 and ZQ2 samples.

2.3. Synthesis of nanocomposites

One of the synthesized ZnO QDs with best performance was selected and added to liquid epoxy resin in four different concentrations, i.e. 0, 0.05, 0.1 and 0.15 % and mixed using sonication method. 1,3-bis (amino methyl) cyclohexane (1,3-BAC) in 1:2 molar ratio used as curing agent. DSC measurements were done using NETZSCH DSC 214 instrument with 4 different hitting rates.

3. Results and Discussion

3.1. Characterization of ZnO quantum dots

3.1.1. Structural studies

X-ray diffraction patterns of ZnO QDs synthesized with different concentrations of SA are shown in Figure 1. There are differences between the patterns that help to choose a sample for making the QDs composite. The main phase of all samples is zinc oxide with hexagonal wurtzite structure (JCPDS No. 01-079-0207). However, some samples show the minor peaks of zinc hydroxide (JCPDS No. 00-001-0360) and event zinc acetate (JCPDS No. 00-001-089). Because of the minimum amounts of secondary phases, the optimum condition is seen in ZQ05. In ZQ05, the purest zinc oxide structure is seen, indicate that all precursors have been completely consumed and no by-products are formed. The concentration of siloxane SA has significant influence on the intensity and full width of half maximum (FWHM) of diffraction peaks. Broadening in diffraction peaks in ZQ01, ZQ05 and ZQ1 can be the result of size reduction effects due to organic functionalization and crystallinity reduction [1, 3-7]. The optimum concentration of SA is needed to help the formation of pure zinc oxide. Excess (ZQ1 and ZQ2 samples) or less (ZQ01) amounts of SA leads to formation of zinc acetate and zinc hydroxide beside the zinc oxide structure. In the other words, less amounts of SA leads to lack of coverage of functional groups of SA and excess amounts of that moves the system towards micelle formation as a rival to quantum dots.

3.1.2. Chemical composition

Fourier Transform infrared spectrum (FTIR) of ZnO QDs prepared with different concentrations of siloxane SA showed a peak at 450 cm^{-1} attributed to the vibration of Zn-O bonds. Strong bonds at 817 and 1200 cm^{-1} correspond to epoxide groups and Si-O-Si, respectively, in all the samples [1, 7, 12]. The intensity of these peaks increased with increasing the SA concentration (Figure 2). A broad peak at ~ 3500 cm^{-1} and a shoulder at 1570 cm^{-1} corresponds to OH stretching and bending vibrations, respectively. The peaks at 3500 cm^{-1} can also belonged to the Zn(OH)$_2$.

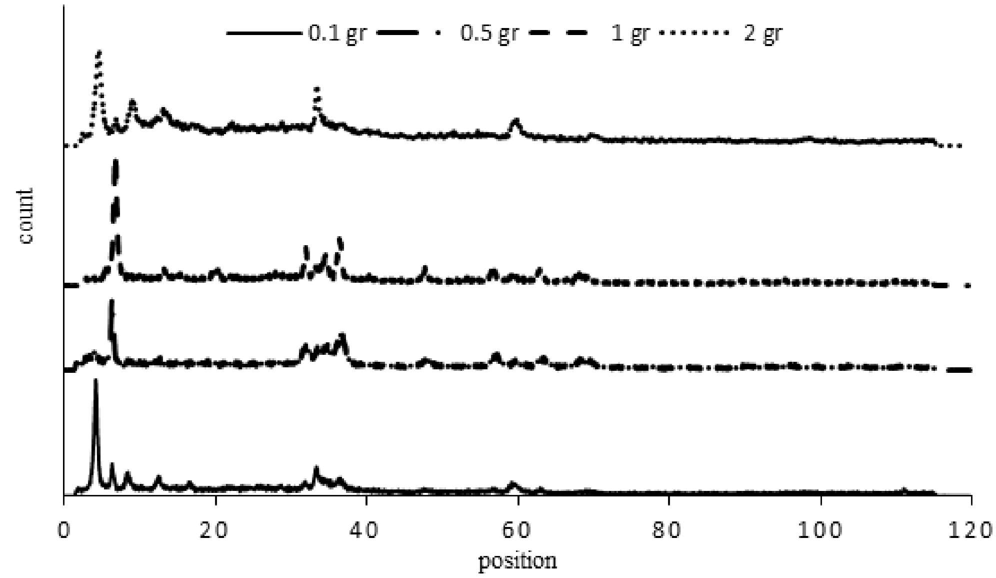

Figure 1: X-ray diffraction patterns of the synthesized ZnO particles in the presence of different amounts of SA.

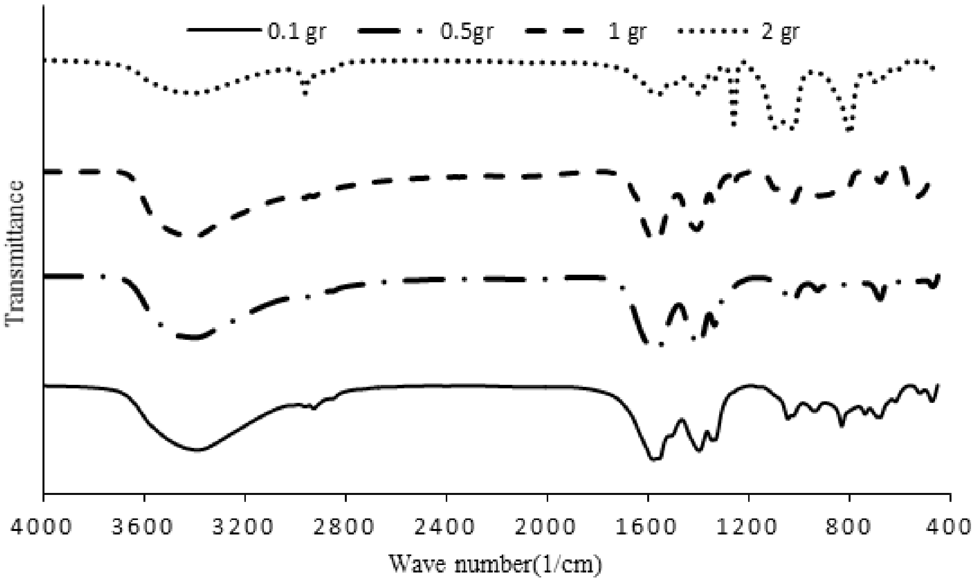

Figure 2: FTIR of the synthesized ZnO particles in the presence of different amounts of SA.

3.1.3. Photoluminescence properties

Figure 3 shows PL spectra of ZnO QDs with different SA concentrations. Some authors believe that PL radiation is associated with surface defects, it is quite clear that changing in the ligand graft density (ZnO: SA ratio) will change the size of the clusters [10, 24]. Generally, by reducing the QDs particle size, the quantum confinement switches the energy of the conduction and valance bands, and leads to a blue shift [4, 13]. Except ZQ2 sample, all specimens in the visible photoluminescence region contain a strong cyan emission peak. The sample ZQ2 showed a blue peak in the visible region, which is the edge emission values of ZnO bulk. It seems that the ZQ2 sample is not in the quantum size region (its size is rather than Bohr radius). The ZQ05 sample exhibits the highest emission intensity which can be originated from the formation of the purest zinc oxide structure [13, 21]. In the other samples, zinc hydroxide or zinc acetate minor phases (Figure 1) act as a competitor for electron – hole recombination. On the other hand, the electron excited by the high energy photons migrates to the zinc hydroxide or acetate instead of radiative transition to relax to the ground state. So, the reduction of luminescence efficiency can be related to the non-radiative transition of electron towards zinc hydroxide or acetate and the conversion to thermal energy [26].

3.1.4. Morphological studies

Morphology of the synthesized nanoparticles and the samples synthesized with different concentrations of surface modifier is evaluated using SEM, as shown in Figure 4. According to the Figure, ZQ01 and ZQ05 have particles less than 10 nm in size, which cannot be accurately measured due to the resolution limitations of the SEM images. On the other hand, the ZQ1 and ZQ2 samples have larger agglomerated particles. In order to specify the shape and size of ZnO QDs nanoparticles, TEM image of the ZQ05 (which was the best candidate for making nanocomposite) is shown in Figure 5. As seen, the particles are relatively separate and are mostly under Bohr radius (2.34 nm) [13]. Because of the existence of a kind of polymeric coverage from SA, QDs seem to be spherical and are partially agglomerated. ZnO QDs are mono-dispersed with an average particle size of less than 3 nm that is in the range of Bohr radius of ZnO and is in good agreement with other zinc oxide quantum dots synthesized with different surface modifiers by other researchers, which are in the approximate range of about 2 to 8 nm [10, 15, 24].

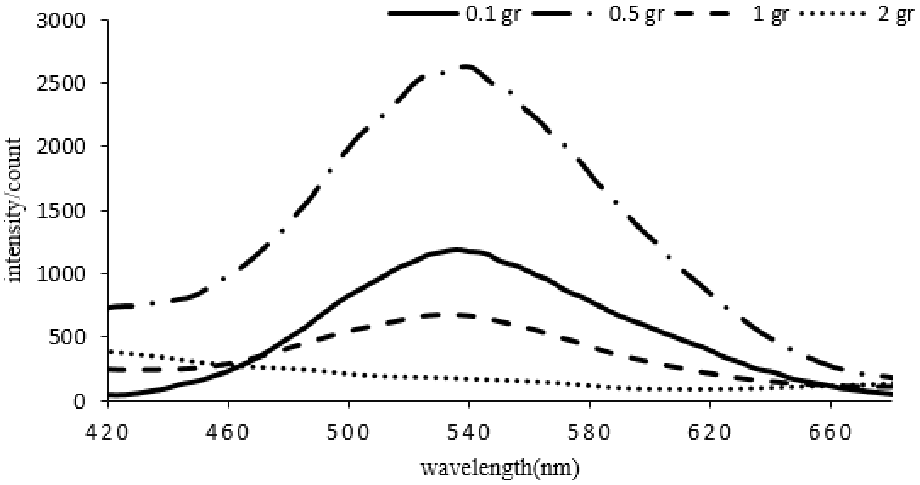

Figure 3: PL spectra of the synthesized ZnO particles in the presence of different amounts of SA.

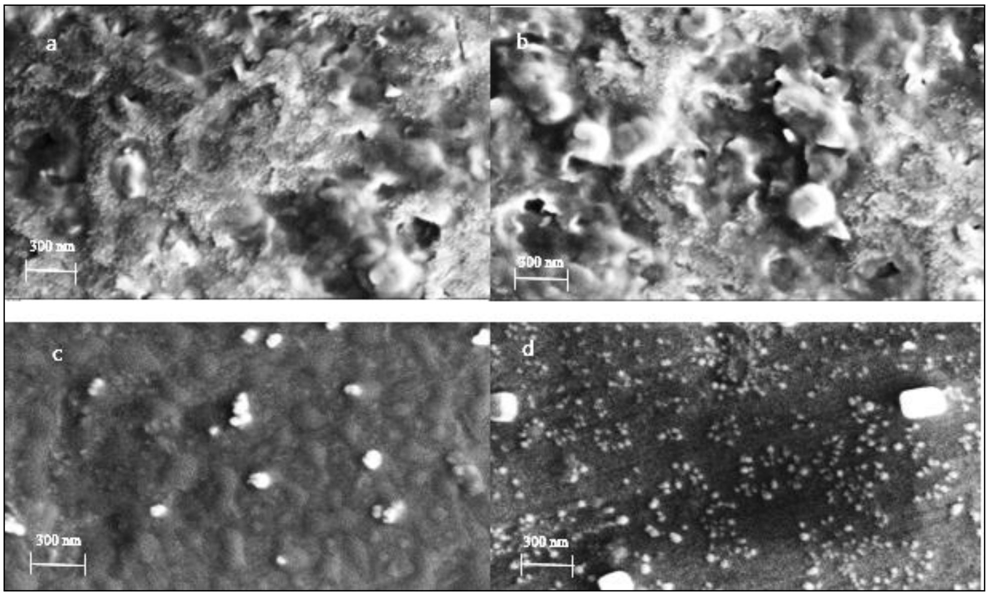

Figure 4: SEM images of the synthesized ZnO particles containing 4 different SA values a) 0.1gr (ZQ01), b) 0.5gr (ZQ05), c) 1gr (ZQ1) d) 2gr (ZQ2).

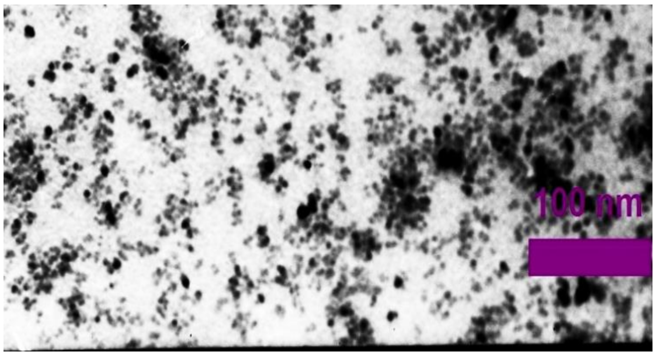

Figure 5: TEM images of the ZQ05 sample.

3.1.5. UV-Visible absorption spectra

The UV-Visible adsorption spectra of ZQ01, ZQ05, ZQ1 and ZQ2 are shown in Figure 6. As can be seen, the efficient UV emission shifts to higher energies with a sharp peak by decreasing the size of ZnO QDs [4]. The quantum dot samples have higher interaction with the incident light and show the exact position of bandgap as the significant changing the slope in the curves (shown by the number on the curves). So, the ZQ01 and ZQ05 sample are clearly in the quantum confinement region with the 4.13 and 3.87 eV bandgaps, respectively. The bandgap values are significantly wider than the bulk ZnO (3.2 eV) [13, 21, 26, 27].

3.2. Characterization of nanocomposites

3.2.1. Thermal Analysis

ZQ05 (ZnO QDs with 0.5 g surface modifier) which represented better features were chosen and added to liquid epoxy resin to investigate their influence on final nanocomposite behavior. Nanocomposites with four ZQ05 concentrations, i.e. 0, 0.05, 0.1 and 0.15 %, were prepared and their curing reactions with 1,3-BAC were studied by DSC. According to the DSC results shown in Figure 7 and Table 1, incorporation of ZnO QDs into the epoxy resin exhibited a reduction in the heat released from curing reaction. The nanocomposites containing 0.05, 0.1 and 0.15 % ZnO QDs presented 3.6, 15.05, and 12.76 % lower enthalpy values than the neat resin matrix, respectively. The ZnO QDs can cause a barrier effect and decrease the probability of reaction functional groups of amine and epoxy. This phenomenon occurred with increasing the concentration of ZnO QDs up to 0.1 %, after which nanoparticles begin to agglomerate and lose their function.

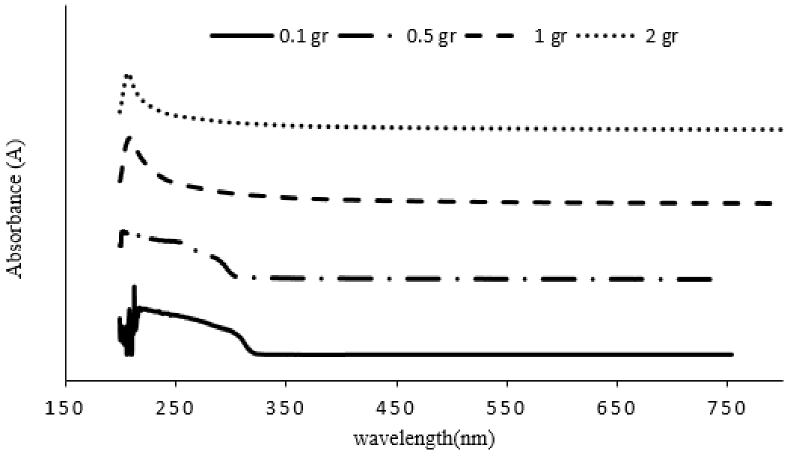

Figure 6: UV-Visible absorption spectra of the synthesized ZnO particles in the presence of different amounts of SA.

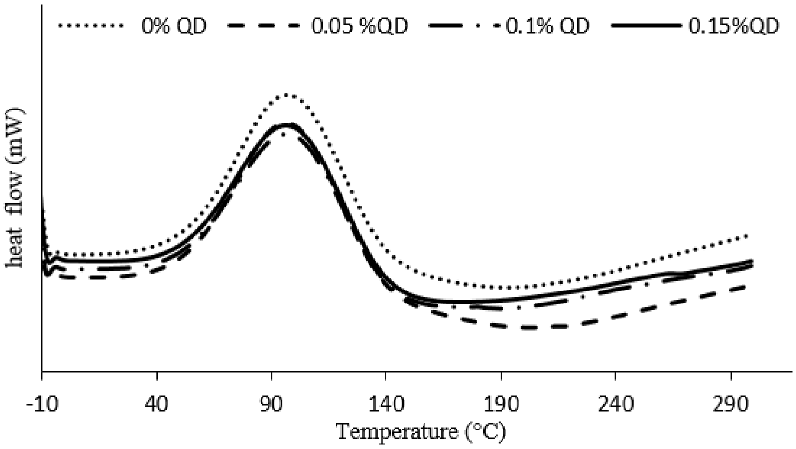

Figure 7: DSC curves of the epoxy/ZnO QD nanocomposites in the presence of different amounts of ZnO QDs.

Table 1: DSC extracted data for the epoxy/ZnO QD nanocomposite.

sample	T_o (°C)	T_m (°C)	T_e (°C)	ΔH (J/g)	r max (1/min)	T (r max) (°C)
0 % QD	54.3	95.7	137.1	174.7	1.72264	97.12144
0.05 % QD	58.2	95.0	136.5	168.4	1.76668	98.27
0.1 % QD	58.5	95.3	142.2	148.4	1.82036	97.41652
0.15 % QD	55.7	95.1	137.1	152.4	1.86957	97.11455

T_o is the onset temperature, T_e is the end-point temperature and T_m is the peak temperature.

3.2.2. Optical properties

Optical transmittance spectra of crystalline ZnO QDs in the vast region from 200 to 1100 nm are shown in Figure 8. For accurate exploration, three regions, i.e. UV, Visible, and NIR regions, were evaluated separately shown in Figures 9-12 and Tables 2 and 3. In UV region (300-380 nm), nanocomposite containing 0.15 % ZnO QDs showed the highest absorption. ZnO QDs are UV absorbent and their higher concentration leads to less transmission of UV irradiation. In visible region, different concentrations of QDs have no effect on the amount of light transmission. And finally in NIR region, the presence of ZnO QDs results in the reduction of infrared irradiation transmission. In other words, ZnO QDs increase heat absorption. The results are quite consistent with DSC results. ZnO QDs which absorb heat will reduce the total released heat during curing reaction. At the same time, sample containing 0.1 % ZnO QDs that has the highest heat absorption, showed the lowest amount of heat released from curing reaction.

Table 2: IR transmittance of the epoxy/ZnO QD nanocomposite.

Nanocomposite	Transmittance (%)
0 % QD	88
0.05 %QD	86
0.1 % QD	84
0.15 %QD	86

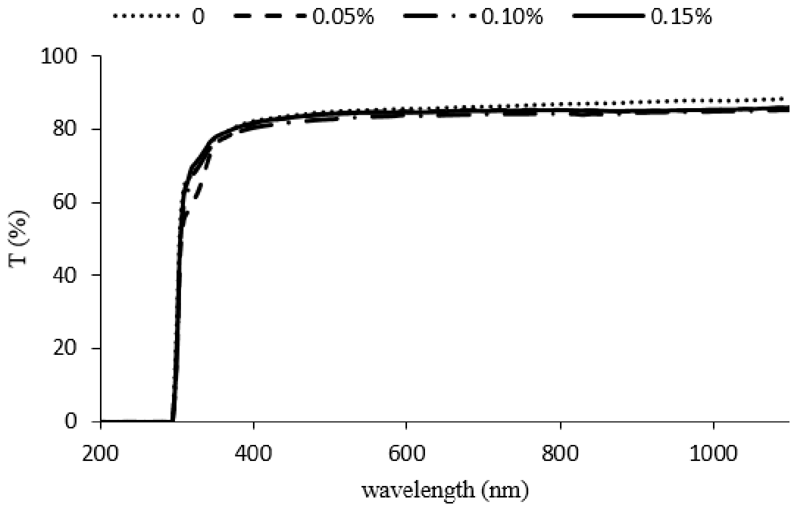

Figure 8: Optical transmittance spectra of the epoxy/ZnO QD nanocomposites in the presence of different amounts of ZnO QDs.

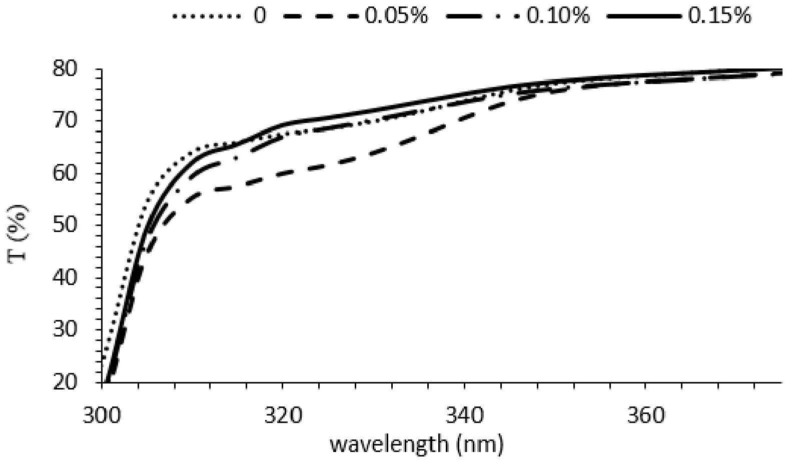

Figure 9: UV transmittance spectra of the epoxy/ZnO QD nanocomposite in the presence of different amounts of ZnO QDs.

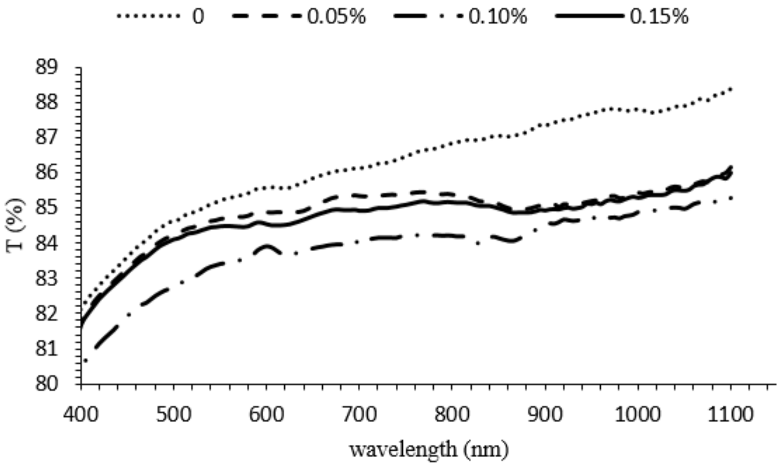

Figure 10: IR transmittance spectra of the epoxy/ZnO QD nanocomposite in the presence of different amounts of ZnO QDs.

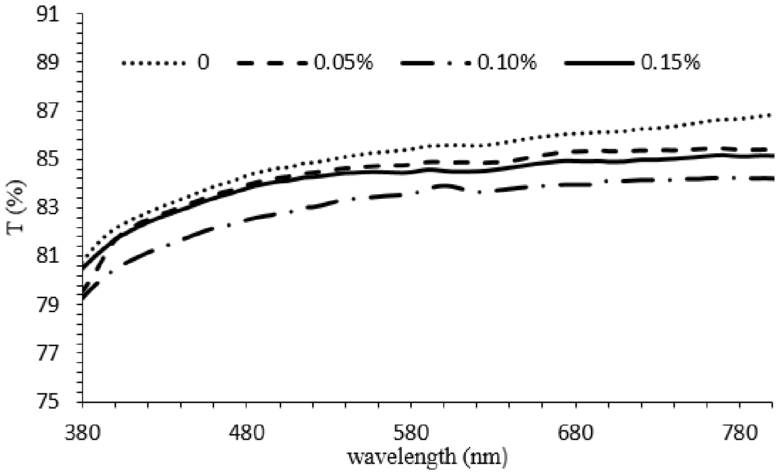

Figure 11: Light absorbance spectra of the epoxy/ZnO QD nanocomposite in the presence of different amounts of ZnO QDs.

Figure 12: The image of transparency of the epoxy/ZnO QD nanocomposite films.

Table 3: Type and characterization of some surface modifiers used in the ZnO QD preparation.

Ref	Surface modifier	Size (nm)	Other effect
23	diethylenetriamine (DETA)	Lower than 20	The PL spectra of QDs on different substrates all present a redshift and decreased
11	different hydroxylated polymers	3.8 to 5	Fluorescence enhancement occurred when ZnO QDs were synthesized in the presence of the hydroxylated polymers
18	siloxane	4.1 ± 0.5	The broad-band visible PL, which originates from surface or defect states, becomes much weaker and undergoes a red-shift of 10 nm and a gradual enlargement compared to starting ZnO@AEPTE QDs
24	Ho(AcAc)3	3.0 ± 0.5	Good dispersion in epoxy and the emission intensity and the UV absorptivity increased.
Our Work	poly (dimethyl siloxane) diglycidyl ether terminated,	About 3	Good dispersion in epoxy and increased the absorbance of UV radiation.

4. Conclusions

In the past decades, the use of quantum dots has expanded considerably, given their desirable propertie. The main problem that limits their consumption is the fact that they cannot be uniformly dispersed in polymeric matrices. Application of suitable surface modifier to enhance the compatibility with polymeric matrix can be a good idea. Epoxy-siloxane surface modifiers led to the synthesis of stable QDs, but their concentration is a key point. In order to investigate the effect of surface modifier concentration on the final properties, four different amounts of QDs were used. ZnO QDs synthesized by 0.0125 M epoxy-siloxane are about 3 nm in size and have blue light emission. These QDs were distributed uniformly in epoxy resin and enhanced its properties. They showed no effect on the transparency of the epoxy film but increased the absorbance of UV radiation. They also played a catalytic role in curing reaction and increased its rate, leading to the incomplete curing of the epoxy.

5. References

1. J. J. Huang, Y. Bin Ye, Z. Q. Lei, X. J. Ye, M. Z. Rong, M. Q. Zhang, Highly luminescent and transparent ZnO quantum dots–epoxy composite used for white light emitting diodes, *Phys. Chem. Chem. Phys*., 16(2014), 5480..
2. T. Jin, D. Sun, J. Y. Su, H. Zhang, H. J. Sue, Antimicrobial efficacy of zinc oxide quantum dots against *Listeria monocytogenes, Salmonella* enteritidis, and *Escherichia coli* O157:H7, *J. Food Sci*., 74(2009) M46-M52.
3. V. Muşat, A. Tăbăcaru, B. Ş. Vasile, V. A. Surdu, Size-dependent photoluminescence of zinc oxide quantum dots through organosilane functionalization, *RSC Adv*., 4(2014), 63128-63136.
4. K. F. Lin, H. M. Cheng, H. C. Hsu, L. J. Lin, W. F. Hsieh, Band gap variation of size-controlled ZnO quantum dots synthesized by sol–gel method, *Chem. Phys. Lett*., 409(2005), 208-211.
5. L. Zhang, L. Yin, C. Wang, N. lun, Y. Qi, D. Xiang, Origin of visible photoluminescence of ZnO quantum

dots: defect-dependent and size-dependent, *J. Phys. Chem. C.*, 114(2010), 9651-9658.

6. T. J. Jacobsson, T. Edvinsson, Absorption and fluorescence spectroscopy of growing ZnO quantum dots: size and band gap correlation and evidence of mobile trap states, *Inorg. Chem.*, 50(2011), 9578-9586.
7. X. J. Huang, X. F. Zeng, J. X. Wang, J. F. Chen, Transparent dispersions of monodispersed ZnO nanoparticles with ultrahigh content and stability for polymer nanocomposite film with excellent optical properties, *Ind. Eng. Chem. Res.*, 57(2018), 4253-4260.
8. A. K. Verma, ZnO quantum dots a novel nanomaterial for various applications: Recent advances and challenges, Indian *J. Biochem. Biophys.*, 59(2022) 1190-1198.
9. S. Repp, S. Weber, E. Erdem, Defect evolution of nonstoichiometric ZnO quantum dots, *J. Phys. Chem. C*. 120(2016), 25124-25130.
10. T. Zou, X. Xing, Y. Yang, Z. Wang, Z. Wang, R. Zhao, X. Zhang, Y. Wang, Water-soluble ZnO quantum dots modified by (3-aminopropyl) triethoxysilane: The promising fluorescent probe for the selective detection of Cu^{2+} ion in drinking water, *J. Alloys Compd.*, 825(2020), 153904.
11. L. San José, O. García, I. Quijada-Garrido, M. López-González, RAFT hydroxylated polymers as templates and ligands for the synthesis of fluorescent ZnO quantum dots, *Nanomaterials*., 12(2022), 3441.
12. S. Li, Z. Sun, R. Li, M. Dong, L. Zhang, W. Qi, X. Zhang, H. Wang, ZnO nanocomposites modified by hydrophobic and hydrophilic silanes with dramatically enhanced tunable fluorescence and aqueous ultrastability toward biological imaging applications., *Sci. Rep.*, 5(2015), 8475.
13. J. Oliva, L. Diaz-Torres, A. Torres-Castro, P. Salas, L. Perez-Mayen, E. De la Rosa, Effect of TEA on the blue emission of ZnO quantum dots with high quantum yield, *Opt. Mater. Express*., 5(2015), 1109.
14. Y. Q. Li, S. Y. Fu, Y. Yang, Y. W. Mai, Facile synthesis of highly transparent polymer nanocomposites by introduction of core–shell structured nanoparticles, *Chem. Mater.*, 20(2008), 2637-2643.
15. Y. Yang, W. N. Li, Y. S. Luo, H. M. Xiao, S. Y. Fu, Y. W. Mai, Novel ultraviolet-opaque, visible-transparent and light-emitting ZnO-QD/silicone composites with tunable luminescence colors, *Polymer* (Guildf)., 51(2010), 2755-2762.
16. R. L. B. Cabral, F. M. F. Galvão, K. K. O. de Souto Silva, B. H. S. Felipe, N. F. de Andrade Neto, P. B. de Almeida Fechine, A. Zille, S. Kim, J. H. O. do Nascimento, Surface modification of ZnO quantum dots coated polylactic acid knitted fabric for photocatalytic application, *J. Appl. Polym. Sci.*, 139(2022), 482-496.
17. M. A. V. Garrido, M. Pacio, A. Pacio, M. C. Portillo, O. P. Moreno, H. Jaurez, Analysis of blue (BE), green (GE), yellow (YE), and red (RE) emission band in ZnO quantum dots, *Optik (Stuttg)*, 271(2022), 170102.
18. A. Schejn, L. Balan, D. Piatkowski, S. MacKowski, J. Lulek, R. Schneider, From visible to white-light emission by siloxane-capped ZnO quantum dots upon interaction with thiols, *Opt. Mater. (Amst)*, 34(2012), 1357-1361.
19. C. S. Garoufalis, Z. Zeng, G. Bester, I. Galanakis, D. Hayrapetyan, E. Paspalakis, S. Baskoutas, Excitons in ZnO quantum dots: the role of dielectric confinement, *J. Phys. Chem. C.*, 126(2022), 2833-2838.
20. V. A. Fonoberov, K. A. Alim, A. A. Balandin, F. Xiu, J. Liu, Photoluminescence investigation of the carrier recombination processes in ZnO quantum dots and nanocrystals, *Phys. Rev. B.*, 73(2006), 1-9.
21. D. Haranath, S. Sahai, P. Joshi, Tuning of emission colors in zinc oxide quantum dots, *Appl. Phys. Lett.*, 92(2008), 148-159.
22. P. Zhang, W. Liu, ZnO QD@PMAA-co-PDMAEMA nonviral vector for plasmid DNA delivery and bioimaging, *Biomaterials*., 31(2010), 3087-3094.
23. D. Zhang, Y. H. Liu, L. Zhu, Surface engineering of ZnO nanoparticles with diethylenetriamine for efficient red quantum-dot light-emitting diodes, *IScience*., 25(2022), 105111.
24. M. Yu, W. Yang, Q. Zhang, C. Wong, W. Ding, L. Wang, X. Yang, Holmium acetylacetonate, a compatibilizer between ZnO quantum dots and epoxy resin, *Opt. Mater. Express*, 6(2016), 1757-1767.
25. F. Asadi, A. Jannesari, A. Arabi, Progress in organic coatings epoxy siloxane / ZnO quantum dot nanocomposites : Model-fi tting and model-free approaches to kinetic analysis of non-isothermal curing process, *Prog. Org. Coat.*, 135(2019), 270-280.
26. S. Banerjee, P. Bhattacharyya, C. K. Ghosh, Charge carrier–LO phonon interaction in ZnO nanostructures: effect on photocatalytic activity and infrared optical constants, *Appl. Phys. A Mater. Sci. Process.*, 123(2017), 1-9.
27. G. Jain, C. Rocks, P. Maguire, D. Mariotti, One-step synthesis of strongly confined, defect-free and hydroxy-terminated ZnO quantum dots, *Nanotechnology*., 31(2020), 215707.

How to cite this article:
F. Asadi, A. Jannesari, A.M. Arabi, Synthesis and Characterization of Well-dispersed Zinc Oxide Quantum Dots in Epoxy Resin Using Epoxy Siloxane Surface Modifier Prog. Color Colorants Coat., 16 (2023), 399-408.

PROGRESS
IN COLOR, COLORANTS AND COATINGS

available online @ www.pccc.icrc.ac.ir
Progress in Color Colorants Coating 16 (2023), 409-415

Ministry of Science, Research and Technology
Institute for Color Science & Technology

Analysis of Nitrogen Ion Implantation on Corrosion Inhabitation of Zirconium Nitride Coated 304 Stainless Steel and Correlation with Nano-strucrure and Surface Hardness

M. Karimi, A. R. Grayeli*
Physics and Accelerators Research School, Nuclear Science & Technology Research Institute, P.O. Box: 11365-3486, Tehran, Iran.

ARTICLE INFO

Article history:
Received: 11 Apr 2023
Final Revised: 06 July 2023
Accepted: 08 July 2023
Available online: 17 Sep 2023

Keywords:
Zirconium thin film
Ion implantation
Corrosion
Hardness
Stainless steel

ABSTRACT

One of the common methods to improve and change the structural, wear, and corrosion characteristics of materials is to create a resistant thin film using the physical vapor deposition process. Various ions are substituted or interspersed on the surface of metal or non-metal parts using accelerators. This article investigates the structural, corrosion, and mechanical properties (hardness) of zirconium nitride coatings prepared by ion beam sputtering and nitrogen ion implantation on 304 stainless steel. For this purpose, a coating of zirconium with a thickness of 100 nm has been deposited on 304 stainless steel by the ion beam sputtering method. Nitrogen ion implantation was performed at a temperature of 400 K and a dose of 5×10^{17} N^+ cm^{-2} at energies of 10, 20, 40, and 80 keV. The crystallographic investigation, hardness, corrosion tests in 0.6 M NaCl solution, and SEM were done for different samples. The correlation between the test results, considering the increase in the implantation energy, introduced the optimal energy of 40 keV to make the sample with the highest degree of corrosion resistance and hardness. Prog. Color Colorants Coat. 16 (2023), 409-415© Institute for Color Science and Technology.

1. Introduction

The use of thin films for protection has been of interest to humans for a long time. Many modern and complex electronic and optical parts are made in thin film [1-4]. Over the past few years, transition metal nitrides have emerged as the most promising coating options for enhancing the corrosion resistance of less noble materials like steel. Despite possessing beneficial properties such as chemical stability, hardness, good adhesion to steel substrates, and attractive colors, metal nitrides coatings tend to exhibit poor corrosion resistance due to the presence of certain imperfections, including pores, cracks, pinholes, and transient grain boundaries. Physical vapor deposition techniques, in particular, often result in a high density of microscopic defects within the coating structure, making the film vulnerable to corrosion attack. Essentially, the presence of these defects creates paths that allow corrosive media to penetrate the substrate, compromising the system's corrosion resistance. Consequently, researchers have explored various techniques to improve the coatings' quality [5-8].

Recently, compared to other metal nitrides, zirconium nitride thin film has been used the most in industrial fields, such as hard coatings, corrosion-resistant coatings, and creating penetration barriers in microelectronic devices. The formation of zirconium nitride coatings is more complex than TiN or CrN films

---

*Corresponding author: * a_ grayli@yahoo.com

Doi: 10.30509/pccc.2023.167128.1213

because zirconium has a high melting point and low vapor pressure and is highly susceptible to oxygen and carbon pollution. Fewer studies have been done about zirconium nitride compared with nitride films of other transition metals [9-11].

To deposit zirconium nitride on different substrates, a long time and high temperature are required; therefore, various methods of physical vapor deposition (PVD) have been used to increase the deposition rate and lower the temperature [12, 13]. In 2003, Pilloud and Dehlinger fabricated a zirconium nitride film through magnetron sputtering using an Alcatel SCM650 sputtering system. They investigated the effect of changing substrate bias, substrate temperature, and nitrogen gas flow on structural and mechanical properties [14]. In 2003, Hu and Li deposited zirconium nitride on the glass substrate by a magnetron sputtering with different nitrogen gas flows in an argon and nitrogen gas mixture. They showed that if the flow of nitrogen (F (N_2)) is between 5 and 12 %, the film with NaCl structure (fcc) with the preferred direction is formed. ZrN_x structure does not change with increasing nitrogen flow from 12 to 24 %, and ZrN(111) peak is the preferred direction. When F(N_2) is more than 24 %, no more peak is observed, which means that ZrN_x films are formed in an amorphous form [15]. Han, Lee, and colleagues subjected zirconium to nitrogen ion implantation. By examining the wear test results, they found that with the process of nitrogen implantation and formation of zirconium nitride, the wear of zirconium decreases with the increase of the ion dose, and the wear also decreases [16].

The first step of this research involved depositing thin films of zirconium onto 304 steel substrates using an ion-sputtering device. Then a thin zirconium nitride film was made using an ion implantation accelerator with a constant ion dose at different energies. In the following, its structural properties, corrosion behavior, and SEM analysis after the corrosion test have been investigated as a function of implantation energy. The deposition techniques used are chosen due to their ability to precisely control the thickness of the coating and produce a uniformly coated surface with superior adhesion.

2. Experimental

In this study, Zirconium nitride thin films with a thickness of 100 nm were deposited on AISI 304 stainless steel substrates by ion beam sputtering (IBS) at room temperature. Table 1 [17] provides information on the chemical composition and element abundance of the stainless steel alloy employed in the study. Ion beam sputtering is a highly effective coating method that uses ion beams to apply materials onto a substrate's surface. The schematic diagram of the IBS for the deposition of ZrN films is shown in Figure 1. This study accelerated Ar ions toward a Zr target at a fixed energy of 2.2 keV and a 25 mA/cm^2 current throughout the experimental process. The substrate temperature during deposition was consistently maintained at 400 °C. For a more detailed overview of the deposition conditions, please refer to Table 2. The purity of the zirconium target used in the experiment was 99.98 %. The deposition process was carried out in an advanced (E19 A3 Edwards, England) coating plant, which maintained a base pressure of 2×10^{-5} mbar. A quartz crystal deposition rate controller (Sigma Instruments, SQM-160, USA) was positioned close to the substrates to measure the deposition rate precisely.

To safeguard against scratching and oxidation, the production factory shielded the stainless steel substrates with a protective polyethylene sheet. The sheet was removed by soaking the substrates in ethanol, which were cut to a size of 20 × 20 × 1 mm. Before deposition, all substrates underwent a thorough ultrasonic cleaning process in heated acetone and ethanol. Nitrogen ion implantation of the samples was done at a temperature of 400 °C, a dose of 5×10^{17} N^+/cm^2, and four different energies of 10, 20, 40, and 80 keV.

Table 1: Chemical composition and abundances (%) of different elements in 304 stainless steels [17].

SS Type	Fe	Cr	Ni	Mn	Si	C	P	S
SS(304)	66-71	18-20	8-10.5	2	1	0.08	0.045	0.03

Table 2: The deposition conditions for zirconium nitride thin films by ion beam sputtering.

Deposition parameters specifications	
Target	Zirconium
Sputtering gas	Argon
Base pressure (mbar)	2×10^{-5}
Working Pressure (mbar)	4×10^{-3}
Substrate temperature (^{o}C)	400
Electron beam current (mA)	25
Acceleration voltage (kV)	2.2
Deposition time (min)	40
N^+ dose (N^+/cm^2)	5×10^{17}
Implantation energy (keV)	10, 20, 40, 80

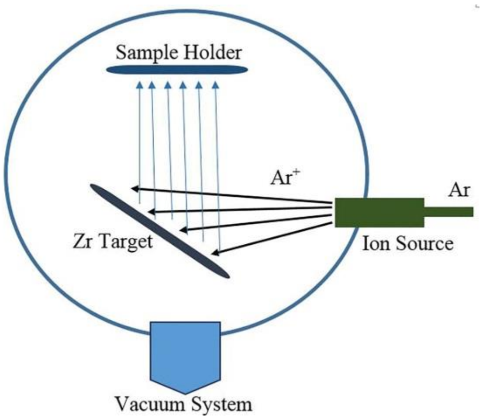

Figure 1: Schematic diagram of the Ion Beam Sputtering system.

The crystallographic structure of the thin films was analyzed using a STOE model STADI MP Diffractometer from Germany, which employed CuKα radiation and used a step size of 0.01° with a count time of 1.0 s per step. The surface physical morphology and nanostructure were characterized using a scanning electron microscope (SEM: LEO 440i, England. The hardness of the samples was determined by a Vickers microhardness tester (Leitz Hardness Tester). A weight of 25 g was used for applying a force equal to 25.254×10^{-4} N on the surface. The electrochemical behavior of the samples was assessed using the potentiodynamic polarization method and device (IVIUM-Compact-State 20250 model). A specially designed holder was used to ensure precise measurements, exposing only a surface area of 1±0.05 cm^2 to the corrosive environment. The test medium consisted of a 0.6 M NaCl solution, with Ag/AgCl and platinum electrodes as a reference and auxiliary electrodes, respectively. The samples produced were utilized as working electrodes in the electrochemical cell. All potentials used were expressed relative to V_{OCP}, with the starting potential set at -400 mV relative to V_{OCP}.

3. Results and Discussion

3.1. Crystal structure analysis

The XRD patterns of the untreated and coated samples with different implantation energies are shown in Figure 2. As expected, three iron peaks related to 304 steel are observed as substrate peaks in the spectrum of samples. Zirconium nitride peaks are observed in the sample produced by the implantation process with 10 keV energy. As it is known, ZrN(111) peak has the highest intensity. Therefore, the preferred direction in the film belongs to this peak. In this sample, zirconium nitride can also be seen on peaks of (200), (220), (222), and (311).

Increasing the implantation energy to 20 keV, increases the intensity of the peak belonging to ZrN(111). This increase is also observed in other zirconium nitride peaks. Also, increasing the implantation energy to 40 keV, increases the intensity of the peak in the preferred direction (111). The intensity of the peaks related to the (200), (220), (311), and (222) directions has been increased compared to the previous sample. By increasing the implantation energy to 80 keV, the intensity of the peak belonging to the (111) peak of zirconium nitride has decreased significantly. For the other peaks, the intensity decrease is visible. In other words, increasing the implantation energy to 80 keV has resulted in the disruption of the arrangement of the crystal plates, leading to a reduction in the level of crystallization.

By comparing the peaks, it is concluded that by increasing the implantation energy up to 40 keV, the intensity of the zirconium nitride peak or the degree of crystallization has increased, reaching its maximum value for 40 keV energy. However, at the maximum energy of 80 keV, the intensity of the zirconium nitride peaks decreases and reaches its lowest value, and the degree of crystallization decreases.

By using Scherer's law and the diffraction pattern of different samples, it is possible to calculate the crystal size (Eq. 1):

$$d=\frac{k\,\lambda}{D\,\cos\theta} \tag{1}$$

Whee d: the crystal size, λ: wavelength, D: Full width at half maximum(FWHM), θ: Bragg angle, k: constant value 0.9 [10].

The crystal size of the samples for different amounts of implantation energy is calculated and given in Table 3. Increasing the implantation energy up to 40 keV makes the crystal size larger. The crystal size has decreased for the sample produced at the highest implantation energy, equivalent to 80 keV.

3.2. Hardness measurement

The samples produced at different implantation energies were studied to check the mechanical properties, including hardness. Table 3 exhibits implantation energy's influence on the produced samples' hardness. The hardness of the samples deposited on 304SS was measured using a Vickers microhardness tester and calculated using the following equation (Eq. 2):

$$H_v=2\cos 22^{o}\frac{F}{l_v^2}=1.854\frac{F}{l_v^2}\,\mathrm{kg/mm^2} \tag{2}$$

Where l_v is the diameter of the rhombus or pyramid, and F is the weight mass [1].

The measured values for the samples can be used as long as the indentation rate is about one-tenth or less than the thickness of the film so that the hardness of the sample does not affect the hardness of the combination of the film and the substrate.

Considering the constant conditions of the process in all the samples, a weight of 25 grams was used. As seen in Table 3, the hardness increases and then decreases by increasing implantation energy. By increasing the implantation energy up to 40 keV, initially, the hardness increased, and for the maximum implantation energy of 80 keV, the hardness of the sample decreased.

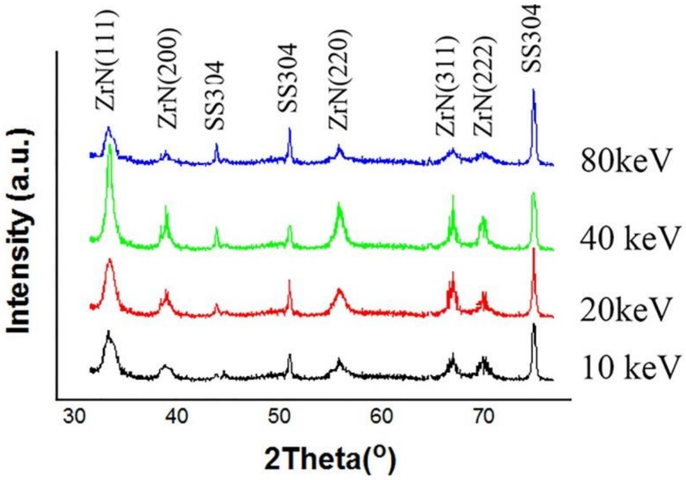

Figure 2: The crystallographic pattern of different samples produced at different implantation energies.

Table3: Calculated crystal size for (111) preferred direction and hardness of different samples.

Implantation energy (keV)	10	20	40	80
Crystal size (nm)	28	54	76	22
Film hardness	362	454	561	417

Table 4: Corrosion parameters of samples produced on 304SS substrates.

Sample		Energy (keV)	Corrosion current density (µA cm^{-2})	Corrosion potential (V vs. SCE)
304 SS		---	17.7828	-0.363
Implanted samples	1	10	0.4897	-0.161
	2	20	0.1862	-0.017
	3	40	0.0194	0.020
	4	80	4.3651	-0.227

3.3. Potentiodynamic polarization

Potentiodynamic curves of the bare 304 stainless steel substrates and those implanted at various energies of 10, 20, 40, and 80 keV are shown in Figure 3. The polarization plot shows that the deposition of ZrN on the stainless steel substrate improves its corrosion resistance. Figure 4 shows that the polarization plot of treated 304SS samples has shifted towards lower corrosion current density and higher corrosion potential, which indicates that corrosion protection has improved for these samples. As can be seen in Table 4, for the 304SS sample that has been implanted in 40 keV, the optimal value of corrosion current density and corrosion potential were obtained as 0.0194 µA/cm^2 and 0.020 V vs SCE, respectively; in contrast, these values for bare 304SS substrate were obtained 17.7828 µA/cm^2 and -0.363 V vs SCE.

For optimal measured hardness and maximum corrosion resistance, a critical value of 40 keV is observed. The XRD results also showed that the intensity of ZrN(111) was highest at this implantation energy. Therefore, it can also be concluded that the volume of zirconium nitride formed on this sample is more significant than that produced at lower and higher energies. Therefore, all of the above discussions point to correlations between the results reported in this study.

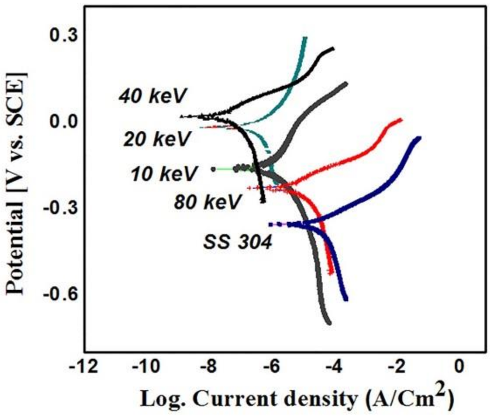

Figure 3: Potentiodynamic polarization curves for 304SS and Zr/304SS samples implanted at different energies.

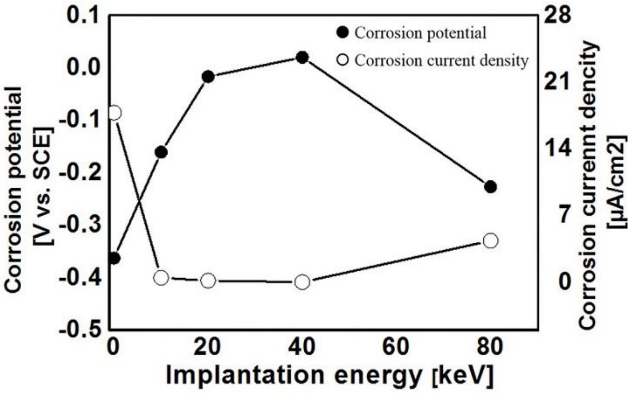

Figure 4: Variations of corrosion potential and corrosion current density as a function of implantation energy for 304SS and Zr/304SS samples implanted at different energies.

3.4. SEM Analysis

Figure 5 presents the surface morphologies of the implanted samples at different implantation energy and the untreated 304 stainless steel substrate after undergoing corrosion tests. The uncoated substrate (Figure 5a) displays obvious signs of corrosion attack and dissolution distributed across the sample's surface. However, the SEM images of implanted samples show different morphologies with varying types and sizes of corrosion effects, such as pits, cracks, peel-offs, and dissolutions. From Figure 5, it is evident that the sample implanted at 40 keV (Figure 5d) exhibits the least amount of corrosion effects mentioned above, and it has also produced the best results for the potentiodynamic test. On the surface of the samples implanted at 10, 20, and 80 keV, pits and peel-offs of the zirconium nitride layer or deeper attacks of the corroding medium into the SS substrates (Figure 5e) can be distinguished in comparison small pits or imperfections have caused an almost uniform distribution of corrosion on the surface of the sample implanted at 20 keV (Figure 5c). These features can be likened to bubbles on the film surface that may also be expected during the corrosion or reaction.

Upon implanting the sample at the highest energy level of 80 keV, the resulting SEM image reveals a significant deterioration in the surface of the zirconium nitride coating such that the corrosive solution can penetrate the steel substrate and ultimately causes the complete removal of the layer.

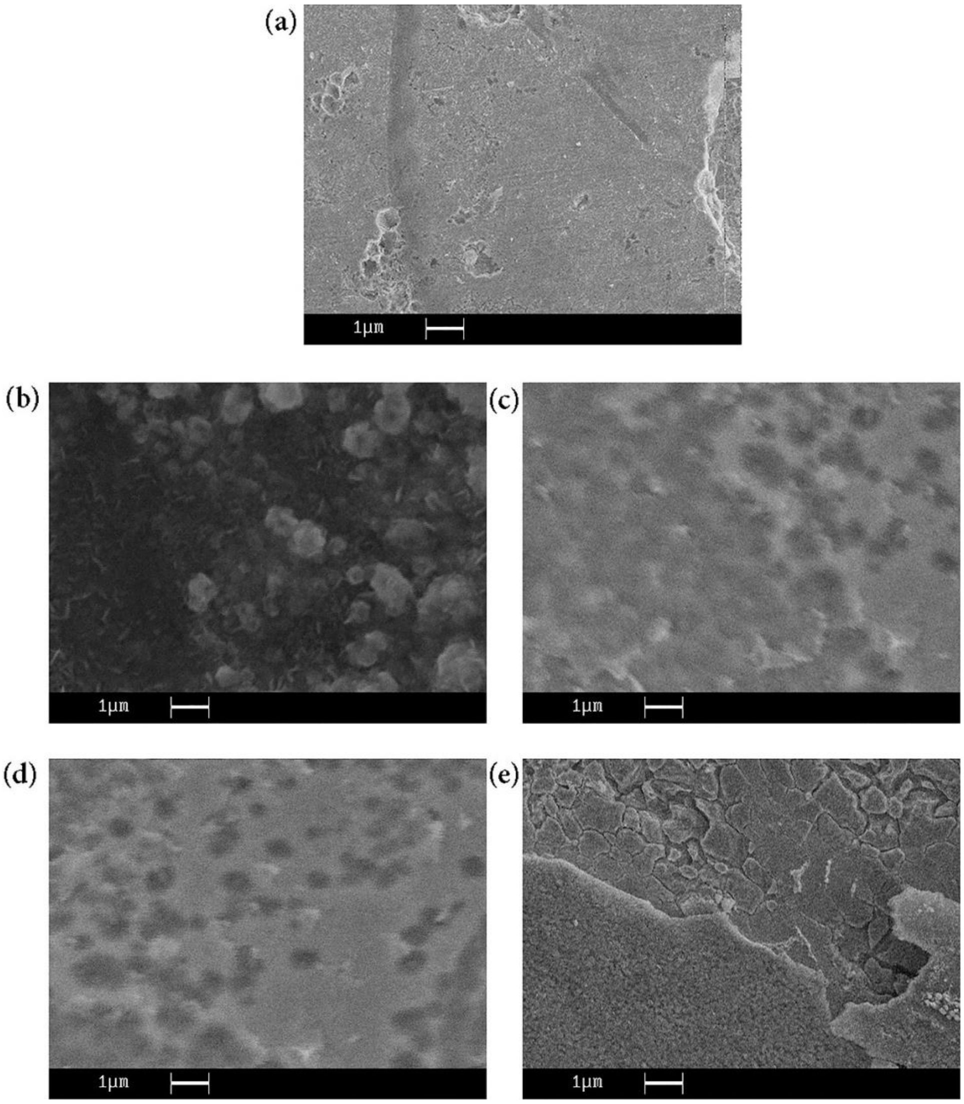

Figure 5: SEM images of different samples produced at different implantation energies: (a) 304 SS, (b) 10 keV, (c) 20 keV, (e) 40 keV and (e) 80 keV.

4. Conclusion

Zirconium nitride thin films were deposited on 304 stainless steel substrates at 400 ^{o}C and then implanted at different energies. The XRD pattern of ZrN/SS samples shows the formation of the ZrN crystal phase with the preferred growth direction (111). The peak intensity corresponding to this direction increases with the implantation energy up to 40 keV. Increasing the implantation energy to 80 keV has decreased (111) peak intensity. With the increase of energy up to the optimal value of 40 keV, the hardness of the samples had an upward trend and then decreased. The maximum measured hardness value is equal to 561 Hv. The sample implanted in the energy of 40 keV with a corrosion current density of 0.0194 μA cm^{-2} and a corrosion potential of 0.02 V has optimal results for corrosion resistance in the test environment. The optimal sample also showed the most intact surface after the corrosion test in SEM images.

5. References

1. M. Ohring, materials science of thin films, Academic press, New York, 1991.
2. L. Eckertova, Physics of Thin Films, Plenum Press, New York, 1990.
3. C.-H Ma, J.-H. Huang, H. Chen, A study of preferred orientation of vanadium nitride and zirconium nitride coatings on silicon prepared by Ion beam assisted depostion, *Surf. Coat.*, 133-134(2000), 289-294.
4. A. R. Grayeli Korpi, Kh. M. Bahmanpour, Effect of nitriding temperature on the nanostructure and corrosion properties of nickel coated 304 stainless steel, *Prog. Color Colorants Coat.*, 10(2017), 85-92.
5. K. I. Aly, A. Mahdy, M. A. Hegazy, N. S. Al-Muaike, S.W. Kuo, M. G. Mohamed, Corrosion resistance of mild steel coated withPhthalimide-functionalized polybenzoxazines, *Coatings*, 10(2020), 1114.
6. M. G. Mohamed, S.W. Kuo, A. Mahdy, I.M. Ghayd, K. I. Aly, Bisbenzylidene cyclopentanone and cyclohexanone-functionalized polybenzoxazine nanocomposites: Synthesis, characterization, and use for corrosion protection on mild steel, *Mater. Today Commun.*, 25(2020), 101418.
7. K. I. Aly, M. G. Mohamed, O. Younis, M. H. Mahross, M. Abdel-Hakim, M. M. Sayed, Salicylaldehyde azine-functionalized polybenzoxazine: Synthesis, characterization, and its nanocomposites as coatings for inhibiting the mildsteel corrosion, *Prog. Org. Coat.*, 138(2020), 105385.
8. M. G. Mohamed, A. Mahdy, R. J. Obaid, M. A. Hegazy, S.W. Kuo, K. I. Aly, Synthesis and characterization of polybenzoxazine/clay hybridnanocomposites for UV light shielding and anti-corrosion coatings on mild steel, *J. Polym. Res.*, 28(2021), 297.
9. J. A. Garcia, A. Guette, A. Medrano, C. Labrugere, M. Rico, M. Lahaye, R. Sanchez, A. Martines, R. J. Rodiguez, Nitrogen Ion implantation on group IVb metals: chemical, mechanical and tribological, *Vaccum*, 64(2002), 343-351.
10. R. J. Rodriguez, J. A. Garcia, A. Medrano, M. Rico, R. Sanchez, R. Martinez, C. Labrugere, M. Lahaye, A. Guette, Tribological behaviour of hard coatings deposited by arc-evaporation PVD, *Vacuum*, 67(2002), 559-566.
11. J.H. Huang, C.Y. Hsu, S.S. Chen, G.P. Yu, Effect of substrate bias on the structure and properties of Ion-plated ZrN on Si and stainless steel substrates, Mater. Chem. Phys., 77(2003), 14-21.
12. W. J. Chou, G. P. Yu, J. H. Huang, Bias effect of Ion-plated Zirconium nitride film on Si (100), *Thin Solid Films*, 405(2002), 162-169.
13. A. R. Grayeli Korpi, Kh. M. Bahmanpour, Influence of nitrogen Ion implantation on the structure and corrosion resistance of stainless steel substrates coated with Ni nanolayer, *Prog. Color Colorants Coat.*, 9(2016), 77-83.
14. D. Pilloud, A. S. Dehlinger, J. F. Pierson, A. Roman, I. Pichon, Reactively sputtered zirconium nitride coating: structural, mechanical, optical and electrical characteristics, *Surf. Coat.*, 174-175 (2003), 338-344.
15. L. Hu, D. Li, G.Fang, Influence of $N_2(N_2$+Ar) flow ratio and substrate temperature on the properties of Zirconium nitride films prepared by reactive DC magnetron sputtering, *Appl. Surf. Sci.*, 220(2003), 367-371.
16. J.G. Han, J.S. Lee, B.H. Choi, W. Kim, G. Tang, Wear and fretting wear behaviour of ion-implanted zircaloy-4, *Surf. Coat.*, 83(1996), 307-312.
17. J.R. Davis, ASM Specialty Handbook: Stainless Steels (Materials OH: ASM International, 1994), 22.

How to cite this article:
M. Karimi, A.R. Grayeli, Analysis of Nitrogen Ion Implantation on Corrosion Inhabitation of Zirconium Nitride Coated 304 Stainless Steel and Correlation with Nano-strucrure and Surface Hardness. Prog. Color Colorants Coat., 16 (2023), 409-415.

Vol.16, No.4(51), Summer 2023

PROGRESS
IN COLOR, COLORANTS AND COATINGS

CONTENTS

Progress in Color, Colorants and Coatings